FATIGUE AND FRACTURE ANALYSIS OF HELICOPTER FUSELAGE STRUCTURES

A THESIS SUBMITTED TO
THE GRADUATE SCHOOL OF NATURAL AND APPLIED SCIENCES
OF
MIDDLE EAST TECHNICAL UNIVERSITY

BY

RIZA ÖZCAN

IN PARTIAL FULFILLMENT OF THE REQUIREMENTS
FOR
THE DEGREE OF MASTER OF SCIENCE
IN
MECHANICAL ENGINEERING

JANUARY 2013

Approval of the thesis:

FATIGUE AND FRACTURE ANALYSIS OF HELICOPTER FUSELAGE STRUCTURES

submitted by **RIZA ÖZCAN** in partial fulfillment of the requirements for the degree of **Master of Science in Department of Mechanical Engineering, Middle East Technical University** by,

Prof. Dr. Canan Özgen _____
Dean, Graduate School of **Natural and Applied Sciences**

Prof. Dr. Süha Oral _____
Head of Department, **Mechanical Engineering**

Assoc. Prof. Dr. Serkan Dağ _____
Supervisor, **Mechanical Engineering Dept., METU**

Examining Committee Members:

Prof. Dr. Suat Kadıoğlu _____
Mechanical Engineering Dept., METU

Assoc. Prof. Dr. Serkan Dağ _____
Mechanical Engineering Dept., METU

Asst.Prof.Dr. Gökhan Özgen _____
Mechanical Engineering Dept., METU

Asst. Prof. Dr. Ender Ciğeroğlu _____
Mechanical Engineering Dept., METU

Dr. Tunç Apatay _____
Mechanical Engineering Dept., Gazi University

Date: 29.01.2013

I hereby declare that all information in this document has been obtained and presented in accordance with academic rules and ethical conduct. I also declare that, as required by these rules and conduct, I have fully cited and referenced all material and results that are not original to this work.

Name, Last name: Rıza ÖZCAN

Signature:

ABSTRACT

FATIGUE AND FRACTURE ANALYSIS OF HELICOPTER FUSELAGE STRUCTURES

Özcan, Rıza

M.Sc, Department of Mechanical Engineering

Supervisor: Assoc. Prof. Dr. Serkan Dağ

January 2013 , 101 pages

In this study a methodology is developed for the fatigue and fracture analysis of helicopter fuselage structures, which are considered as the stiffened panels. The damage tolerance behavior of the stiffened panels multiaxially loaded is investigated by implementing virtual crack closure technique (VCCT). Validation of VCCT is done through comparison between numerical analysis and the studies from literature, which consists of stiffened panels uniaxially loaded and the panel with an inclined crack. A program based on Fortran programming language is developed to automate the crack growth analysis under mixed mode conditions. The program integrates the prediction of the change in crack propagation direction by maximum circumferential stress criterion and the computation of energy release rate by VCCT. It allows reducing the computation time for damage tolerance evaluation for mixed mode cases through finite element analysis and runs the procedure file of MSC.Marc/Mentat for numerical analysis and the program generated by Patran Command Language (PCL) of MSC.Patran for remeshing. The developed code is verified by comparing the crack growth trajectories obtained by numerical analysis with the experimental studies from literature. A submodeling technique is utilized to analyze a particular fuselage portion of helicopter tail boom. Effects of different skin/stringer configurations of the helicopter fuselage structure on stress intensity factor are studied by means of the developed program. Fatigue crack growth analysis is performed by using stress intensity factors obtained from numerical analysis and fatigue propagation models proposed in literature.

Keywords: crack propagation, VCCT, fatigue life, stiffened panel

ÖZ

HELİKOPTER GÖVDE YAPILARININ YORULMA VE KIRILMA MEKANİĞİ ANALİZİ

Özcan, Rıza

Yüksek Lisans, Makina Mühendisliği Bölümü

Tez Yöneticisi: Doç. Dr. Serkan Dağ

Ocak 2013, 101 sayfa

Bu çalışmada güçlendirilmiş panel olarak davranılan helikopter gövde yapılarının yorulma ve kırlıma mekaniği analizleri için bir metot geliştirilmiştir. Çok yönlü yüklenmiş güçlendirilmiş panellerin hasara tolerans davranışı sanal çatlak kapama tekniği (VCCT) kullanılarak incelenmiştir. VCCT' nin doğrulanması için sayısal analiz sonuçları literatürdeki tek yönlü yük altındaki güçlendirilmiş panel ve açılı çatlak içeren plaka çalışmaları ile karşılaştırılmıştır. Fortan programlama dili ile karışık mod durumunda çatlak ilerleme analizini otomatikleştirmek için bir program geliştirilmiştir. Program en yüksek çevresel gerilme kriteri kullanarak çatlak yön değişimini ve VCCT kullanarak enerji serbest kalma oranını hesaplamaktadır. Program yardımı ile yapıların sonlu elemenlar yöntemi ile hasara tolerans analizi değerlendirmesi için gerekli hesaplama zamanı azalacaktır. Analizler için MSC.Marc/Mentat prosedür dosyaları ve sonlu elemanlar modelinin güncellenmesi için MSC.Patran' ın programlama dilinde (PCL) oluşturulmuş program çalıştırılır. Geliştirilen kodun doğrulanması için sayısal analizler ile elde edilen çatlak güzergâhı literatürden deneysel çalışmalar ile karşılaştırılmıştır. Helikopter kuyruk kısmındaki bir gövde yapısının analizi için alt-modelleme tekniği kullanılmıştır. Helikopter gövde yapısının farklı kabuk/kiriş yapılandırmalarının gerilim şiddet katsayısı üzerindeki etkileri geliştirilen program yardımı ile çalışılmıştır. Sayısal analizler ile elde edilen gerilim şiddet değerleri ve literatürdeki yorulma ilerleme modelleri kullanılarak yorulma kaynaklı çatlak ilerleme analizleri gerçekleştirilmiştir.

Anahtar kelimeler: çatlak ilerlemesi, VCCT, yorulma ömrü, güçlendirilmiş panel

To My Family

ACKNOWLEDGEMENTS

First of all, I would like to thank this supervisor, Prof. Dr. C. Serkan Dağ for his guidance and advices throughout the study.

I am heartily thankful to my company TUSAŞ for supporting my thesis. I would like to express special thanks to my colleagues in TUSAŞ for their supports and help.

I would like to express my deepest gratitude to my family for their continuous motivation and encouragement.

TABLE OF CONTENT

LIST OF TABLES

TABLES

LIST OF FIGURES

FIGURES

LIST OF SYMBOLS

E	Modulus of Elasticity
a	Crack Length
t	Thickness of the Plate
v	Poisson's Ratio
K_c	Critical Stress Intensity Factor, Fracture Toughness
θ	Angle from the Crack Plane
r	Distance from the Crack Tip
K	Stress Intensity Factor
K_I	Mode I Stress Intensity Factor
K_{II}	Mode II Stress Intensity Factor
K_{III}	Mode III Stress Intensity Factor
G	Energy Release Rate
μ	Poisson's Ratio
σ	Axial Load
β	Geometric Factor
F_y	Normal Force
F_x	Shear Force
A	Cross Section Area
L	Length
K_{th}	Threshold Stress Intensity Factor
K_{eff}	Effective Stress Intensity Factor
R	Stress Ratio
S	Strain Energy Density Factor

CHAPTER 1

INTRODUCTION

1.1. Motivation

Fracture mechanics is a significant phenomenon to be understood by structural analysis engineers working for aerospace industry. The disciplines of fracture mechanics give the answer of the question whether the structure containing defects to be replaced or to leave it in service for a certain period of time. It means cracks should be kept under control.

There are aerospace accidents caused by fracture in history showed that damage tolerance design of the critical structures was crucial. Two catastrophic ones of those accidents are Boeing 737 and the de Havillan Comet [1]. The roof of a Boeing 737 was tore away due to a large crack formed by multiple fatigue cracks in 1988 (Figure 1). The accident of the Comet was caused by a crack developed in the front of the cabin roof turned into a very large crack in 1954. In those accidents many people were killed and injured. It stimulated a reassessment of the methods to ensure the structural integrity. It gets very clear that aircraft structures shall be designed to sustain damage by avoiding catastrophic failure during its life or inspection interval.

In order to evaluate the damage tolerant behavior of the fuselage structures subjected to cycling fatigue loads, fracture mechanics methods should be considered. Fracture mechanics approach is mainly dealing with the mechanical behavior of an existing crack on a structure. Its scope covers the subjects as whether the certain size of crack is tolerable by the structure or not, the crack growth rate, direction of the crack extension and the life of the component up to failure. In other words, the behavior of cracks at propagation and final failure phase is investigated by fracture mechanics. The source of cracks is mainly fatigue, fretting, corrosion, manufacturing defects and damages from accidents etc. The main concept is based on detection of those cracks before reaching its critical length.

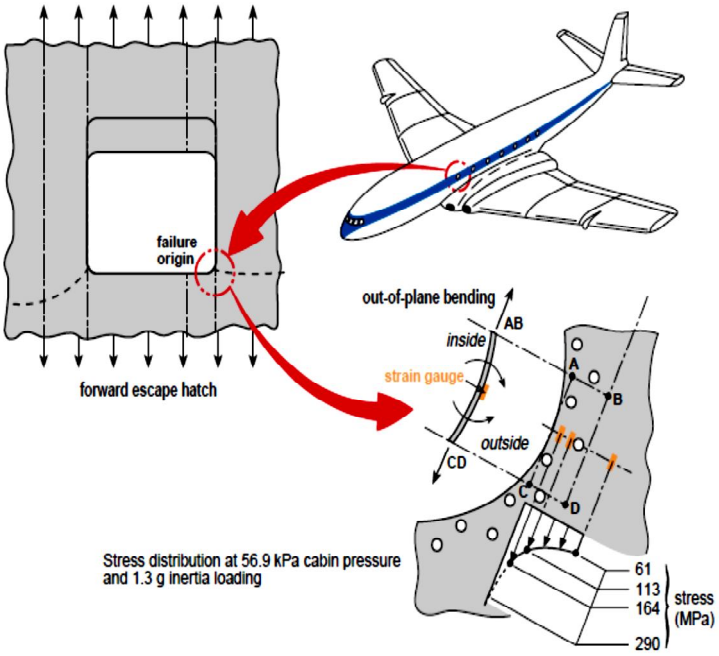

Figure 1 Probable failure origin of Comet (1988)[1]

Understanding and investigation of the parameters having influence on slowing or arresting the crack before critical length are very crucial. For example, the stiffeners attached to a panel improve the damage tolerance performance of the panel. When the skin has a crack the stiffeners represent an alternative load path to the skin. As a crack grows in the panel closing to a stiffener, a portion of the load contributing the stress intensity factor at the crack tip can move out of the sheet into the stiffeners. Therefore the crack tip stress intensity factor decreases in parallel with reducing the amount of the load in the panel.

Stress intensity factor is an important parameter of the fracture mechanics. It is essential to accomplish the fatigue crack growth analysis. The published values and analytical solutions of stress intensity factor are not available in the literature for complex crack configurations, especially mixed-mode cases. The outcome of this thesis is to investigate fatigue life of a fuselage structure subjected to complex loading such as helicopter fuselage by utilizing stress intensity factor values predicted by FEM (finite element method). The analyses of fracture mechanics can be successfully performed by the finite element approaches. A crack propagation program is developed to make an automatic crack extension to generate the stress intensity factor against crack length for especially mixed mode cases. It helps to investigate the effects of the structural parameters on the stress intensity factor by considerably reducing the analysis time.

1.2. Literature Review

The fuselage structure of a helicopter or an airplane is composed of skin panels and stiffeners, longitudinal and circumferential ones of which is called as stringers and frames respectively (Figure 2). Hence it is considered as stiffened panels. The assembling methods of the stringers and frames to the panels are generally riveted and welded, but intact stiffener panel configurations, where the stiffeners are integrally machined with the panel is also

present. The manufacturing methods of integrally stiffened panels can be listed as extrusion of wide panels with integral stiffeners, joining by welding technologies such as friction stir welding (FSW) and laser welding, high speed machining of the panel with stiffeners. The most common method is to assemble the stringers or frames to the skin by riveting process in aerospace industry.

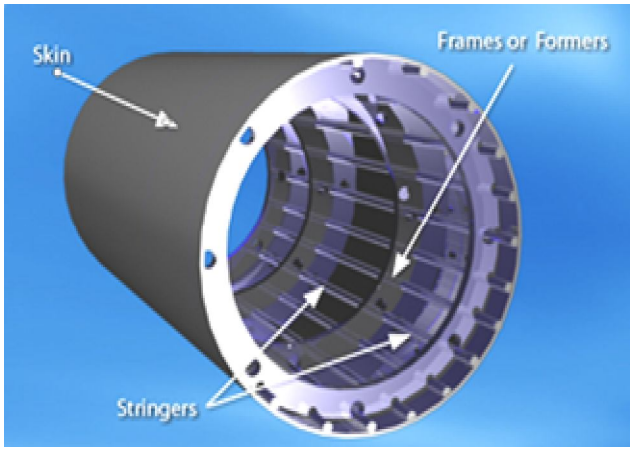

Figure 2 Components of a fuselage structure

The preliminary sizing of the airframe structures (the skin-stringer combination) is done by considering the ease of manufacturing and assembly, material properties, basic loads and the judgements based on previous experience etc. The weight is also an important parameter for the sizing. The structural analyses for the sizing of the skin-stringer combination include the stability (crippling, inter-rivet buckling, buckling etc.), yielding stress, fatigue and damage tolerance.

Fatigue and fracture analysis of the fuselage structures are one of the subjects, which researchers are mostly interested in aerospace design. The experiments and finite element methods are widely used to comprehend the damage tolerance behavior of the stiffened panels.

This study covers two major subjects; one of them is stress intensity factor computation by different techniques using FEM and the assessment of damage tolerance behavior of the stiffened panels by FEM, the other one is automatic crack propagation with direction change and fatigue life assessment for mixed mode case. Hence the studies in the literature are classified into two sections accordingly.

1.2.1. Assessment of damage tolerance behavior of the stiffened panels by FEM

There are many studies on the fracture mechanics analyses by means of useful techniques such as VCCT (virtual crack closure technique), J-integral, DCT (displacement correlation technique) and cohesive zone method etc. Finite element methods by commercial software packages are extensively employed for linear elastic fracture mechanics problems. The researchers especially utilize those methods for the stress intensity factor and the energy release rate calculations. They can be used to simulate fatigue crack growth and to understand the damage tolerance behavior of the structure.

In this study VCCT is used to compute energy release rates (G_I and G_{II}). VCCT can be utilized for 2D and 3D crack problems. In some of the studies the result of the analyses by finite element methods were compared favorably by the other methods and the good achievements were obtained [2], [3], [4].

Tavers et al. [2] examined several finite element techniques such as J-integral, DCT (displacement correlation technique), VCCT and compounding method. The solutions of stress intensity factor by FEM are compared with the analytical solutions for the cases of plate with collinear cracks and stiffened panel with crack. It is concluded that VCCT can yield sufficiently accurate results for even complex structure.

Analytical solutions of stress intensity factors for complex geometry and loading is not readily available in literature. The analytical solutions for the stiffened panels are mainly on the sheet and stringer configuration with uniform size of stiffeners, equally spaced rivets and uniaxial loading [5], [6]. In the study of Poe [5], stress intensity factors were computed for the sheet containing a crack that is located symmetrically with respect to the stringers; that is, a crack that extends equally on both sides of a point midway between two stringers. He used the principle of superposition to calculate the total stress intensity factor. Hence the expression of stress intensity factor becomes as below:

$$K = S\sqrt{\pi a} + \sum_j K_j Q_j \tag{1}$$

where S is uniaxial stress, a is the half crack size, $K_j Q_j$ is the component due to symmetric set of rivet forces Q_j (see Figure 3).

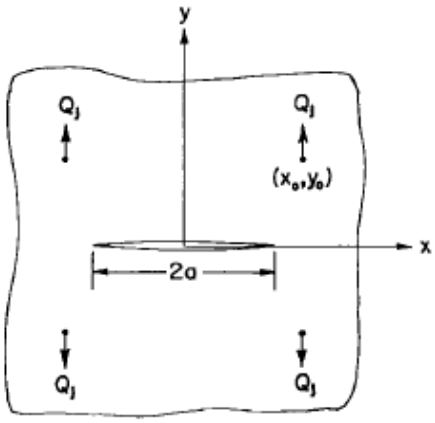

Figure 3 Combination of central crack and point forces from rivets [5]

The studies using finite element methods on the stiffened panels are mainly focused on the cases, in which uniaxial loading is applied and Mod-I stress intensity factor is computed.

In the paper by Carta and Pirondi [7] damage tolerance behavior of the panels integrally stiffened by the stringers was investigated by different modeling techniques such as solid

and shell mesh, inclusion of adhesive into model etc. The stress intensity factor computed by finite element method was used to determine crack growth rate. The comparison with the experiment results was presented with good agreement.

In the study by Adeel [8], the comparison of the damage tolerance was performed between integrally and riveted stiffened panels made of aluminum alloy by computing stress intensity factors. Both stringer and panels were modeled by SHELL 181 –element of finite element analyses software, Ansys. The failure of the panel was also analyzed by calculating Von-mises stress for the holes. The results showed that as the crack propagated through the stringers, as opposed to riveted stiffened panels, the stress intensity factor values went up in the integrally stiffened panels. He also investigated the rise of the Von-mises stresses around the rivet hole of the stringer as the crack passes through the stringer. The increase did not cause the failure of the stringer.

Another study by Tavers et al. [9], presented the stress intensity factor computation by modified virtual crack closure technique supported by Abaqus software for integrally stiffened panels. NASGRO law has been used to predict fatigue life with the inclusion of residual stress due to manufacturing processes. The effect of residual stress on the fatigue life was investigated by finite element method and the experimental studies.

The paper presented by Brot et al. [10] was about the damage tolerance behavior of the integrally stiffened panels. The finite element analysis was performed by Abaqus software. J-integral method is used to compute stress intensity factor. Crack growth analysis was carried out by NASGRO law. The analysis and experimental results has indicated that damage tolerance of integrally stiffened panels were not good.

Arsene et al. [11] developed a software tool to optimize damage tolerance of airframe stiffened panels. The various parameters related to bonded, integrally stiffened and riveted panels can be selected in the tool. The finite element modeling and analysis are performed by employing commercial software MSC.Marc/Mentat integrated into this tool. Crack opening displacement and strain energy release rate methods are implemented to compute stress intensity factor in the tool. The output of the tool is crack length versus stress intensity factor curves. The results obtained by the tool were compared with experimental studies and very good agreement was observed.

1.2.2. Crack propagation analysis under mixed mode loading

The crack propagation analysis mainly includes two consecutive steps; at the first step finite element model is prepared with proper mesh for the crack tip and the crack path, and the succeeding step is to compute stress intensity factors and the direction of crack extension for the new condition. The steps are repeated up to prescribed crack length. Automatic crack propagation requires automatic remeshing work and programming effort.

One of the studies on the automatic crack propagations the study conducted by Bochard and Chastel [12]. They compared the maximum strain energy release rate, minimum strain energy density criterion and the maximum circumferential stress criterion for various experimental applications to determine the crack propagation direction. They also proposed an alternative approach to maximum circumferential stress criterion by employing integration points nearest to the crack tip. The comparative study suggests that the accuracy of the maximum circumferential stress criterion and the maximum strain energy release rate criterion is better than the minimum strain energy density criterion. One of the applications used in comparative study is illustrated in Figure 4.

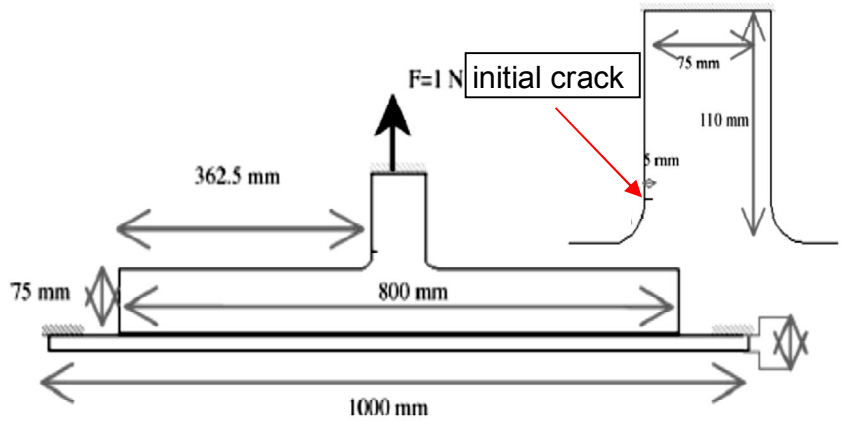

Figure 4 An experimental setup to generate mixed mode at the crack tip

Another study on the simulation of crack growth and computation of stress intensity factors in three-dimensional model is presented by Ayhan [13]. He used enriched crack tip finite elements in his crack growth model with the good agreement by literature.

Colombo and Giglio [14] developed a remeshing algorithm for the crack propagation simulation on the finite element models with shell elements. The code is adaptable to any FE solver capable of sub-modeling and can be used with any existing finite element model at the beginning of analyses. They applied the code on the fuselage of a helicopter and obtained good agreement on the crack growth path with the experimental results.

In the study of Miranda et al. [15] two software codes were developed to estimate the fracture life for two dimensional finite element models. The first part of the code has the capability of the remeshing and computation of the stress intensity factors and the crack growth direction. The computation of stress intensity factor is performed by the method of the displacement correlation technique (DCT) with quarter-point singular elements in the vicinity of the crack tip. The remeshing phase of the algorithm includes smooth passing procedure from coarse elements size to fine element and eliminating the bad-shaped elements.

Another numerical investigation supported by experimental study is conducted by Maksimovic and Boljanovic [16]. The stress intensity factor calculations in the case of mixed-mode were done by employing quarter point singular elements. The maximum circumferential stress criterion was used to predict the crack extension angle step by step. Very good correlation is obtained between experiments and numerical studies. The specimen types used in experimental study are illustrated in Figure 5. One of the case studies (see Figure 5.b) performed by Maksimovic and Boljanovic is also used to validate the developed method in this thesis.

Qian and Fatemi [17] investigated the crack growth rate of a four point bending specimen under the mixed mode fatigue loading. Crack growth trajectories, which were obtained by experiments and finite element analysis, were compared and good correlation was obtained for both the minimum strain energy density criterion and maximum circumferential stress criterion. They concluded that the good estimation of crack growth rate is obtained if the effective stress intensity factors are computed from the curved cracks.

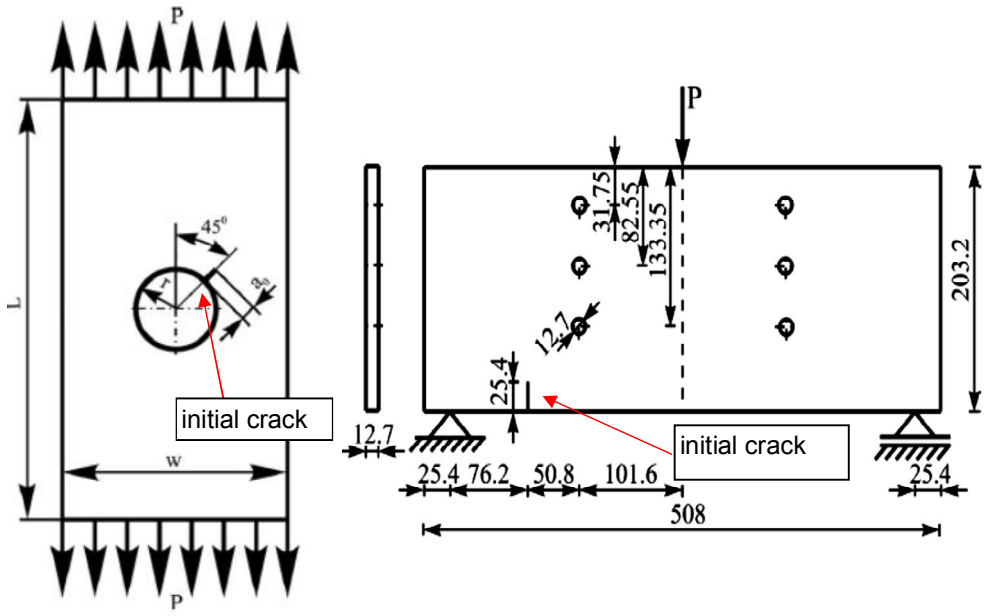

(a) (b)

Figure 5 (a) The plate with crack emanating from the edge of a hole, (b) Three Point Bending Beam with initial crack of 25.4 mm

Regarding fatigue crack growth of a fuselage panel under mixed mode case, a study by Cehn et al. [18] was performed by using FRANC3D/STAGS software system. With enhancement of the software's, several parameters affecting crack trajectories were studied. It was found that the initial crack angle and the length of the crack growth increment had no considerable effect on the prediction of the crack trajectory, whereas rivets and debonding properties had significant effect. Another result of the study is that the residual strength is significantly affected by crack trajectories.

1.3. Organization of Thesis

The main purpose of the study is to develop a method for life assessment of the helicopter fuselage structures by utilizing fracture mechanics approach. As regards this purpose, the damage tolerance behavior of the stiffened panel with crack is investigated for mixed mode condition and a code is developed to estimate the stress intensity factors against the crack length. First of all validation of the methods used through the study is done. Then they are used for fatigue and fracture analyses of the particular helicopter fuselage structure.

The first part of the thesis includes the finite element analyses performed for the flat stiffened panels and the flat plate with inclined crack by employing VCCT. The stress intensity factors of opening mode, mode-I are estimated for the different configurations of intact and riveted stiffened panels. Then results are compared with the ones from literature. The other comparative study on the flat panel with inclined crack is performed. The panel is subjected to uniaxial tensile loading. Due to inclined crack both the stress intensity factors of mode-I (opening mode) and mode-II (sliding mode) exist. The accuracy of VCCT to estimate the energy release rates for mode-I and mode-II are verified by comparing with analytical solutions.

The second part of the study is concerned with the code developed to carry out automatic crack propagation by VCCT analysis in conjunction with the prediction of the crack extension direction by maximum circumferential stress criterion. The Fortran code is prepared to handle stress intensity factor calculation against the crack length. The code runs the algorithms prepared by the programming language (Patran Command Language (PCL)) of MSC.Patran and MSC.Marc/Mentat procedure files. Crack growth trajectories predicted by the developed program are compared with two different case studies from literature.

The last part covers the application of the developed code to a sub-structure of a helicopter fuselage. The effects of the several parameters such as rivet flexibility, rivet pitch, the size of the stiffener and the thickness of the panel on stress intensity factor are investigated by means of the developed code performing the automatic crack propagation. The review of crack propagation models for mode-I and mixed mode are also presented in this section. The way to estimate crack length against the number of cycles from the stress intensity factor values with crack length obtained by numerical analysis is explained, and it is used for the helicopter fuselage.

CHAPTER 2

DETERMINATION OF THE STRESS INTENSITY FACTOR BY FINITE ELEMENT METHOD

2.1. Introduction

Three basic modes of the crack growth exist in general, although mixed-mode growth is also possible (Figure 6). Mode-I is the opening mode where crack faces separate symmetrically. In Mode-II, the crack surfaces slide relative to each other perpendicular to the leading edge of the crack, and shear stresses in the y direction occur ahead of the crack. In Mode-III, the sliding of the crack surfaces occurs with respect to one another in the z direction and it leads to shear stresses in the z direction.

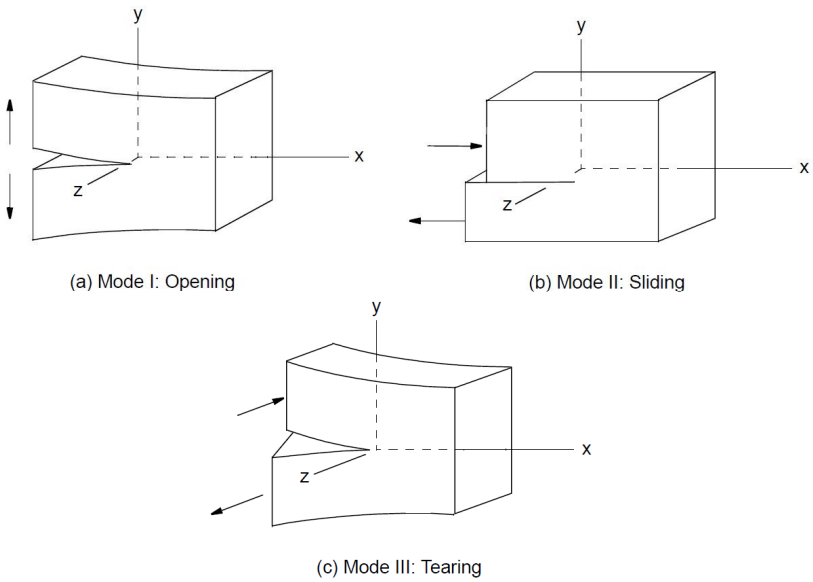

Figure 6 Fracture modes; a) opening mode, b) shearing mode, c) tearing mode [37]

The problems with Mode-I is the most common in engineering applications. Mode-II and mode-III are not widely experienced. It is probable to see two modes of crack propagation simultaneously in complex loadings.

The stress intensity factor is a measure of the magnitude of the stress occurring in the highly stressed region at the crack tip in an elastic solid [15]. It is a function of the loading on the body with crack, geometrical features and the crack size. By the elasticity theory, it is possible to calculate the stress field at the crack tip in a body with crack under a loading. The crack tip stresses in the local coordinate system shown in Figure 7 are;

$$\sigma_{ij} = \frac{K_I}{\sqrt{\pi 2r}} f_{ij}(\theta) + C_1 r^0 + C_2 r^{1/2} \ldots \quad (2)$$

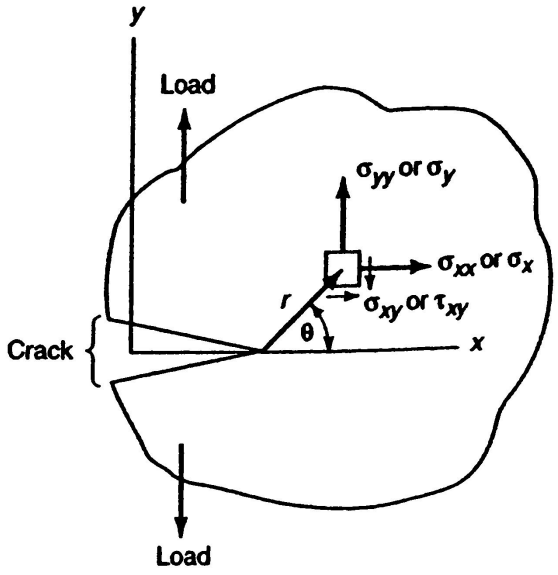

Figure 7 Stress components at the crack tip

For the stress in y-direction for the plane θ=0, the function of $f_{yy}(\theta)$ =0, it results in;

$$\sigma_{yy} = \frac{K_I}{\sqrt{2\pi r}} \quad (3)$$

It means that stress intensity factor, K, can be defined as a function of a distance "r" near crack tip and the applied load (stress).

The geometric factor (β) has been calculated and compiled in for many generic geometries in various handbooks [5], [19], [20].

The general expression of the stress intensity factor is defined as:

$$K = \beta\sigma\sqrt{\pi.a} \tag{4}$$

All geometrical effects are represented by the geometric parameter, β.

When the loading is cyclic, the stress intensity factor range is defined in terms of the range of the alternating stress, $\triangle\sigma$;

$$\Delta K = \beta\Delta\sigma\sqrt{\pi.a} \tag{5}$$

2.2. Finite Element Methods to Compute SIF

For materials that exhibit mostly elastic deformation prior to failure, linear elastic fracture mechanics (LEFM) provides a good prediction of the crack growth. LEFM is a relatively simple and direct method for finding fracture toughness that is based on crack tip stress intensity parameter, K. The finite element methods are widely employed to predict stress intensity factor. The mostly used methods can be listed as:

- Displacement Correlation Technique [21]
- Modified Crack Closure Integral (MCCI) or Virtual Crack Closure Technique (VCCT)
- J-integral

Last two methods are widely used by researchers. They are available in commercial software like ABAQUS, MSC.Marc/Mentat [38], [37]. There are various studies on comparing the results of both methods. Both of techniques generally give good result even for relatively coarse meshes [15], [2], [23].

Ingraffea and Wawrzynek [23] stated that in general for the same mesh, VCCT yields SIFs that are more accurate than the displacement correlation technique, but less accurate than the J-integral approach.

2.2.1. J-Integral

J-integral concept is defined by Rice [24] as:

$$J = \int_{\mathbf{\Gamma}} \left(wn_1 - \sigma_{ij} \frac{\partial u_i}{\partial x_1} n_j \right) d\mathbf{\Gamma} \tag{6}$$

Where σ_{ij} is the stress tensor, w is the strain energy density, u_i is the displacement vector, Γ is the integration path and n_j is the unit normal to the integration contour.

The J-integral equals to the energy release rate, i.e., $J=G$, when the contour Γ is a circle around the crack tip The equations of J-integral in terms of stress intensity factor, K are given as below:

$$J_{I,II} = G_{I,II} = \frac{K_{I,II}^2}{E'} \tag{7}$$

$$J_{III} = G_{III} = (1+v)\frac{K_{III}^2}{E} \tag{8}$$

Note that $E'=E/(1- v^2)$ for plane strain and $E'=E$ for plane stress, and $\mu=E/2(1+v)$ is the shear modulus.

It is path independent, which is any path Γ that starts and ends on the crack faces will give the same value of J. The value of J is independent of the direction of the crack growth. J is equal to G only for straight ahead crack growth in elastic materials.

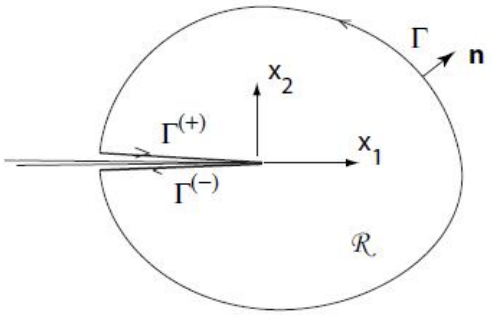

Figure 8 Calculation by J integral taking R to be any fixed region surrounding the crack tip

2.2.2. Virtual Crack Closure Technique (VCCT)

VCCT is a technique to estimate the energy release rate, based on Irwin's crack closure integral. It is used successfully and very widely for fracture analysis. The assumption of crack closure integral is that the energy release when the crack grows is equal to the energy required to close the crack to initial state before crack extends. The technique uses two steps of the analysis.

The VCCT approach was firstly introduced with quadrilateral elements by Rybicki and Kanninen [25]. It is also implemented in conjunction with the quarter point singular elements [26]. VCCT was extended to three-dimensional cracked bodies by Shivakumar [28] and to higher order elements by Raju [27].

In this technique the computation of strain energy release rates is carried out by using the nodal forces at the crack tip and relative displacements in its behind. The crack closure method uses two step finite element analyses in which the crack is extended and closed. The assumption is based on that the released energy at extension of the crack is equivalent to the energy that is required to bring the crack its original state. Modified crack closure

method called as VCCT uses the same assumption with crack closure method. Additionally, another assumption of VCCT is that the extension of crack does not change the state at the crack tip. It allows calculating the energy required to close the crack at one single finite element analysis. In conclusion the energy required to close the crack is calculated for four-node elements as:

$$\Delta E = \frac{1}{2}\left[F_{y3}(u_1 - u_2) + F_{x3}(v_1 - v_2)\right] \tag{9}$$

Where F_{x3} and F_{y3} are the shear and normal forces at tip node-3. u_1, u_2, v_1 and v_2 are the shear and the opening displacements at the nodes behind the crack tip (see Figure 9).

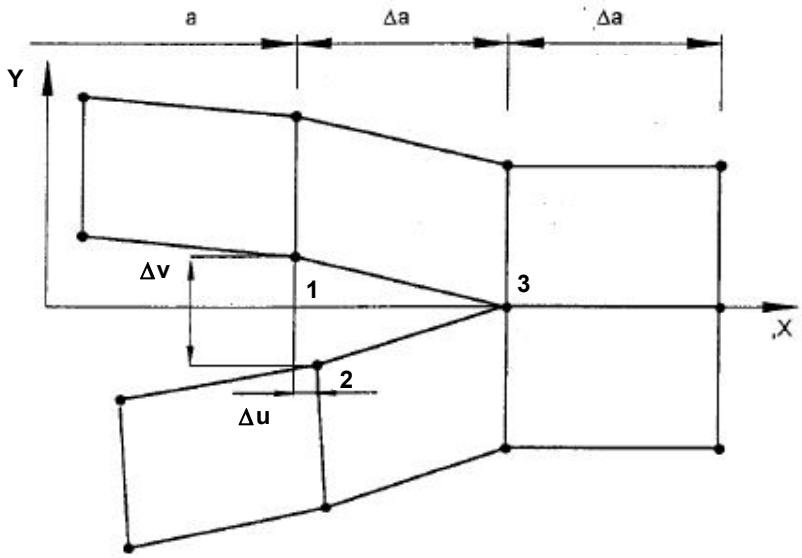

Figure 9 Virtual Crack Closure Technique for 4-node element

The energy release rate, G can be expressed as $\Delta E / \Delta A$, where ΔA is the area of the crack surface. The expression is defined for Mode I and Mode II as follows:

$$G_I = -\frac{F_{y3}(v_1 - v_2)}{2\Delta a t} \tag{10}$$

$$G_{II} = -\frac{F_{x3}(u_1 - u_2)}{2\Delta a t} \tag{11}$$

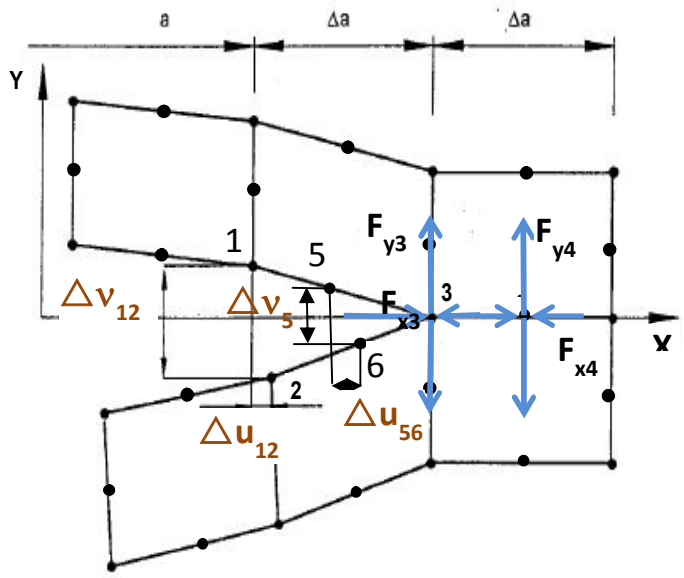

Figure 10 Virtual Crack Closure Technique for 8-node element

For higher order elements, the contributions from mid-side nodes are also included (see Figure 10). The energy release rates, G_I and G_{II} are calculated for eight-nodded elements as below:

$$G_I = -\frac{F_{y3}(v_1 - v_2) + F_{y4}(v_5 - v_6)}{2\Delta at} \tag{12}$$

$$G_{II} = -\frac{F_{x3}(u_1 - u_2) + F_{x4}(u_5 - u_6)}{2\Delta at} \tag{13}$$

According to virtual crack closure relations given by Irwin [29], energy release rates for three modes (G_I,G_{II},G_{III}) are computed by the following expressions in terms of SIFs (K_I, K_{II},K_{III})

$$G_{I,II} = \frac{K_{I,II}^2}{E'} \tag{14}$$

with

$$E' = \begin{cases} E & for\ plane\ stress \\ \dfrac{E}{1-v^2} & for\ plane\ strain \end{cases}$$

$$G_{III} = (1 + v)\frac{K_{III}^2}{E} \tag{15}$$

There are some studies comparing VCCT with other methods, and the studies showed that VCCT is a reliable method. [2], [30] According to the study by Bucholz, Chergui and Richard, the accuracy was verified for the center cracked tension specimen [30].

The virtual crack closure technique is very attractive method for the computation of energy release rates with good accuracy. The analysis with VCCT does not make assumption for the stresses and displacements in the vicinity of the crack tip. Hence the other benefits of the VCCT are easily implemented and no need special crack tip elements at crack tip. The major drawback of the VCCT is that its application is only limited for linear elastic fracture mechanics (LEFM).

2.3. Comparison of stress intensity factors from numerical analysis with literature

In this part of the study stress intensity factors for the cracked stiffened panels subjected to uniform uniaxial loading are computed by numerical analysis. The results from the analytical solutions for stiffened panels from literature are compared with those obtained by the finite element method. The finite element analyses are performed by commercial software MSC.Marc/Mentat, and MSC.Patran is used as pre-processor for modeling the stiffened panel with the crack.

The study covers two case studies; the intact stiffened panel and the riveted stiffened panel. Uniaxial loadσ is uniformly applied in the perpendicular direction to the crack. One edge of the panel parallel to the stiffener is fixed in y direction. The edge perpendicular to the stiffener is fixed in two degree of freedom, x and y directions. The out-of plane deformations of the entire panel and the stiffener are restricted by fixing in z direction.

The stress intensity factors, K_I are normalized to the stress intensity factor in the absence of the stiffener, K_0. Variation of the normalized stress intensity factor are investigated for the different stiffness ratio (λ), for the different ratios of the crack length to rivet pitch (a/h) and for the different ratios of the crack length to the distance between the crack center and the stiffener (a/b). The value of b is the distance from the crack center to the stiffener. The value of h is the distance between the rivets equally spaced. λ is a measure of the stiffness ratio between the sheet and the stiffener. The expression of λ is given as below:

$$\lambda = \frac{2E_1 at}{E_2 A} \tag{16}$$

where a is half of the crack length, $E_1$is young's modulus of the sheet, and t is the thickness of the sheet respectively. E_2 and A are young's modulus and the cross section area of the stiffener respectively.

The finite element model used for the different stiffened panel configurations is shown in Figure 11. In this study stiffeners are modeled by 1D bar elements with different cross sections. The flat panel is modeled by using 2D quadrilateral elements. Rivets are modeled by 1D bar elements. The rivets are considered as rigid so that very high stiffness values are used for the stiffeners.

The parameters used in the analyses are given in Table 1.

Table 1 The parameters in FEA

Poisson's ratio, μ (plate and stiffener)	0.33
Modulus of elasticity, E (plate and stiffener)	70000 Mpa
Distributed Load-σ	100 Mpa
Thickness of the plate	2 mm
The element size along the crack	1 mm
Global mesh size	4 mm
Element Type	QUAD4-Bar2

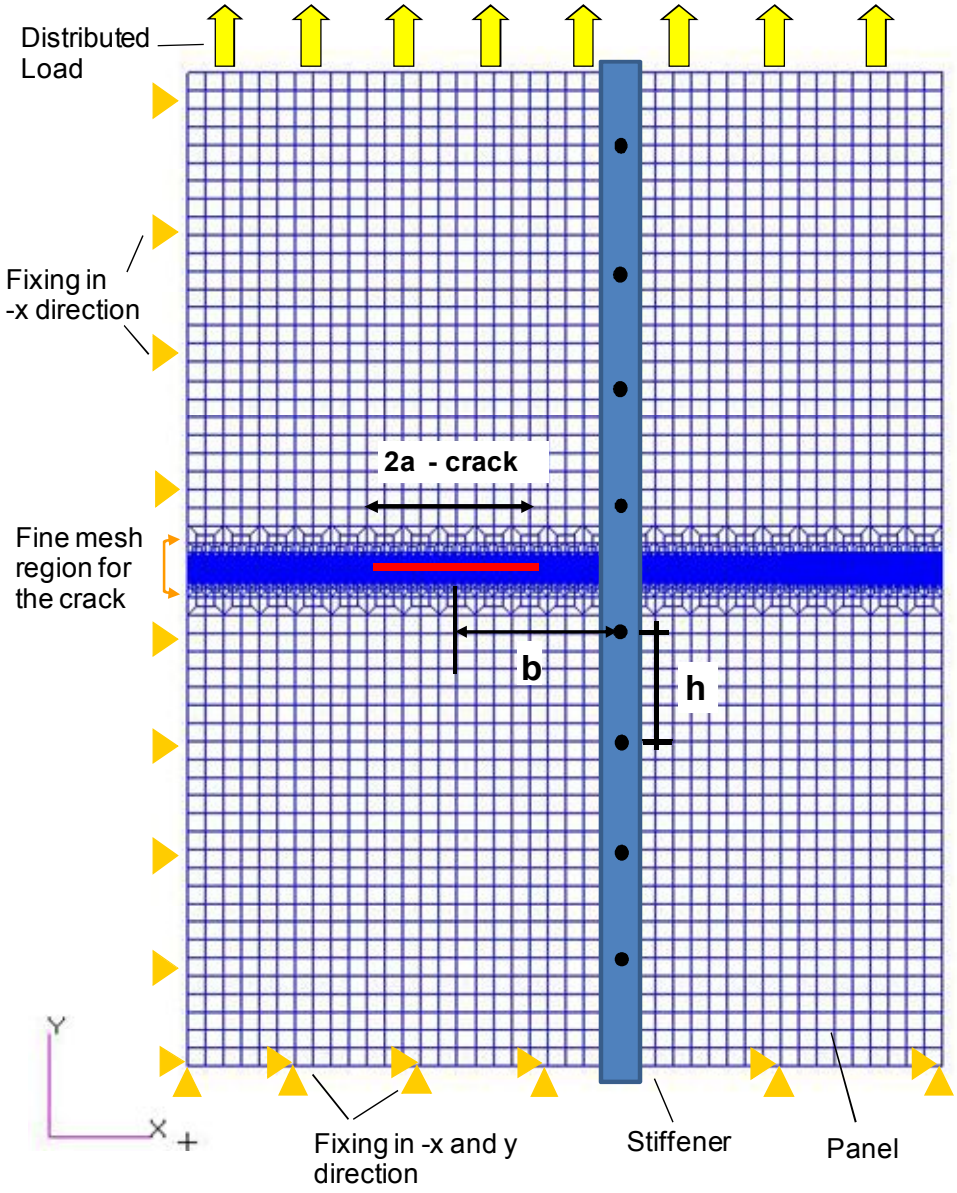

Figure 11 Boundary conditions in FEA for the stiffened panel

2.3.1. Crack near an intact stiffener on a sheet

First case study is on the intact stiffener on a sheet. The stress intensity factors computed by FEM are compared with the values calculated at the study of Greif and Sanders [19], in which the crack tip grows closer to one stiffener. Opening mode stress intensity factors are determined for intact stiffener configuration in their study. Bending stiffness of the stiffener is ignored.

When a/b increases, which means the crack tip moves closer to stiffener, the stress intensity factor diminishes as expected. However increase of λ raises up the stress intensity factor because the stiffness of the stiffener reduces compared to the panel.

The results computed by numerical analyses and the difference between the numerical study and the literature are given in Table 2 and Table 3. Figure 12 illustrates the plots of normalized stress intensity factors (K_I/K_0) against the stiffness ratio (λ) for the different crack tip locations (a/b).

Table 2 Difference between FEM results with literature[19] for a/b=0.818

λ	Study in Literature	FEM Results			% Difference
	K_I/K_o	G_I (N/mm)	K_I (Mpa(mm)$^{1/2}$)	K_I/K_o	
0.5	0.83	16.07	1060.55	0.85	-1.95
1.0	0.87	17.01	1091.19	0.87	-0.65
2.0	0.90	18.24	1129.80	0.90	-0.16
3.0	0.92	18.99	1152.95	0.92	0.01
4.0	0.94	19.50	1168.33	0.93	0.62
6.0	0.95	20.16	1187.94	0.95	0.59
7.0	0.96	20.38	1194.52	0.95	0.41

Table 3 Difference between FEM results with literature [19] for a/b=0.923

λ	Study in Literature	FEM Results			% Difference
	K_I/K_o	G_I (N/mm)	K_I (Mpa(mm)$^{1/2}$)	K_I/K_o	
0.5	0.71	16.60	1077.96	0.70	0.39
1.0	0.75	17.77	1115.30	0.73	2.47
1.5	0.78	19.31	1162.63	0.76	2.27
2.0	0.80	20.40	1194.99	0.78	2.08
3.0	0.83	21.80	1235.31	0.80	2.45
4.0	0.85	23.09	1271.34	0.83	1.98
5.0	0.86	24.03	1296.82	0.84	1.99
6.0	0.88	24.96	1321.82	0.86	1.59
7.0	0.89	26.00	1349.07	0.88	0.80

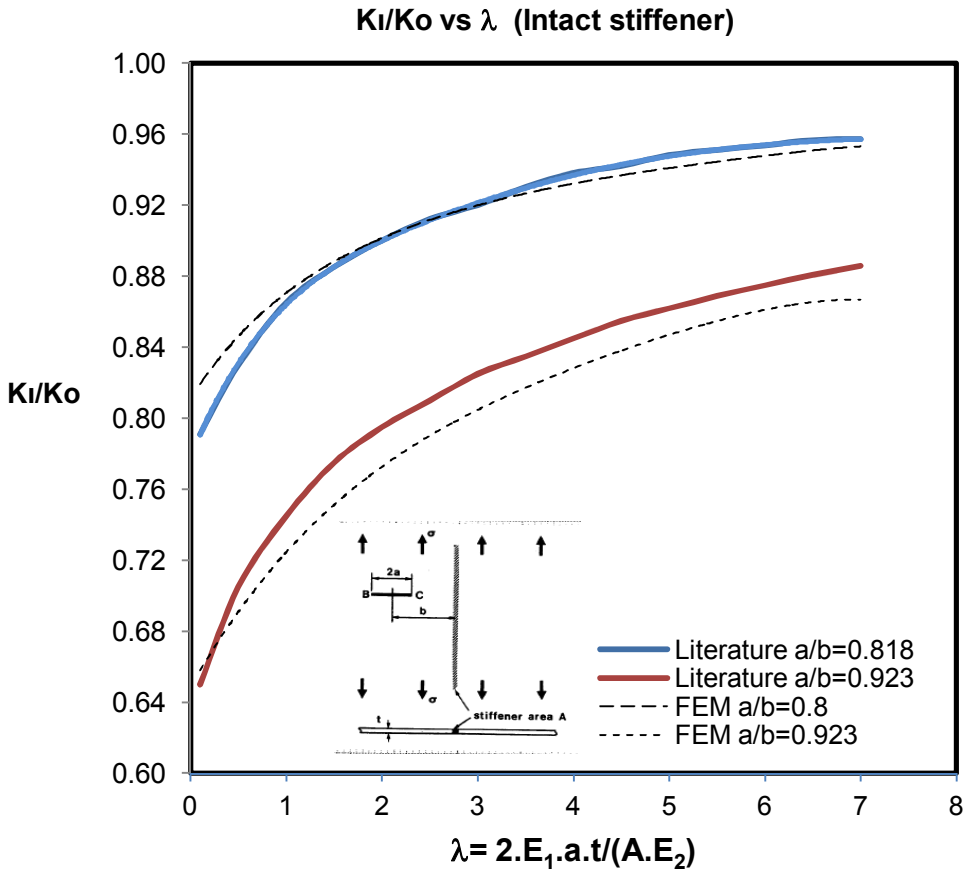

Figure 12 Comparison of numerical results with literature for intact stiffener case

2.3.2. Crack near a riveted stiffener on a sheet

As for a riveted stiffener in a sheet, the results obtained by FEM analysis are compared with the study of Bloom and Sanders [19]. In their study, Mode-I stress intensity factors are calculated by using complex stress functions and assuming zero in-plane bending stiffness of the stiffener.

The same material is used for the stiffener and the sheet in finite element model. The rivets are assumed as rigid circular inserts. For different a/b values, the stress intensity factor comparisons for λ=2 are given in Table 4 and Table 5, and the comparisions for λ=0.5 are given in Tables 7 – 9. The plots of normalized stress intensity factors (K_I/K_O) against the a/b are illustrated in Figure 14 and Figure 15 for λ=2 and λ=0.5 respectively. The influence of the stiffener on the opening of the crack tip passing through the stiffener is clearly observed in Figure 13, which shows the deformation results for different crack lengths.

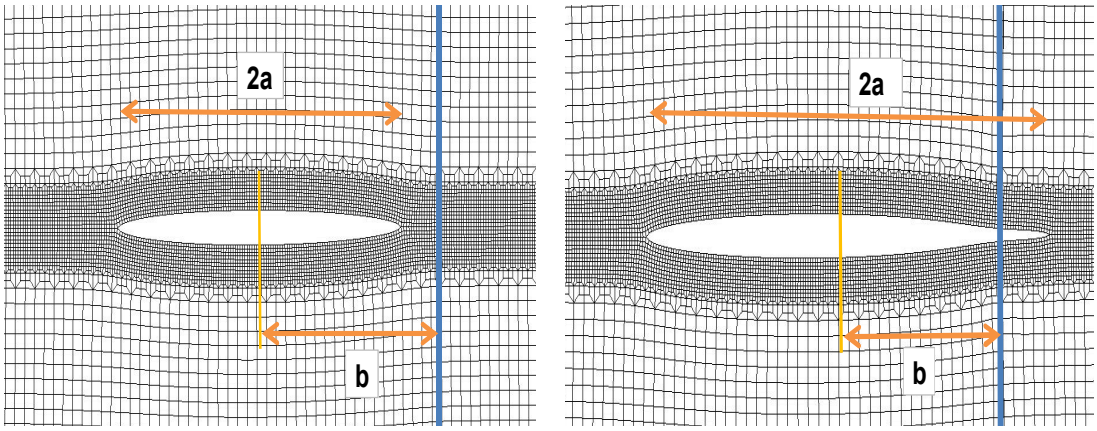

Figure 13 Different crack lengths in FEM

Table 4 Difference between FEM results with literature[19] for λ=2, a/h=0.5

a/b	Study in literature	FEM results				% difference
	K_I/K_0	G (N/mm)	K_0 (Mpa(mm)$^{1/2}$)	K_I (Mpa(mm)$^{1/2}$)	K_I/K_0	
0.84	0.90	7.25	792.67	712.44	0.90	0.13
0.90	0.88	6.89	792.67	694.48	0.88	-0.13
1.00	0.85	6.53	792.67	676.04	0.85	-0.69
1.10	0.83	6.19	792.67	658.31	0.83	-0.06
1.20	0.81	5.90	792.67	642.81	0.81	0.37
1.30	0.80	5.78	792.67	636.19	0.80	-0.07
1.40	0.80	5.68	792.67	630.44	0.80	-0.04

Table 5 Difference between FEM results with literature[19] for λ=2, a/h=1

a/b	Study in literature	FEM results				% difference
	KI/Ko	G (N/mm)	K_0 (Mpa(mm)$^{1/2}$)	K_I (Mpa(mm)$^{1/2}$)	KI/Ko	
0.60	0.95	4.75	614.00	576.39	0.94	1.18
0.70	0.92	7.14	772.59	706.82	0.91	0.56
0.80	0.89	11.34	1002.65	890.95	0.89	0.16
0.84	0.88	14.00	1121.00	989.95	0.88	-0.35
0.86	0.86	12.93	1121.00	951.37	0.85	1.32
0.90	0.81	11.76	1121.00	907.30	0.81	0.08
0.94	0.78	10.80	1121.00	869.40	0.78	0.57
1.00	0.73	9.69	1121.00	823.59	0.73	-0.64
1.10	0.66	7.93	1121.00	744.96	0.66	-0.69
1.20	0.62	7.03	1121.00	701.60	0.63	-1.77
1.30	0.59	6.38	1121.00	677.69	0.60	-1.91
1.40	0.58	6.39	1121.00	670.79	0.60	-2.86

Table 6 Difference between FEM results with literature [19] for λ=2, a/h=2

a/b	Study in literature	FEM results				% difference
	KI/Ko	G (N/mm)	K_0 (Mpa(mm)$^{1/2}$)	K_I (Mpa(mm)$^{1/2}$)	K_I/K_0	
0.60	0.95	9.12	840.75	799.17	0.95	-0.06
0.70	0.92	13.61	1048.60	976.06	0.93	-1.18
0.80	0.89	22.32	1372.94	1249.96	0.91	-1.69
0.84	0.87	29.00	1585.33	1424.78	0.89	-2.30
0.86	0.85	26.84	1585.33	1370.69	0.86	-1.72
0.90	0.80	24.31	1585.33	1304.49	0.82	-2.86
0.96	0.70	17.60	1585.33	1110.08	0.70	-0.03
1.00	0.61	14.10	1585.33	993.48	0.63	-2.73
1.04	0.51	9.70	1585.33	824.01	0.52	-1.92
1.10	0.47	8.09	1585.33	752.53	0.47	-2.08
1.20	0.44	7.14	1585.33	706.97	0.45	-2.52
1.30	0.42	6.83	1585.33	691.45	0.44	-2.87
1.40	0.42	6.81	1585.33	690.43	0.44	-2.96

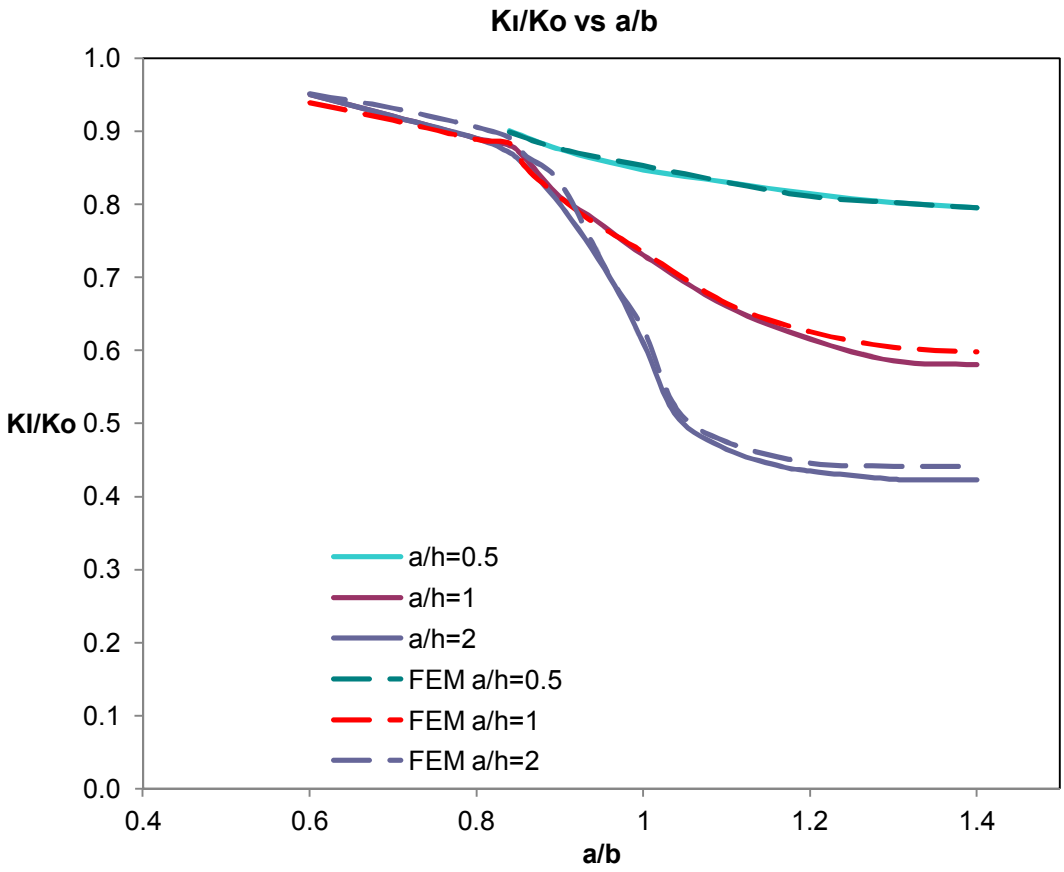

Figure 14 K_I/K_o vs a/b graphs for λ=2

Table 7 Difference between FEM results with literature[19] for λ=0.5, a/h=0.5

a/b	Study in literature	FEM results				Difference
	K_I/K_0	G (N/mm)	K_0 (Mpa(mm)$^{1/2}$)	K_I (Mpa(mm)$^{1/2}$)	K_I/K_0	
0.84	0.83	6.02	792.67	649.15	0.819	0.73%
0.90	0.80	5.80	792.67	637.18	0.804	-0.48%
1.00	0.75	5.00	792.67	591.61	0.746	0.49%
1.10	0.72	4.57	792.67	565.47	0.713	0.92%
1.25	0.68	4.22	792.67	543.51	0.686	-0.83%
1.30	0.67	4.09	792.67	534.87	0.675	-0.71%
1.40	0.67	3.98	792.67	527.56	0.666	-0.08%

Table 8 Difference between FEM results with literature[19] for λ=0.5, a/h=1

a/b	Study in literature	FEM results				% difference
	K_I/K_0	G (N/mm)	K_0 (Mpa(mm)$^{1/2}$)	K_I (Mpa(mm)$^{1/2}$)	K_I/K_0	
0.84	0.815	11.81	1121.00	909.23	0.811	0.48
0.86	0.79	10.62	1121.00	862.21	0.769	2.64
0.90	0.73	9.01	1121.00	794.17	0.708	2.95
0.94	0.69	8.20	1121.00	757.63	0.675	-2.05
1.00	0.62	6.51	1121.00	675.06	0.602	2.87
1.10	0.53	5.22	1121.00	604.48	0.539	-1.74
1.20	0.47	3.93	1121.00	524.50	0.468	0.45
1.30	0.461	3.72	1121.00	510.50	0.455	1.22
1.40	0.47	4.05	1121.00	532.71	0.475	-1.11

Table 9 Difference between FEM results with literature[19] for λ=0.5, a/h=2

a/b	Study in literature	FEM results				% difference
	K_I/K_0	G (N/mm)	K_0 (Mpa(mm)$^{1/2}$)	K_I (Mpa(mm)$^{1/2}$)	K_I/K_0	
0.80	0.83	18.20	1372.94	1128.72	0.822	0.95
0.84	0.8	22.92	1585.33	1266.65	0.799	0.13
0.86	0.79	22.00	1585.33	1240.97	0.783	0.91
0.90	0.72	18.93	1585.33	1151.13	0.726	-0.85
0.96	0.58	12.07	1585.33	919.18	0.580	0.03
1.00	0.5	9.05	1585.33	795.93	0.502	-0.41
1.04	0.4	5.80	1585.33	637.18	0.402	-0.48
1.10	0.36	4.81	1585.33	580.26	0.366	-1.67
1.16	0.335	4.09	1585.33	535.07	0.338	-0.75
1.20	0.33	4.01	1585.33	529.88	0.334	-1.28
1.30	0.355	4.37	1585.33	553.21	0.349	1.70
1.40	0.36	4.90	1585.33	585.66	0.369	-2.62

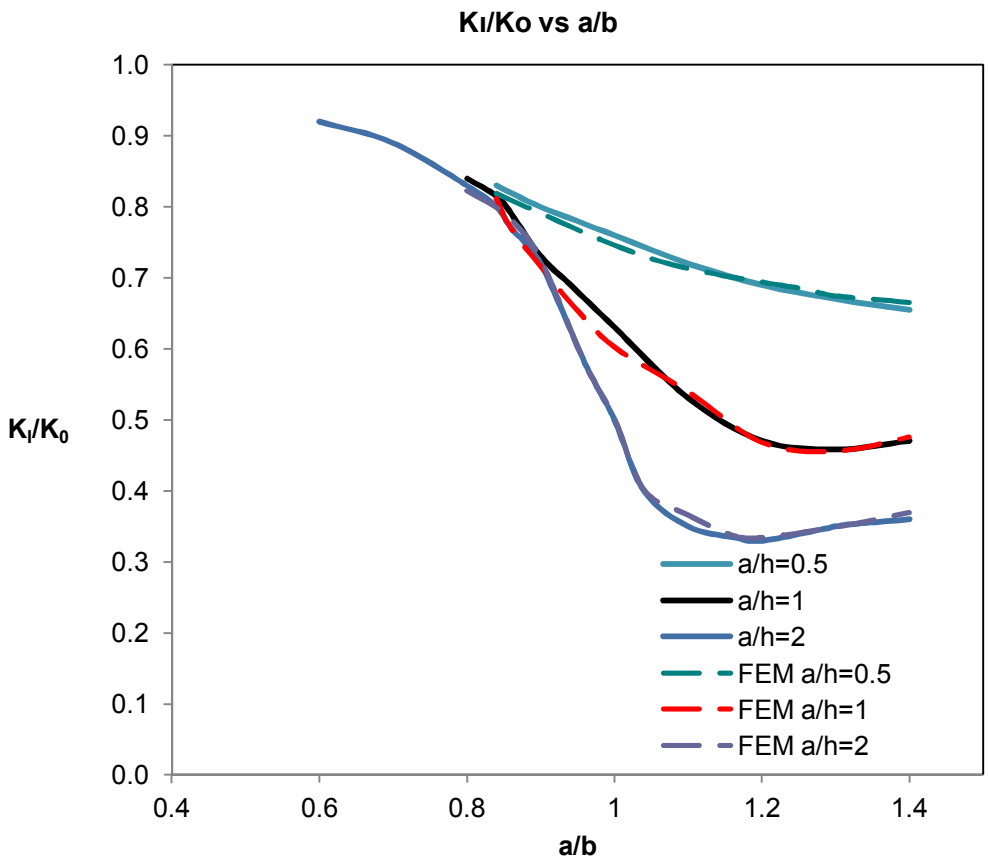

Figure 15 KI/Ko vs a/b graphs for λ=0.5

2.3.3. Inclined crack in a flat panel

A simple mixed mode crack problem is studied to verify numerical calculation in conjunction with VCCT under mixed mode condition. The results obtained by using VCCT are compared with the results calculated by analytical method.

The stress intensity factors KI and KII for an inclined central crack at the center of a sheet to uniform tensile loading are calculated by finite element analysis. The influence of different mesh sizes around crack tip and element types (Quad4 or Quad8) on the stress intensity factor calculations are investigated.

The finite element analysis is carried out for the angles of 5, 10, 15 and 20 between the crack direction and the perpendicular to the load direction.

The parameters used in finite element modeling are given in Table 10. The boundary conditions are illustrated in Figure 16.

Table 10 The parameters in FEM analysis

Panel dimension	10x10mm
The thickness of the plate	1 mm
Modulus of the material, E	70000 Mpa
Poisson's ratio, ν	0.33
Distributed load	200 Mpa
Global mesh size	1 mm
Crack Size (2a)	2 mm

The analytical solutions K_I and K_{II} for inclined crack on a plate are given as;

$$K_I = \sigma(sin\,\beta)^2\sqrt{\pi a} \tag{17}$$

$$K_{II} = \sigma(sin\,\beta\,cos\,\beta)^2\sqrt{\pi a} \tag{18}$$

$\beta = 90 - \alpha$

where β is the angle between the direction of the load and the crack plane, a is half of the crack size.

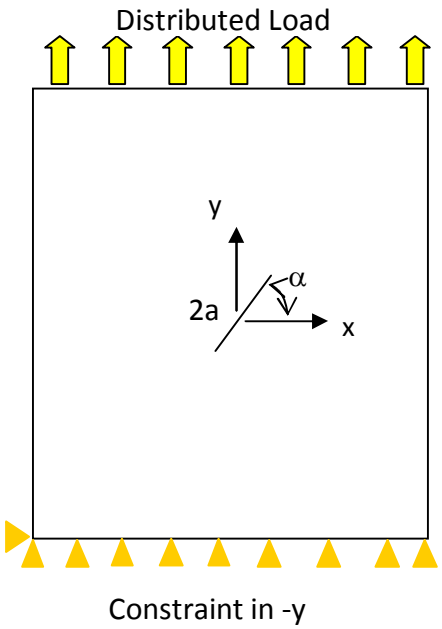

Figure 16 Boundary conditions in FEA for inclined cracked panel

The results for analytical solutions and FEM are presented in Table 11 - 16. The relative differences between the results are also given in tables. The results are also illustrated in graphical forms in Figure 17- 20. The graphs are separated according to element type. In the tables, the unit of the crack length, energy release rate and stress intensity factor are mm, N/mm and MPa$(m)^{1/2}$ respectively.

Table 11 Comparison of analytical and FEM results for crack tip element size 0.5 mm and element type Quad4

α	Analytical Solution		FEM Solution				Difference K_I	Difference K_{II}
	K_I	K_{II}	G_I	K_I	G_{II}	K_{II}		
5	11.12	0.97	1.592	10.56	0.009	0.79	5.1%	18.6%
10	10.87	1.92	1.521	10.32	0.037	1.60	5.1%	16.6%
15	10.46	2.80	1.363	9.77	0.089	2.50	6.6%	10.9%
20	9.90	3.60	1.224	9.26	0.145	3.18	6.5%	11.7%
25	9.21	4.29	1.056	8.60	0.210	3.83	6.6%	10.8%
35	7.52	5.27	0.710	7.05	0.316	4.70	6.3%	10.7%
45	5.60	5.60	0.391	5.23	0.368	5.08	6.7%	9.4%

Table 12 Comparison of analytical and FEM results for crack tip element size 0.1 mm and element type Quad4

α	Analytical Solution		FEM Solution				Difference-K_I	Difference-K_{II}
	K_I	K_{II}	G_I	K_I	G_{II}	K_{II}		
5	11.12	0.97	1.754	11.08	0.014	1.00	0.4%	-2.4%
10	10.87	1.92	1.668	10.81	0.052	1.91	0.6%	0.2%
15	10.46	2.80	1.548	10.46	0.108	2.75	0.5%	1.9%
20	9.90	3.60	1.381	9.83	0.183	3.58	0.7%	0.7%
25	9.21	4.29	1.198	9.16	0.255	4.23	0.5%	1.6%
35	7.52	5.27	0.795	7.46	0.385	5.19	0.8%	1.5%
45	5.60	5.60	0.442	5.56	0.439	5.54	0.8%	1.1%

Table 13 Comparison of analytical and FEM results for crack tip element size 0.01 mm and element type Quad4

α	Analytical Solution		FEM Solution				Difference-K_I	Difference-K_{II}
	K_I	K_{II}	G_I	K_I	G_{II}	K_{II}		
5	11.12	0.97	1.787	11.18	0.014	0.99	-0.5%	-2.1%
10	10.87	1.92	1.692	10.88	0.051	1.90	-0.1%	1.0%
15	10.46	2.80	1.586	10.54	0.113	2.81	-0.7%	-0.4%
20	9.90	3.60	1.422	9.98	0.187	3.62	-0.8%	-0.4%
25	9.21	4.29	1.235	9.30	0.258	4.25	-1.0%	1.0%
35	7.52	5.27	0.823	7.59	0.386	5.20	-0.9%	1.3%
45	5.60	5.60	0.459	5.67	0.441	5.56	-1.1%	0.9%

Table 14 Comparison of analytical and FEM results for crack tip element size 0.5 and element type Quad8

α	Analytical Solution		FEM Solution				Difference-K_I	Difference-K_{II}
	K_I	K_{II}	G_I	K_I	G_{II}	K_{II}		
5	11.12	0.97	1.833	11.33	0.015	1.01	-1.8%	-3.9%
10	10.87	1.92	1.752	11.07	0.056	1.98	-1.9%	-3.3%
15	10.46	2.80	1.469	10.14	0.103	2.69	3.0%	4.2%
20	9.90	3.60	1.314	9.59	0.171	3.46	3.1%	4.0%
25	9.21	4.29	1.138	8.92	0.242	4.12	3.1%	4.1%
35	7.52	5.27	0.757	7.28	0.365	5.05	3.2%	4.0%
45	5.60	5.60	0.420	5.42	0.415	5.39	3.3%	3.9%

Table 15 Comparison of analytical and FEM results for crack tip element size 0.1 and element type Quad8

α	Analytical Solution		FEM Solution				Difference-K_I	Difference-K_{II}
	K_I	K_{II}	G_I	K_I	G_{II}	K_{II}		
5	11.12	0.97	1.764	11.11	0.013	0.96	0.1%	1.9%
10	10.87	1.92	1.686	10.86	0.052	1.89	0.1%	0.9%
15	10.46	2.80	1.563	10.46	0.110	2.77	0.0%	1.0%
20	9.90	3.60	1.398	9.89	0.182	3.57	0.1%	1.0%
25	9.21	4.29	1.208	9.20	0.255	4.22	0.1%	1.6%
35	7.52	5.27	0.806	7.51	0.385	5.19	0.1%	1.4%
45	5.60	5.60	0.447	5.59	0.440	5.55	0.2%	1.0%

Table 16 Comparison of analytical and FEM results for crack tip element size 0.01 and element type Quad8

α	Analytical Solution		FEM Solution				Difference-K_I	Difference-K_{II}
	K_I	K_{II}	G_I	K_I	G_{II}	K_{II}		
5	11.12	0.97	1.782	11.22	0.014	0.99	-0.4%	-2.07%
10	10.87	1.92	1.715	10.96	0.054	1.96	-0.8%	-1.4%
15	10.46	2.80	1.597	10.57	0.110	2.77	-1.1%	1.0%
20	9.90	3.60	1.431	10.01	0.185	3.60	-1.1%	0.1%
25	9.21	4.29	1.240	9.32	0.261	4.27	-1.2%	0.5%
35	7.52	5.27	0.826	7.60	0.393	5.24	-1.1%	0.4%
45	5.60	5.60	0.458	5.66	0.446	5.59	-1.0%	0.3%

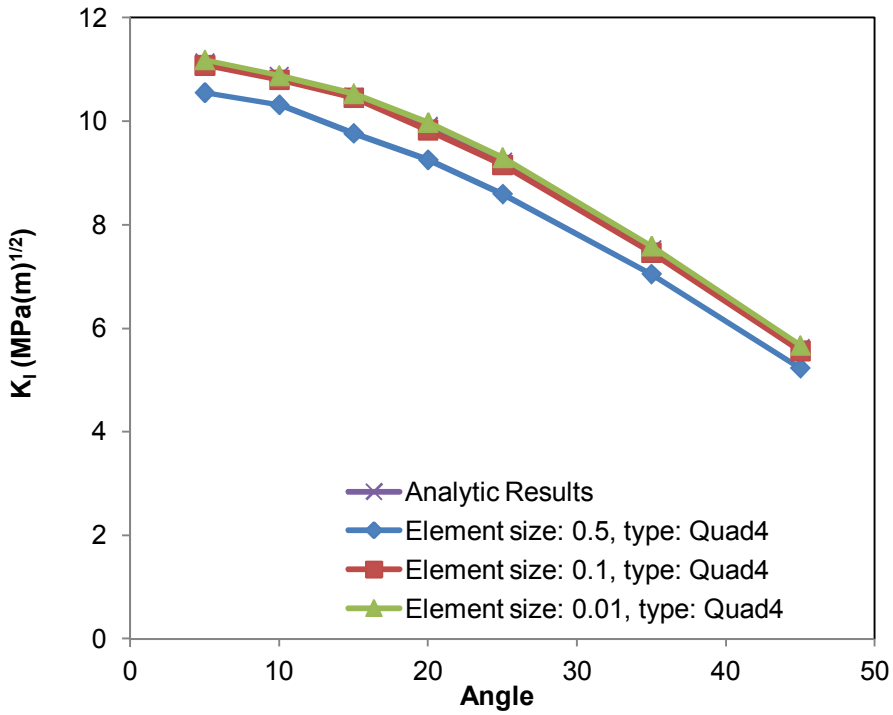

Figure 17 Comparison of numerical results and analytical solution for Mode-I Stress Intensity Factor, Type: Quad4

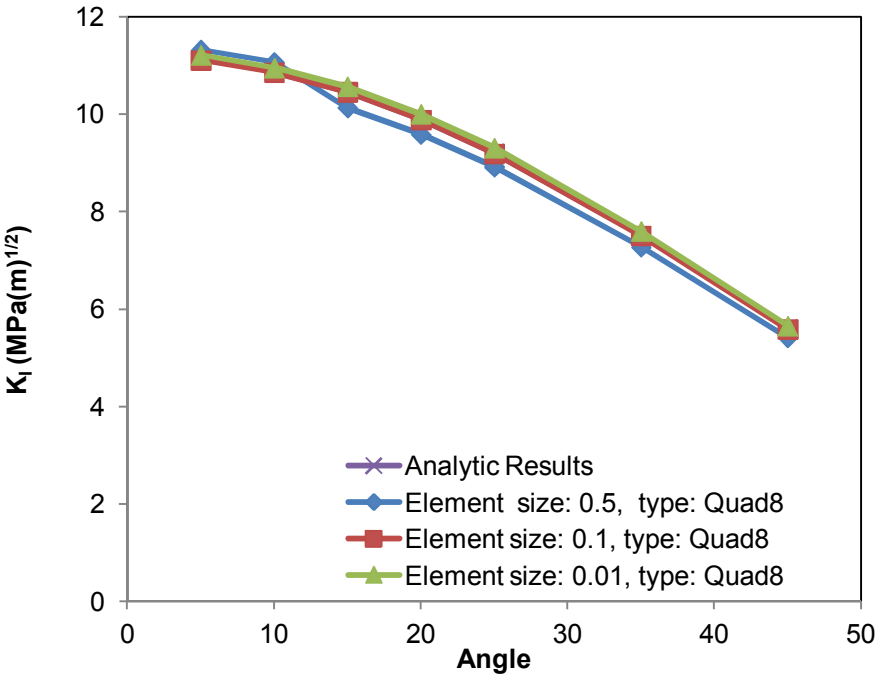

Figure 18 Comparison of numerical results and analytical solution for Mod-I stress intensity factor, Type: Quad8

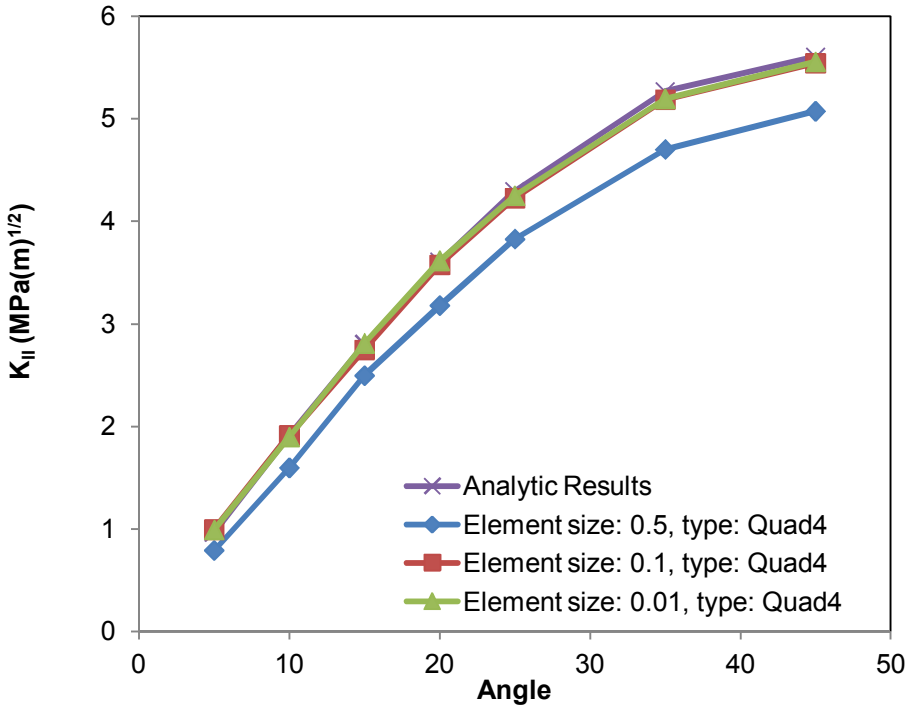

Figure 19 Comparison of numerical results and analytical solution for Mod-II stress intensity factor, Type: Quad4

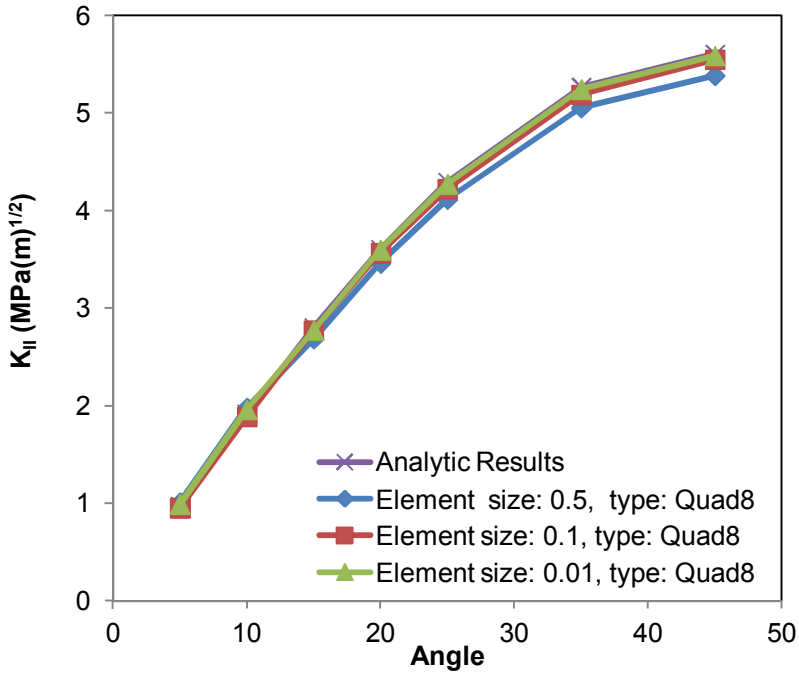

Figure 20 Comparison of numerical results and analytical solution for Mod-II stress intensity factor, element type Quad8

Von-misses stress distribution for a sample analysis (angle: 15 deg, tip element size: 0.1 mm) is shown in Figure 21. The high stress field around the crack tip is clearly seen.

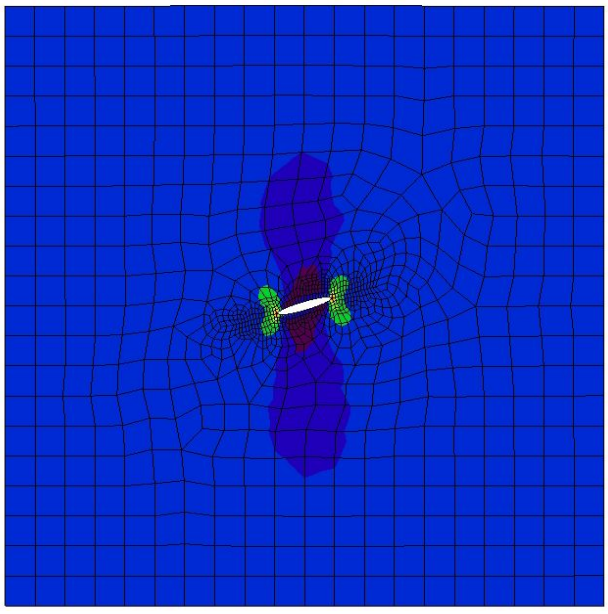

Figure 21 Von-misses stress distribution (α=15 deg, tip mesh=0.1 mm)

2.4. Conclusion

The results for the case studies of the stiffened panels and inclined cracked panel are discussed separately.

The comparative study for the cracked panel with intact stiffener shows that the calculated SIF values by finite element method agree well those from literature The difference between normalized stress intensity factors increases as the crack tip is getting closer to the stiffener but it does not exceed 2.5 %.

With regard to riveted stiffener case, the influences of different stiffness ratio values (λ) and rivet spacing (a/h) are investigated by the numerical solution. It is observed from Table 4 to Table 9 that difference between numerical solution and the values from literature increases as the stiffening effect is increased by reducing rivet spacing. Very precise results are obtained for the very low stiffening effect such as a/h = 0.5. The difference percentage do not exceed %1. The largest percentage of the difference is 3 % for $\lambda = 2$ and 3 % for $\lambda = 0.5$.

As for mixed mode condition of the cracked panel, Figure 17, Figure 18, Figure 19 and Figure 20 show that the values of SIF obtained by VCCT is very close to analytical solutions for the element size of 0.1 and 0.01 mm at the crack tip. The differences between the values obtained by VCCT and analytical solutions are not larger than 1.5 % for K_I and 2.5 % for K_{II} for those sizes. The difference is even not larger than 5 % for the most coarsed mesh size of 0.5 mm wlth Quad8 element type. It is concluded that the mesh size is directly affecting the accuracy of the numerical results. Another conclusion is that the further mesh refinement from 0.1 to 0.01 is unnecessary for the accuracy of the results. Regarding element type, the analyses with Quad8 give better results in general but the results for Quad4 with enough mesh refinement is sufficiently accurate.

The differences given from Table 11 to Table 16 demonstrate that the results for K_I are closer to analytical solutions than those for K_{II} for the small angles, at which K_I is more dominant than K_{II}.

It is possible to conclude that the numerical method using VCCT works well for the prediction of the stress intensity factor for the uniaxially loaded stiffened panel and for mixed-mode condition.

CHAPTER 3

AUTOMATIC CRACK PROPAGATION ANALYSIS

3.1. Crack Growth Direction

In order to perform crack growth simulation with unknown path, the crack growth direction should be determined at the crack tip. In this study the crack is extended by straight line segments. Hence the assumption is that the direction of crack propagation does not change through each straight segment.

There are various useful criteria used to predict the direction of the crack growth under mixed mode loading:

- the maximum circumferential stress [31]
- the minimum strain energy density [33]
- the maximum energy release rate [32]

The direction of the crack growth in the first criteria is estimated using information of the previous step. However an iterative calculation is required in the last two criteria. Both the minimum strain energy density criterion and the maximum circumferential stress criterion are most widely utilized to predict crack direction. Moreover various studies comparing these criteria are available in literature [12], [17].

Minimum strain energy density criterion is based on the strain energy around the crack tip. The extension of the crack takes place in the orientation which minimizes the energy. The crack will start to grow when the strain energy density factor becomes larger than the critical density factor, S_c. The accurate solution is related to the mesh density in the vicinity of the crack tip. The equation of the strain energy density factor is given as:

$$S = a_{11}k_1^2 + 2a_{12}k_1k_2 + a_{22}k_2^2 + a_{33}k_3^2 \tag{19}$$

where a_{11}, a_{12}, a_{22} and a_{33} are the coefficients relating to modulus of elasticity (E), polar angle (θ) and Poisson's ratio (ν).

In this study, the maximum circumferential stress criterion proposed by Erdogan and Sih [31] is used in order to predict the angle of the crack growth. According to the criterion, the crack tip will grow towards to the direction of the maximum tangential stress, $\sigma_{\theta\theta}$. Under general mixed mode loading, the circumferential and shear stresses near crack tip take the form:

$$\sigma_{r\theta} = \frac{K_I}{\sqrt{2\pi r}}\frac{1}{4}\left(3cos\left(\frac{\theta}{2}\right) + cos\left(\frac{3\theta}{2}\right)\right) + \frac{K_{II}}{\sqrt{2\pi r}}\frac{1}{4}\left(-3sin\left(\frac{\theta}{2}\right) - 3sin\left(\frac{3\theta}{2}\right)\right) \quad (20)$$

$$\sigma_{\theta\theta} = \frac{K_I}{\sqrt{2\pi r}}\frac{1}{4}\left(sin\left(\frac{\theta}{2}\right) + sin\left(\frac{3\theta}{2}\right)\right) + \frac{K_{II}}{\sqrt{2\pi r}}\frac{1}{4}\left(cos\left(\frac{\theta}{2}\right) + 3cos\left(\frac{3\theta}{2}\right)\right) \quad (21)$$

The shear stress, $\sigma_{r\theta}$ is set as zero because the circumferential stress, $\sigma_{\theta\theta}$ in the propagation direction is the principal stress. Then the following expression is obtained:

$$K_I sin\theta + K_{II}(3cos\theta - 1) = 0 \quad (22)$$

Extreme values of the angle are in case of K_{II} = 0,pure Mode-I, θ =0 and for pure Mode-II, θ=±70.50

Solution of the above equation leads to the crack propagation angle with respect to the crack face:

$$\theta = 2arctan\left(\frac{1}{4}\frac{K_I}{K_{II}} \pm \frac{1}{4}\sqrt{\frac{K_I}{K_{II}} + 8}\right) \quad (23)$$

The main advantage of the criterion is that it is simply implemented to finite element method. It is also supported by various test results. There are a number of authors applying this criterion in their works [12], [41], [16], [21]. Since the crack direction is determined by the relation between mode-I and mode-II stress intensity factors in the criterion, the application is limited to linear elastic fracture mechanics problems.

3.2. Crack Propagation with remeshing

In order to perform a fracture based fatigue analysis, at each crack size, even no change in boundary condition, the stress intensity factor should be computed. The values of the stress intensity factor with the crack length are later used to determine the fatigue life. Commercial softwares have the capability of the calculation of stress intensity factor by various methods such as virtual crack closure technique, J-integral, DCT (displacement correlation technique) etc. They have difficulties to adopt remeshing ability to crack growth analysis. Some of them have the limitation in remeshing ability in accordance with the analysis types and only support the simple geometries. There are studies for the development of software codes having the ability of crack growth analysis with remeshing. Some of these studies are mentioned in Chapter 1.

FRANC3D developed at Cornell University in 1980's is a software program to simulate crack growth in 3D models with adaptive remeshing capability [34]. The crack growth direction is predicted from the stress intensity factors in FRANC3D.

Another finite element code developed by NASA is STAGS (Structural Analysis and General Shells), which is used for the analysis of the structures modeled by shell elements [35]. STAGS was used to estimate the crack extension amount vs loading in conjunction with crack tip-opening angle (CTOA) criterion in a study [36], which is carried on the stiffened and unstiffened panels with singe cracks and MSD (multiple side damage cracking) at the edge of holes. Another study [21] on the center-crack panel problem presents the comparison of

the analysis results with the tests. The results on the far field stress against crack extension graphs showed good agreement with test for through crack plane stress modeling.

MSC.Marc/Mentat has the ability to perform crack propagation analysis with remeshing but it is limited to 2D solid models. It needs programming effort by user subroutines [37].

Abaqus has the ability to perform fracture analysis to compute the deviation of the crack path and the stress intensity factors. However it does not support automatic remeshing. Mixed-mode energy release rate estimation by VCCT can be performed by ANSYS, ABAQUS and MSC.Marc/Mentat [38], [37], [39].

Remeshing capability is crucial to simulate the growth of the crack as it changes the direction. It is not essential defining crack path with remeshing ability for the analysis of the situations with known crack path such as the composite delamination or simple boundary conditions leading to straight propagation. Some techniques, even for the analysis of the cracks with straight path requires that the finite element model should be arranged to make the meshes very fine around crack tip to capture the singularity for the estimation of the stress intensity factors.

The mesh density at the crack tip and the mesh quality in front of the crack tip are the parameters affecting the energy release rate estimation. In this study the analysis are carried out with different mesh sizes at the crack tip. Accurate stress intensity factors are obtained by VCCT by ensuring the straight crack path so the element edges in front of crack tip should be in the x direction of the local crack tip coordinate system (see Figure 22). Hence the remeshing algorithm will avoid the poor meshes shown in Figure 22(a). The edges of some elements at tip forward will lie on the x-direction of the crack tip system (see Figure 22(b)).

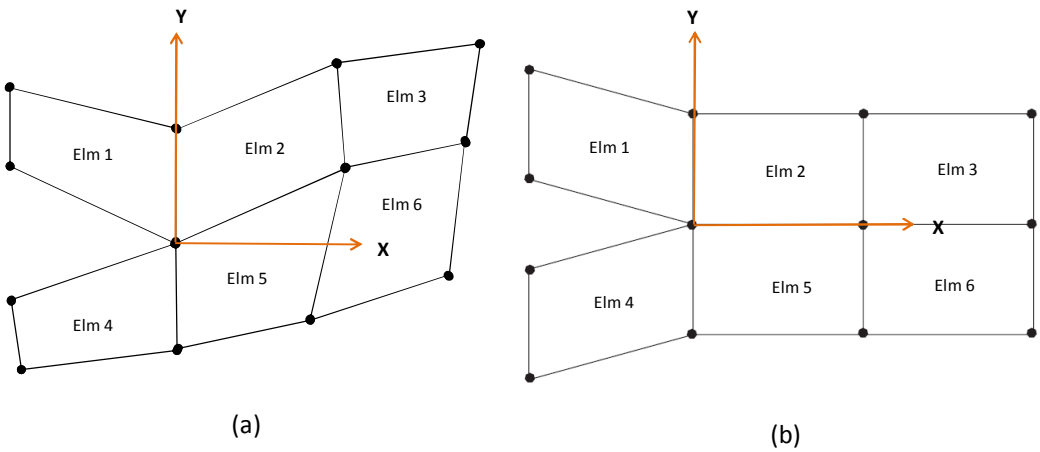

Figure 22 Meshing at the crack tip (a) poor mesh (b) good mesh

3.3. Crack Growth Procedure

The crack is grown quasi-statically by forming straight line segments at each step. The crack growth procedure to be followed in this study is shown in Figure 25. The method is developed to carry out automatic crack growth analysis for particularly stiffened panels, and it can be even adapted to any 2D model with crack. The first step is to build a global model including main load carriers such as frames, panels and stringers. The modeling will not get so detailed that the complex geometrical features is ignored. Then the detailed model of the stringer-panel configuration is prepared with holes, fasteners etc. The sub-model will be modified in case of a change in the fastener properties, fastener spacing and mesh size of the panel and the stringers. After specifying the initial crack location and the length on the sub-model, the rest of the analysis is carried out automatically by running the Fortran code, which activates MSC.Patran PCL code and MSC.Marc/Mentat as solver.

The Fortran code is prepared to handle stress intensity factor calculation by making use of the energy release rates computed by MSC.Marc/Mentat. In this study MSC.PATRAN is used as pre-processor and to make all arrangements regarding the mesh. The code runs the algorithms prepared by the programming language (Patran Command Language (PCL)) of MSC.Patran. The PCL is able to generate various finite element models and to create an application and forms [40]. The software code performs the crack growth propagation by discrete steps. At each cycle the crack is grown with the amount of predetermined length. Remeshing considering new crack path is fulfilled by the code programmed by PCL of MSC.Patran. Then finite element input file including model details is created for MSC.Marc/Mentat. After each crack increment, the computation of the crack growth direction and energy release rates is performed by procedure file of MSC.Marc/Mentat. The file indeed allows the user to sequentially execute a list of operations written in its own operating language and provides input parameters for VCCT analysis. The steps of the computational cycle are repeatedly executed many times up to the total crack size reaching the pre-defined length. Hence the FE calculation and model preparation are launched many times in a full automatic way. The extraction of multiple runs is written down as variations of stress intensity factor values along the crack path and the crack direction angle into a file.

The software code allows users to adjust the following parameters in finite element model:

1. The mesh size of the cracked panel model
2. The length of the crack increment
3. The mesh size in the vicinity of the crack tip
4. Selection of the element type as Quad4 or Quad8
5. The length of the initial crack
6. The mechanical properties and the thickness of the stiffener
7. Number of rivets and rivet spacing
8. The mechanical properties and size of the rivet
9. The mechanical properties and the thickness of the sheet

To perform automatic remeshing and to use different softwares for pre-processor and solver tasks result in some difficulties, which need to be resolved. Some of the issues, which should be taken into consideration for automatic crack growth analysis, are listed below:

- In order to avoid poor meshing in the vicinity at the crack tip, two-step meshing is implemented. At the first step meshes are generated for the whole structure. Then at

the second step the elements in the vicinity at the crack tip are removed and new mesh with good quality is created.

- The mesh needs to be split up to form crack path after remeshing. The mesh split is done at nodes lying on the crack path (see Figure 23).

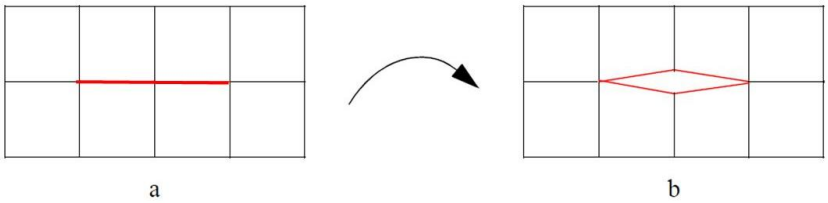

Figure 23 Mesh split at red edges [37]

- To compute stress intensity factor accurately, the mesh refinement in the vicinity of the crack tip is done. Finer mesh is only generated around the crack tip (see Figure 24) to reduce computational effort at the second step of meshing, which is aforementioned in the first item.

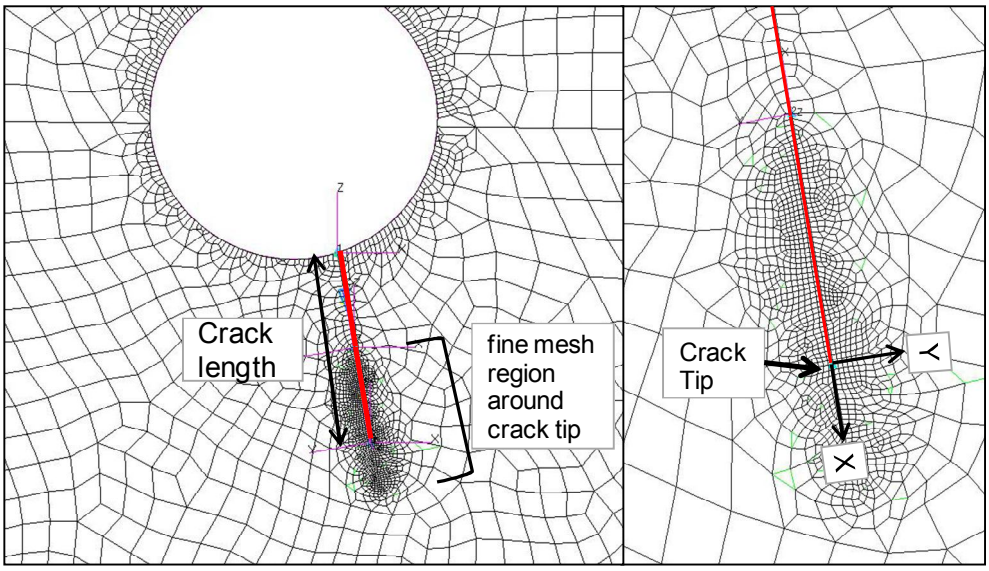

Figure 24 Fine mesh region around crack tip

- Reconnection of fasteners to newly generated elements after remeshing: The connections of the fasteners are recreated after each remeshing step because of new elements of the panel.

- Setting the boundary conditions for the new nodes after remeshing: The application regions of the displacements are modified by selecting new nodes.

- Identifying accurately the crack tip node for the solver software: The remeshing task is performed by pre-processor software MSC.Patran. Hence ID number of the crack tip node is identified by pre-processor after each crack increment and transferred to the solver MSC.Marc/Mentat as an input to crack parameters of VCCT option.

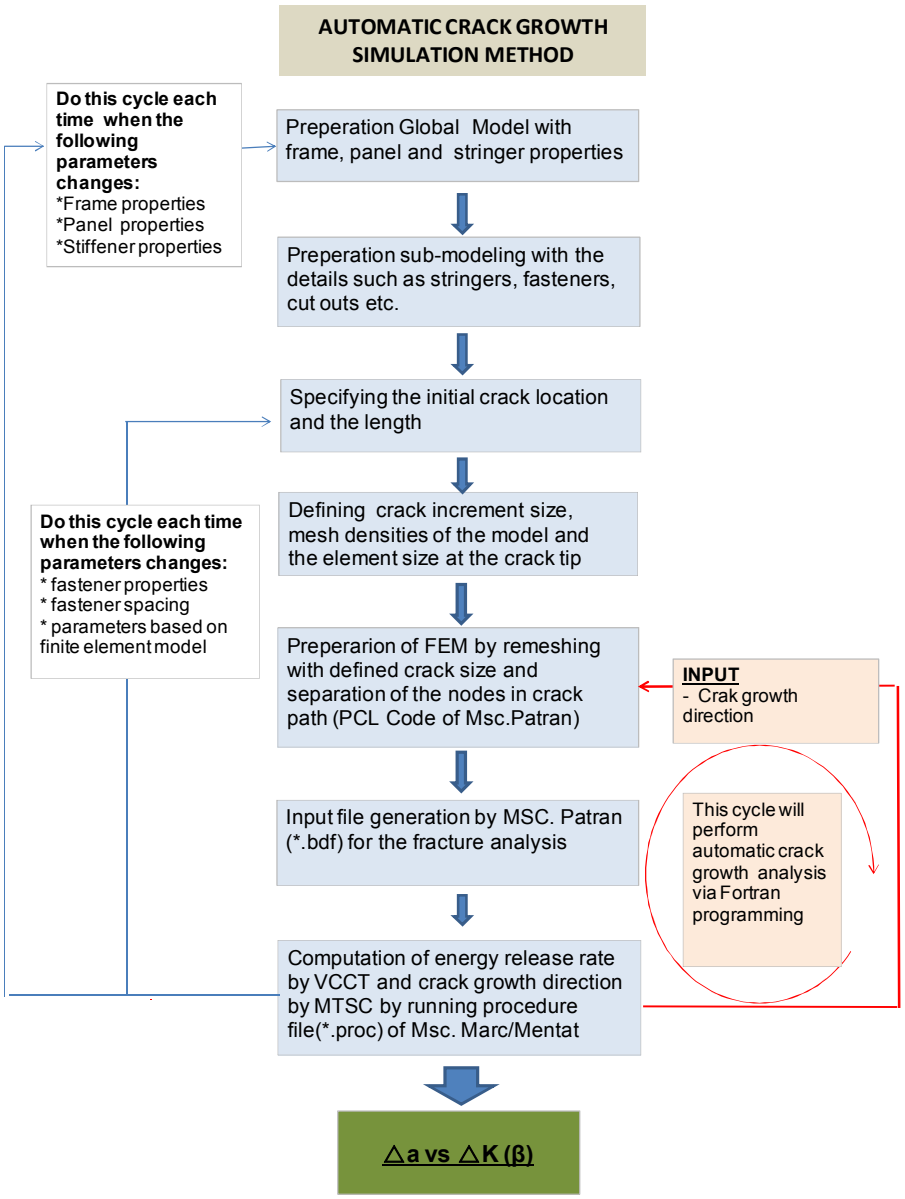

Figure 25 The method to be followed for automatic crack growth analysis

3.4. Crack Trajectory Prediction under Mixed Mode Loading

In this part of the thesis, the crack path predicted by the numerical method suggested in previous section is compared with several experimental studies from literature. Hence the validation of the method using the maximum circumferential stress criterion in conjunction with VCCT is provided. The effects of mesh size at the crack tip and the length of the crack increment on the crack path simulation are also studied by modifying the related parameters in the code developed in this study. In finite element analysis the crack path is formed by straight segments predicted from step by step increment technique. The stress intensity factors, the angle of the propagation direction in local coordinate system at the crack tip and crack tip positions are determined for corresponding crack extension.

The experiments from the literature are designed to obtain mixed-mode condition. The case studies are:

- Lateral force bending experiment
- Three point bending experiment with three holes

3.4.1. Numerical Crack Path Simulation for Lateral Force Bending Test

This experiment is performed on a flat plate made of steel St34 under lateral force by Theiler and Bucholz [22](see Figure 26). The lateral force of 1000 N applied to generate the mixed-mode condition through the specimen. The initial crack of the length a=2 mm is located on the fillet as shown in Figure 27. The thickness of the specimen is 15 mm. The other geometrical characteristics are illustrated in Figure 26. The mechanical characteristics of the material are E=210 GPa and v= 0.33.

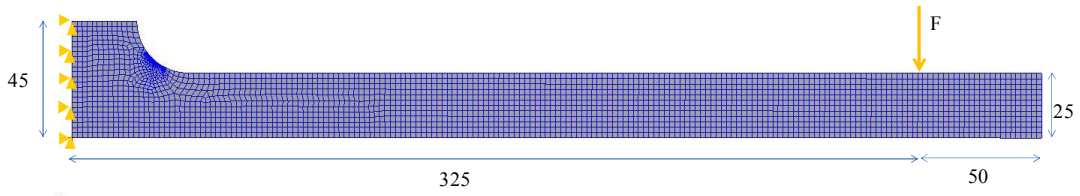

Figure 26 Finite element model for lateral force bending experiment

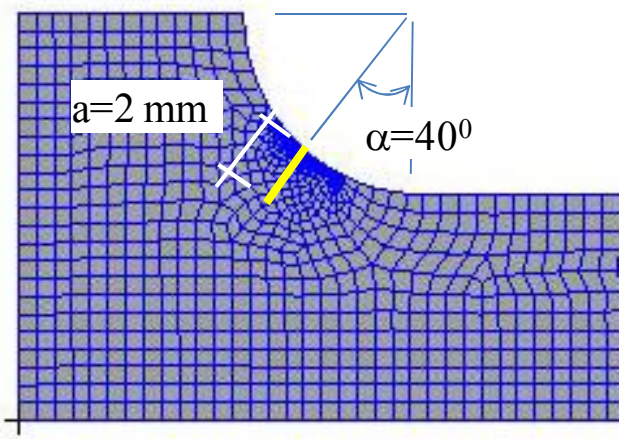

Figure 27 Initial crack detail for lateral force bending experiment

The crack path is simulated for various crack increment lengths and tip mesh sizes. Crack increment size is kept unchanged during the crack growth analysis. The stress intensity factors for each crack increment and the corresponding crack extension angles are listed from Table 17 to Table 20 for the tip mesh sizes of 0.05 mm, 0.2 mm, 0.5 mm and 1 mm, and in Table 21 and Table 23 for the crack increment sizes of 1 mm and 4 mm.

Table 17 The analysis results for crack increment size 2 mm and tip mesh size 0.05 mm

a (mm)	G_I (N/mm)	K_I (Mpa(m)$^{1/2}$)	G_{II} (N/mm)	K_{II} (Mpa(m)$^{1/2}$)	θ (degree)
2	0.62	11.43	7.70E-04	0.40	4.0
4	1.09	15.12	4.77E-03	1.00	7.5
6	1.62	18.47	3.37E-03	0.84	5.2
8	2.29	21.94	2.62E-03	0.74	3.9
10	3.21	25.95	2.09E-03	0.66	2.9
12	4.51	30.77	2.24E-03	0.69	2.6
14	6.51	36.97	2.24E-03	0.69	2.6
16	9.50	44.67	1.84E-03	0.62	0.0

Table 18 The analysis results for crack increment size 2 mm and tip mesh size 0.2 mm

Crack Incr.=2, Tip mesh=0.2

a (mm)	G_I (N/mm)	K_I (Mpa(m)$^{1/2}$)	G_{II} (N/mm)	K_{II} (Mpa(m)$^{1/2}$)	θ (degree)
2	0.62	11.39	7.40E-04	0.39	4.0
4	1.08	15.07	4.54E-03	0.98	7.4
6	1.61	18.41	3.28E-03	0.83	5.1
8	2.28	21.89	2.87E-03	0.78	4.1
10	3.18	25.86	2.44E-03	0.72	3.2
12	4.47	30.65	1.54E-03	0.57	2.1
14	6.41	36.68	2.02E-03	0.65	2.0
16	9.50	44.67	1.84E-03	0.62	1.6

Table 19 The analysis results for crack increment size 2 mm and tip mesh size 0.5 mm

Crack Incr.=2, Tip mesh=0.5

a (mm)	G_I (N/mm)	K_I (Mpa(m)$^{1/2}$)	G_{II} (N/mm)	K_{II} (Mpa(m)$^{1/2}$)	θ (degree)
2	0.56	11.43	3.00E-04	0.25	2.7
4	1.02	15.12	6.02E-03	1.12	8.7
6	1.56	18.47	2.65E-03	0.75	4.7
8	2.22	21.94	2.39E-03	0.71	3.8
10	3.08	25.95	2.65E-03	0.75	3.4
12	4.33	30.77	1.70E-03	0.60	2.3
14	6.11	36.97	2.13E-03	0.67	2.1
16	9.01	44.67	7.00E-05	0.12	0.3

Table 20 The analysis results for crack increment size 2 mm and tip mesh size 1 mm

Crack Incr.=2, Tip mesh=1

a (mm)	G_I (N/mm)	K_I (Mpa(m)$^{1/2}$)	G_{II} (N/mm)	K_{II} (Mpa(m)$^{1/2}$)	θ (degree)
2	0.58	11.02	4.40E-04	0.30	3.1
4	1.02	14.63	4.46E-03	0.97	7.5
6	1.51	17.83	3.72E-03	0.88	5.6
8	2.17	21.35	2.77E-03	0.76	4.1
10	3.09	25.47	1.64E-03	0.59	2.6
12	4.29	30.02	2.92E-03	0.78	3.0
14	6.17	36.00	1.20E-03	0.50	1.6
16	11.32	48.75	3.91E-03	0.91	2.1

Table 21 The results for crack increment size 1 mm and tip mesh size 0.05 mm

Crack Incr.=1, Tip mesh=0.05

a (mm)	G_I (N/mm)	K_I (Mpa(m)$^{1/2}$)	G_{II} (N/mm)	K_{II} (Mpa(m)$^{1/2}$)	θ (degree)
2	0.63	11.54	2.57E-03	0.73	7.2
3	0.85	13.37	3.00E-05	0.08	0.7
4	1.11	15.26	9.00E-04	0.43	3.3
5	1.36	16.93	7.80E-04	0.40	2.7
6	1.65	18.61	8.10E-04	0.41	2.5
7	1.96	20.30	7.00E-04	0.38	2.2
8	2.33	22.10	6.90E-04	0.38	2.0
9	2.75	24.05	4.30E-04	0.30	1.4
10	3.25	26.12	6.10E-04	0.36	1.6
11	3.85	28.44	4.80E-04	0.32	1.3
12	4.57	30.99	4.70E-04	0.31	1.2
13	5.47	33.89	4.60E-04	0.31	1.0
14	6.57	37.14	4.00E-04	0.29	0.9
15	7.97	40.92	3.20E-04	0.26	0.7
16	9.76	45.28	4.70E-04	0.31	0.8

Table 22 The results for crack increment size 4 mm and tip mesh size 0.05 mm

a (mm)	G_I (N/mm)	K_I (Mpa(m)$^{1/2}$)	G_{II} (N/mm)	K_{II} (Mpa(m)$^{1/2}$)	θ (degree)
2	0.62	11.43	7.70E-04	0.40	4.0
6	1.55	18.02	2.10E-02	2.10	13.0
10	3.12	25.59	1.05E-02	1.49	6.6
14	6.28	36.31	8.34E-03	1.32	4.2

Table 23 Comparisons of stress intensity factors for different tip meshes

a (mm)	Tip mesh=0.05	Tip mesh=0.2		Tip mesh=0.5		Tip mesh=1	
	K_I (Mpa(m)$^{1/2}$)	K_I (Mpa(m)$^{1/2}$)	Diff.	K_I (Mpa(m)$^{1/2}$)	Diff.	K_I (Mpa(m)$^{1/2}$)	Diff.
2	11.43	11.39	0.4%	10.84	5.2%	11.02	3.6%
4	15.12	15.07	0.3%	14.65	3.1%	14.63	3.2%
6	18.47	18.41	0.3%	18.09	2.0%	17.83	3.4%
8	21.94	21.89	0.2%	21.57	1.7%	21.35	2.7%
10	25.95	25.86	0.3%	25.42	2.0%	25.47	1.8%
12	30.77	30.65	0.4%	30.16	2.0%	30.02	2.4%
14	36.97	36.68	0.8%	35.82	3.1%	36.00	2.6%
16	45.09	44.67	0.9%	43.50	3.5%	48.75	-8.1%

It can be concluded From Table 23 that the size of the mesh, which is larger than 0.2 mm affects the precision of the computation. In contrast, the analyses with the mesh sizes smaller than 0.2 mm yield very close SIF values to those with the finest mesh size of 0.05 mm.

Figure 28 shows the picture of cracked specimen after fatigue experiment and finite element model with the crack.

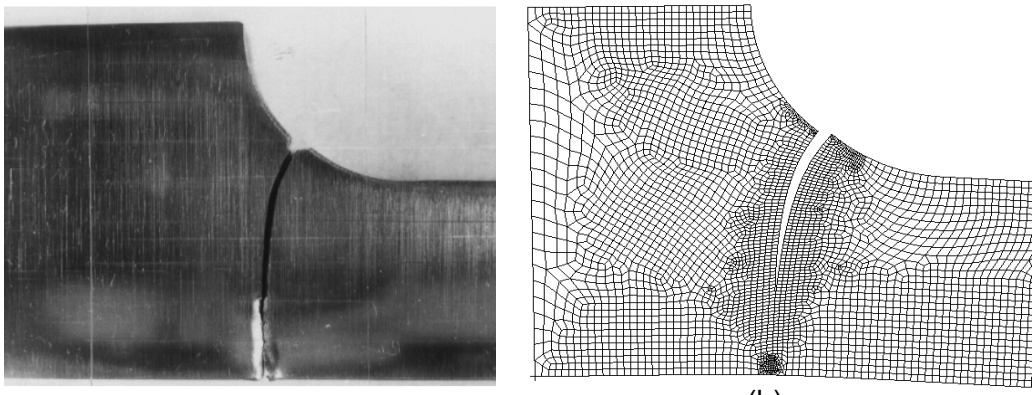

(a) (b)

Figure 28 Crack paths for experiment (a) [22] and numerical studies (b)

Experimentally obtained and simulated crack paths with different tip crack meshes and crack increment sizes are illustrated in Figure 29. The mesh sizes around the crack tip are not much influential on the crack trajectory. Although the computational results of stress intensity factor for the mesh size of 1 mm differ from the results for the mesh size of 0.05 mm about 4%, it does not affect the prediction of the crack path. With regard to the effect of crack increment size, the simulated results deviate from the experimental crack path with the increase in the increment size. The simulated crack trajectories for the increment sizes of 1 mm and 2 mm show good correlation with experimental result.

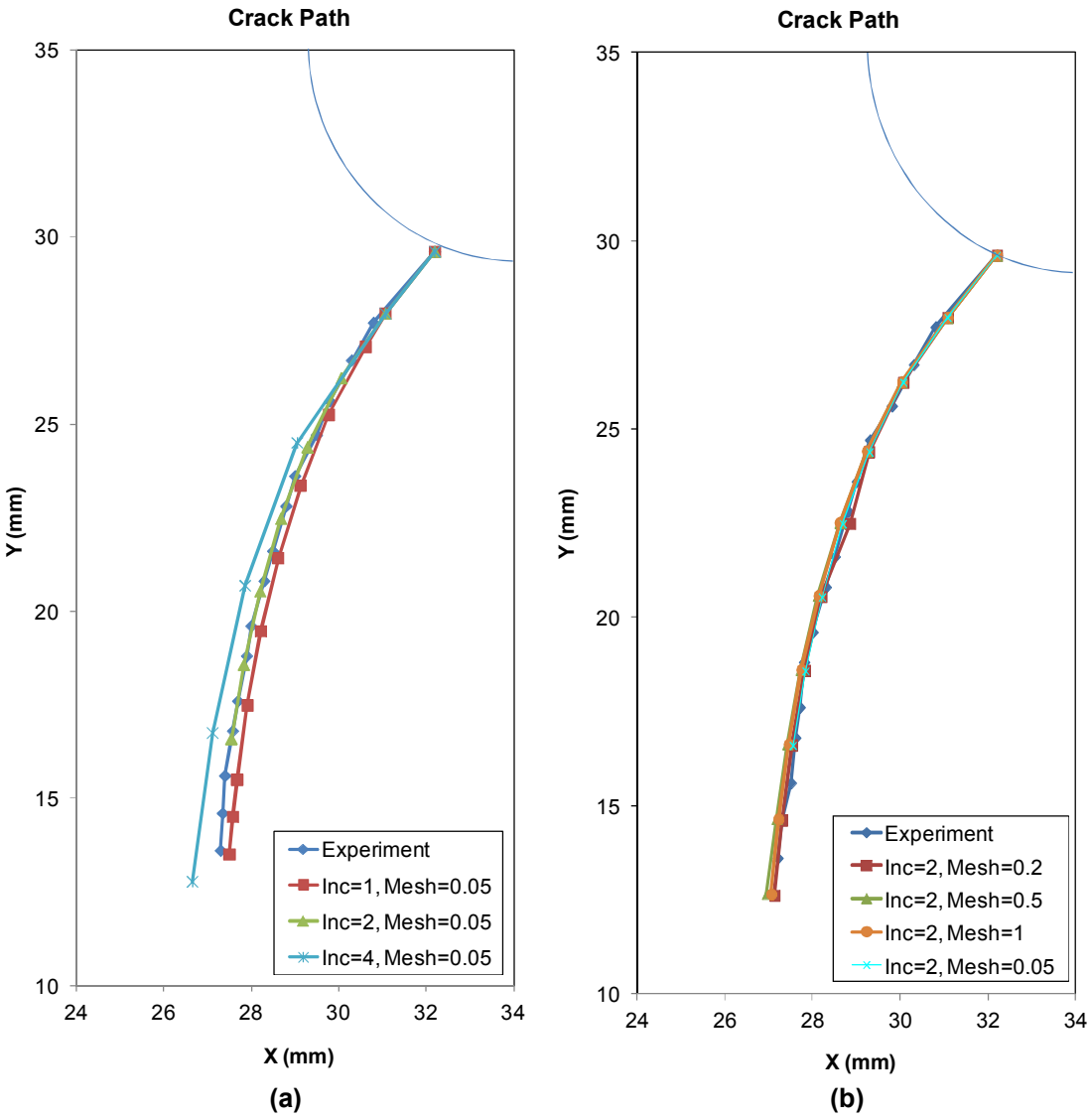

Figure 29 Crack trajectories for different lengths of the crack increment (a) and for the different mesh densities at the crack tip (b)

3.4.2. Numerical Crack Path Simulation for Three Point Bending Test

This experiment is executed for the crack path evaluation of a beam loaded in the center and supported by two points. The geometric features of the specimen are illustrated in Figure 30.

The beam has three holes, which deviate the crack trajectory. Some researchers [16], [42], [43] have simulated the crack path for this experiment by finite element analysis. The length of the initial crack is 25.4 mm. Its location is 101.6 mm away from the edge of the beam. The element sizes at the crack tip examined in this case study are 1 mm, 2 mm and 3 mm. Three different values of the increment as 10 mm, 15 mm, 20 mm and 30 mm are considered for this problem.

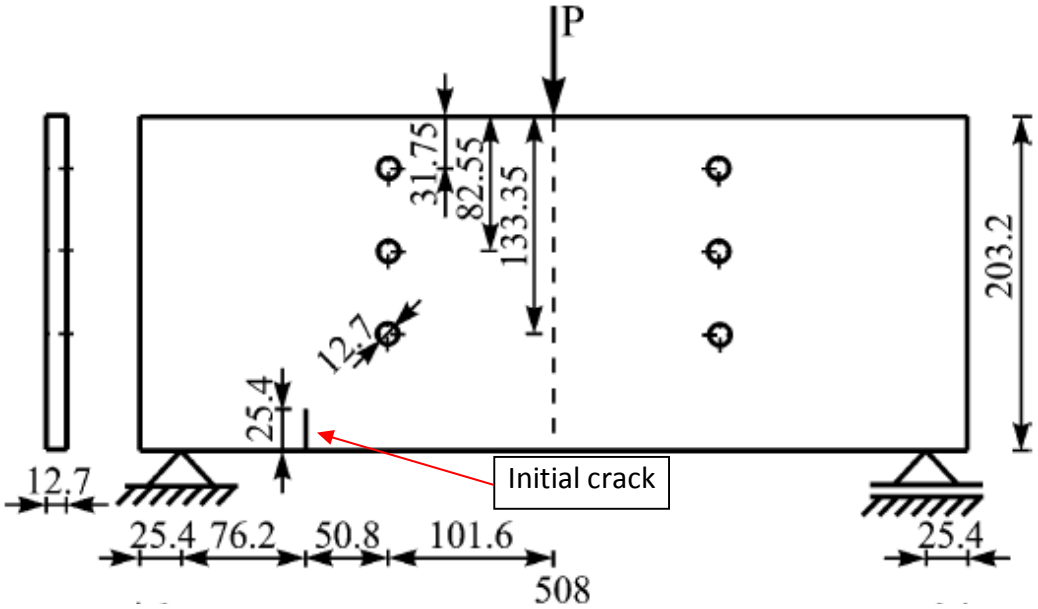

Figure 30 Geometrical features of three point bending test specimen (all dimensions are in mm) [16]

The simulation results for different element sizes at the crack tip (1 mm, 2 mm and 3mm) are presented in Table 24, Table 25and Table 26. The simulation results; SIF values and the angle of crack extensions for the crack increment lengths of 10 mm, 15mm, 20 mm and 30 mm are given in

Table 28, Table 29 and Table 30 respectively.

The differences between K_I values from the simulation with the smallest element size (1 mm) and the values from the simulations with larger element sizes (2 mm and 3 mm) are given in Table 27. It is observed that mesh refinement around the crack tip affects the accuracy of SIF values. The difference between K_I values for 1 mm and 3 mm mesh sizes is about 5 %.

Table 24 The results for crack increment length 15 mm and tip mesh size 1 mm

Crack incr.=15, Tip mesh=1

a (mm)	G_I (N/mm)	K_I (Mpa(m)$^{1/2}$)	G_{II} (N/mm)	K_{II} (Mpa(mm)$^{1/2}$)	θ (degree)
25.4	26.74	8.96	3.40E-01	1.01	12.6
40.4	45.88	11.73	1.27E-01	0.62	6.0
55.4	73.50	14.85	1.88E-01	0.75	5.8
70.4	120.63	19.02	1.70E-01	0.71	4.3
85.4	182.48	23.40	9.60E-02	0.54	2.6

100.4	281.86	29.08	2.66E-02	0.28	1.1
115.4	474.76	37.74	4.67E-01	1.18	3.6

Table 25 The results for crack increment length 15 mm and tip mesh size 2 mm

Crack incr.=15, Tip mesh=2

a (mm)	G_I (N/mm)	K_I (Mpa(m)$^{1/2}$)	G_{II} (N/mm)	K_{II} (Mpa(m)$^{1/2}$)	θ (degree)
25.4	27.66	9.11	3.33E-01	1.00	12.2
40.4	44.47	11.55	1.55E-01	0.68	6.7
55.4	74.87	14.99	1.45E-01	0.66	5.0
70.4	117.35	18.76	1.87E-01	0.75	4.6
85.4	177.66	23.09	8.44E-02	0.50	2.5
100.4	274.36	28.69	1.85E-02	0.24	0.9
115.4	482.53	38.05	3.76E-01	1.06	3.2

Table 26 The results for crack increment length 15 mm and tip mesh size 3 mm

Crack incr.=15, Tip mesh=3

a (mm)	G_I (N/mm)	K_I (Mpa(m)$^{1/2}$)	G_{II} (N/mm)	K_{II} (Mpa(m)$^{1/2}$)	θ (degree)
25.4	26.83	8.97	3.32E-01	1.00	12.4
40.4	49.96	12.24	1.49E-01	0.67	6.2
55.4	70.38	14.53	1.43E-01	0.66	5.1
70.4	110.66	18.22	1.38E-01	0.64	4.0
85.4	166.09	22.32	1.48E-01	0.67	3.4
100.4	256.98	27.77	3.95E-02	0.34	1.4
115.4	429.43	35.89	4.77E-02	0.38	1.2

Table 27 Difference between K_I values with different element sizes at the crack tip

a (mm)	Crack incr.=15, Tip mesh=1	Crack incr.=15, Tip mesh=2		Crack incr.=15, Tip mesh=3	
	K_I (Mpa(m)$^{1/2}$)	K_I (Mpa(m)$^{1/2}$)	Difference	K_I (Mpa(m)$^{1/2}$)	Difference
25.4	8.96	9.11	1.4%	8.97	0.2%
40.4	11.73	11.55	-1.5%	12.24	4.4%
55.4	14.85	14.99	0.9%	14.53	-2.1%
70.4	19.02	18.76	-1.4%	18.22	-4.2%
85.4	23.40	23.09	-1.3%	22.32	-4.6%
100.4	29.08	28.69	-1.3%	27.77	-4.5%
115.4	37.74	38.05	0.8%	35.89	-4.8%

Table 28 The results for crack increment length 10 mm and tip mesh size 1 mm

Crack incr.=10, Tip mesh=1

a (mm)	G_I (N/mm)	K_I (Mpa(m)$^{1/2}$)	G_{II} (N/mm)	K_{II} (Mpa(m)$^{1/2}$)	θ (degree)
25.4	26.74	8.96	3.40E-01	1.01	12.6
35.4	40.08	10.96	4.88E-02	0.38	4.0
45.4	55.47	12.90	7.41E-02	0.47	4.2
55.4	75.85	15.08	7.08E-02	0.46	3.5
65.4	102.87	17.57	5.70E-02	0.41	2.7
75.4	137.20	20.29	6.64E-02	0.45	2.5
85.4	179.52	23.21	3.19E-02	0.31	1.5
95.4	236.38	26.63	9.20E-04	0.05	0.2
105.4	328.37	31.39	8.49E-02	0.50	1.8
115.4	486.87	38.22	7.89E-01	1.54	4.6

Table 29 The results for crack increment length 20 mm and tip mesh size 1 mm

Crack incr.=20, Tip mesh=1

a (mm)	G_I (N/mm)	K_I (Mpa(mm)$^{1/2}$)	G_{II} (N/mm)	K_{II} (Mpa(mm)$^{1/2}$)	θ (degree)
25.4	26.72	8.95	3.38E-01	1.01	12.5
45.4	54.37	12.77	3.20E-01	0.98	8.7
65.4	100.98	17.41	3.07E-01	0.96	6.3
85.4	177.35	23.07	2.01E-01	0.78	3.8
105.4	325.55	31.25	7.62E-02	0.48	1.8

Table 30 The results for crack increment length 30 mm and tip mesh size 1 mm

a (mm)	G_I (N/mm)	K_I (Mpa(mm)$^{1/2}$)	G_{II} (N/mm)	K_{II} (Mpa(mm)$^{1/2}$)	θ (degree)
25.4	26.72	8.95	3.38E-01	1.01	12.5
55.4	71.92	14.69	9.30E-01	1.67	12.7
85.4	174.70	22.89	4.19E-01	1.12	5.6
115.4	478.64	37.89	9.57E-02	0.54	1.6

With regard to the effect of the crack increment length and mesh density on the crack trajectory, the comparison among the simulation results and experimental measurements of crack trajectories is given in Figure 32 and Figure 33. The crack tip locations are given in coordinate system illustrated in Figure 31. The crack paths from finite element method, which extend up to the middle hole in the plate as shown in Figure 31 are consistent with the experimental observations. With the increase in crack increment length, the simulated path is

getting away from the path experimentally obtained. Another observation is that the effect of element sizes used in the analyses is not significant on the crack trajectory.

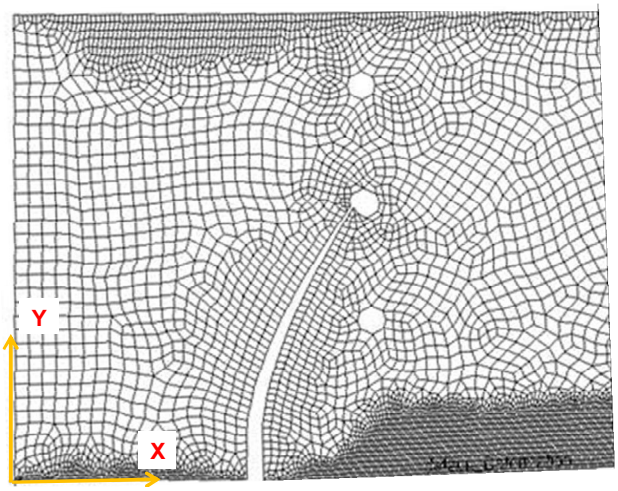

Figure 31 Crack trajectory simulated by FEA

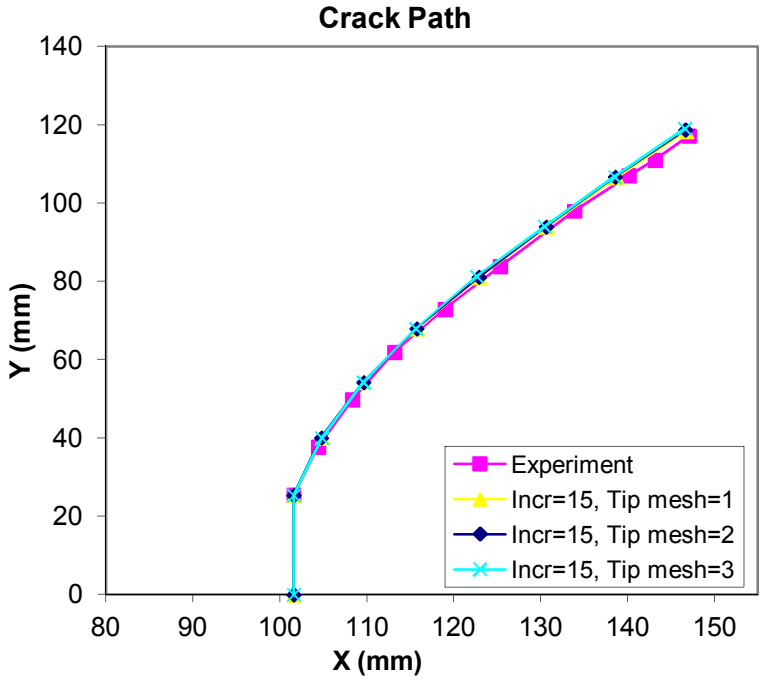

Figure 32 Comparision of crack trajectories for different mesh densities and experiment

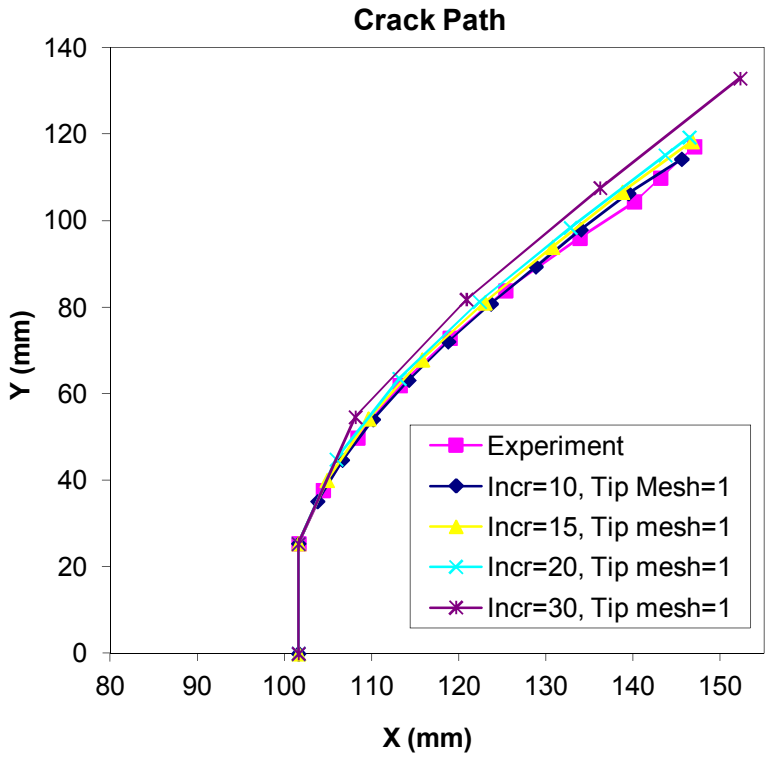

Figure 33 Comparision of crack trajectories from simulations with different crack increment lengths and from experiment

CHAPTER 4

LIFE ASSESMENT OF A STIFFENED HELICOPTER PANEL

4.1. Introduction

In this study tail boom portion of a helicopter is analyzed. The structural parts of helicopter tail portion are illustrated in Figure 34. Boundary conditions and finite element modeling technique are described in forthcoming sections. The fracture analysis of a particular portion of the helicopter fuselage is executed by using finite element method described in previous section.

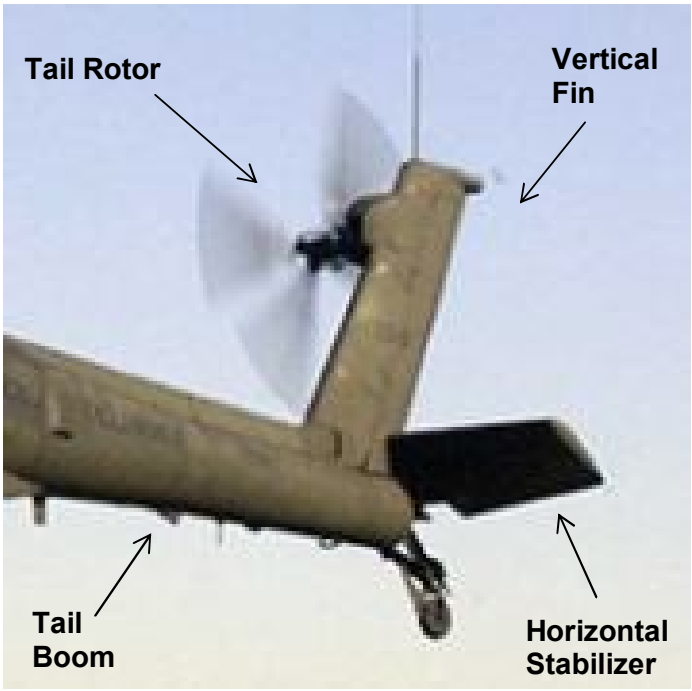

Figure 34 Tail boom structure of a helicopter

The panels of the fuselage structure are supported by stringers and frames. Stringer shape is chosen as Z-cross section. There are various types of stringers, which are used through the fuselage structures. Some common examples are shown in Figure 35. The stringers and frames are fixed to the panels by riveting process. The material of the panels, stringers and frames are aluminum alloy.

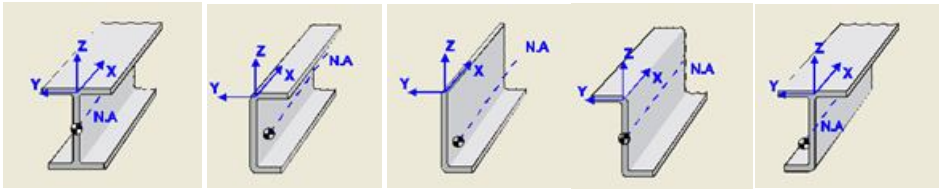

Figure 35 Various stiffener types

The dimensions of stringer and frame used in the fuselage structure are determined as shown in Figure 36.

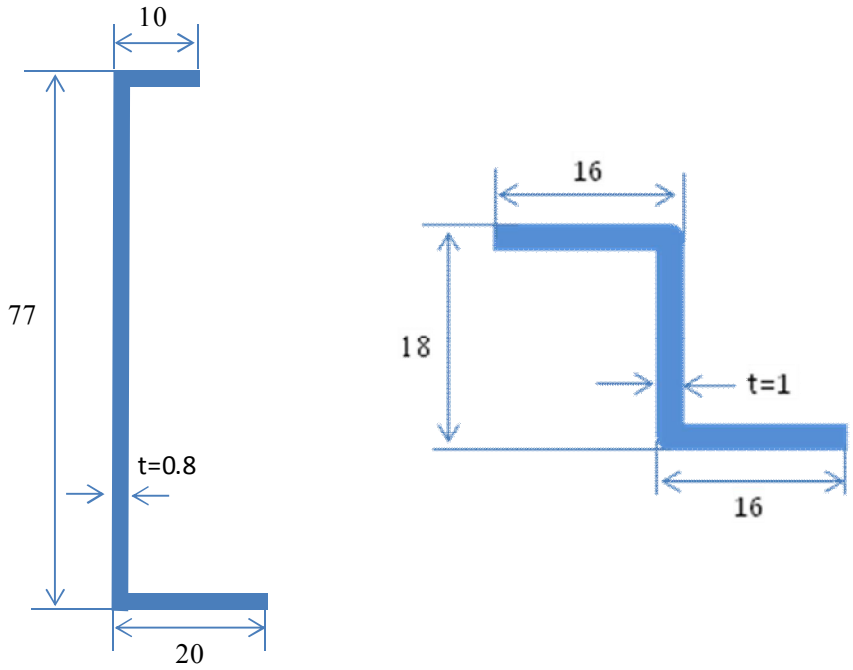

Figure 36 The dimensions of the frame and the stringer which are used in the analysis (the dimensions are in mm)

4.2. Boundary Conditions

4.2.1. Description of Boundary Conditions

As shown in Figure 37, the boom section is connected to the rest of the fuselage by the bolts. The nodes corresponding to the same location with the bolts are constrained at the six degrees of freedom. Thrust load of tail rotor is applied as point load. The direction of the thrust load is the perpendicular to the plane of tail vertical fin. The boundary conditions will not change during the fracture analysis.

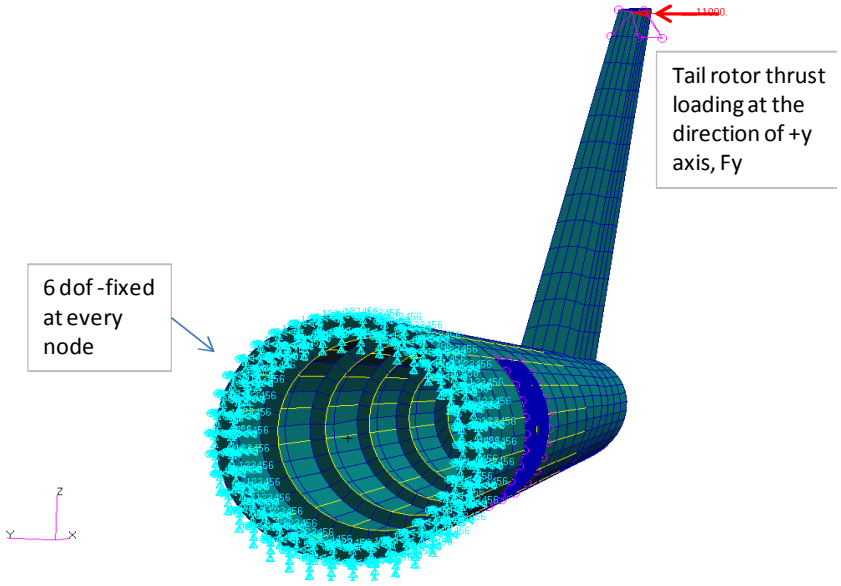

Figure 37 Boundary conditions of the global model

4.2.2. Loading Spectrum

In order to perform fatigue analysis of a structure, the spectrum of the loading subjected during its life is necessary. The loads are often validated by flight tests. The spectrum of the loading on the helicopter changes according to the mission it will act.

Each type of rotorcraft such as emergency medical services, transportation, search and rescue (SAR) and armed etc. has unique missions specified for it. The operations to be accomplished by the rotorcraft establish the maneuvers such as climb, take off, forward flight, turn, landing etc. and their duration. Altitude, speed, fuel, gross weight and the center of gravity of rotorcraft vary for each of these operations. Thus the usage spectrum is created by the combination of maneuvers and their percentage time throughout its operational lifetime [44].

The life of a helicopter component is represented as the flight hours. A flight hour is computed from the time of flight considered from engine start to engine stop. Hence a load spectrum used in the fatigue analysis corresponds to a number of flight hours. Flight load

spectrums are determined for the flight conditions and maneuver of the mission profile by combining usage spectrum and corresponding loads. The fatigue loading may be constant amplitude, constant mean, or a spectrum loading, i.e. variable amplitude and /or mean.

The cyclic loads can be defined with maximum and minimum values as well. A spectrum of the loading on the helicopter changes according to the mission it will act. It has to be representative of the expected mission profile of the rotorcraft.

Flight loads required for the fatigue evaluation is obtained from a comprehensive flight load survey. At the first stage of the analysis flight loads are often not available. An estimate of the load spectrum based on calculated flight loads can be used. The loads are often validated by flight tests. If possible, it is requested to conduct the flight program to measure strains by simulating usage spectrum. Stresses and loads are continuously recorded so the load spectrum is directly obtained for a particular structural element.

The outstanding loading for tail boom fuselage is generated by the tail rotor, which produces the thrust load required for yaw acceleration and for the compensation of main rotor torque. The thrust load is larger effect than the other loads such as tail plane lifting, tail rotor torque, gusts etc.[45].

The spectrum to be used for the forthcoming analysis is obtained from the study of Giglio [46]. In the paper a number of different spectrums are used to estimate the life of an helicopter component. In this study the spectrum for high loading level is applied to our model. That spectrum includes maneuver conditions, gust loads and maximum and minimum levels of the thrust load induced by tail rotor (see Table 31). It consists of eight (8) load cases. The model is subjected to 4000 times of this spectrum corresponding 10.000 flight hours.

Table 31 Load Spectrum

Flight Condition	Maximum Load (N)	Minimum Load (N)	Number of Cycles
Climb	20600	3900	1
Vertical Gust	18600	2900	1
Turn	21600	2900	1
Lateral Gust	16700	-1000	2
Descent	18600	2900	1
C.Descent	13700	2000	1
Spot Turn	18600	2900	3
Landing	13700	2000	1

4.3. Finite Element Modeling

4.3.1. General Procedure

An analysis of a structure by FEM includes three steps;

1) Preprocessing step covers the development of 2D or 3D models of the structure including assignment of the material properties and preparation of meshing.

2) The next step is solving the local and global system of equations and calculation strains, stresses etc.

3) In Post-processing step, visualization of the results is performed.

Finite element modeling allows engineers and researchers to solve complex problems easily. Commercial softwares provide good visualization for the assessment of the results. The results may vary according to modeling techniques of structural elements such as 1D, 2D or 3D, boundary conditions and the element size.

The Young's modulus of the materials used in finite element analysis (FEA) is given in Table 32. The detailed material properties of the aluminum are given in Appendix A.

Table 32 Modulus of elasticity of the materials used in FEA

Material	Young's Modulus (MPa)	Poisson's ratio
AL2024 T3	72395	0.33
AL7050 T7451	71000	0.33
45-cb (titanium alloy)	107000	0.33
P15-7 (corrosive resistant steel)	199000	0.33

4.3.2. Sub-modeling of the fuselage structure

The complex engineering systems are often not modeled in full detail in fact that the modeling and analysis time of a complex model may take so much time. Global–local modeling technique called as submodeling is extensively used in aerospace industry. In the submodeling method a global model is prepared ignoring the details not to affect the overall behavior of the system such as holes, joints and cut-outs etc. Contrarily a local model will have more details with fine meshing (smaller element size). The boundary conditions of the local model are extracted from the global model. The usage of global-local modeling technique will provide the ability to improve FE model to obtain more accurate results by refining the mesh where high field gradients exist.

A sub-modeling technique is implemented for a pressurized aircraft fuselage by three modeling levels in the study of Potyondy et al [47]. In order to determine the constraints of the local model more accurately, the boundary conditions (displacements and rotations) of the 2x2 bay stiffened panel model are extracted from the analysis of 6x6 bay stiffened panel (Figure 38).

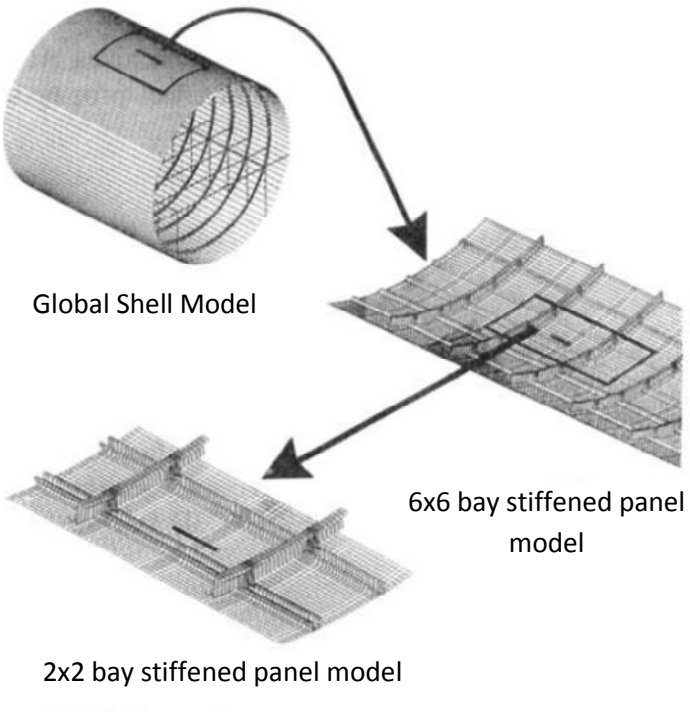

Figure 38 Hierarchical sub-modeling technique [47]

Another application of submodeling was adopted in the study of Giglio [46] Displacements in the global model occurring on the interface nodes applied to the finer meshed local model of the complex structure by linear interpolation method.

In this study, the global model of a helicopter tail boom was generated by using coarse elements, not including the details. In the model, skin panels are modeled by quadrilateral 2D shell elements with 4-node, CQUAD4. The main function of the stringers is to carry mainly axial loads. Stringers are therefore modeled as 1D beam elements (see Figure 39 and Figure 40). Stringers are modeled by CBAR elements representing the physical behavior of a beam. The functions of the frames are to carry both axial loads and bending moments. As for the frames, both the shell and 1D beam elements are used in the modeling. The fasteners, holes, contour etc. are ignored in modeling. To model the fasteners in a large global model is neither practical nor particularly useful. Load will concentrate on single fasteners whereas in reality load will be shared by other fasteners as well, especially under static loading. Horizontal stabilizer is not modeled at all because its effect on the analysis of tail boom is negligible.

Local model is constructed by very fine elements comparing to the element sizes of the global model. The rivets are modeled by the connector elements in MSC.Patran. A cut-out is added to the local model. Cut-outs in fuselage of a helicopter are inevitably opened to install antenna, sensors and maintenance covers etc. The element type of the panels in local model is the same as that of the global model but in scale-down sizes. Stringers are modeled by using 2D shell elements (see Figure 41).

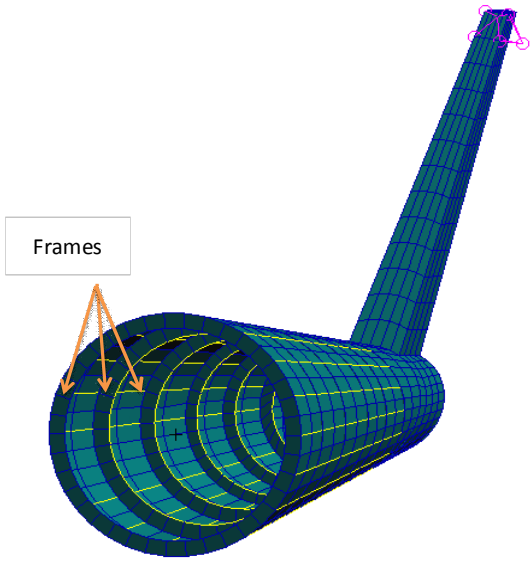

Figure 39 Global FE model

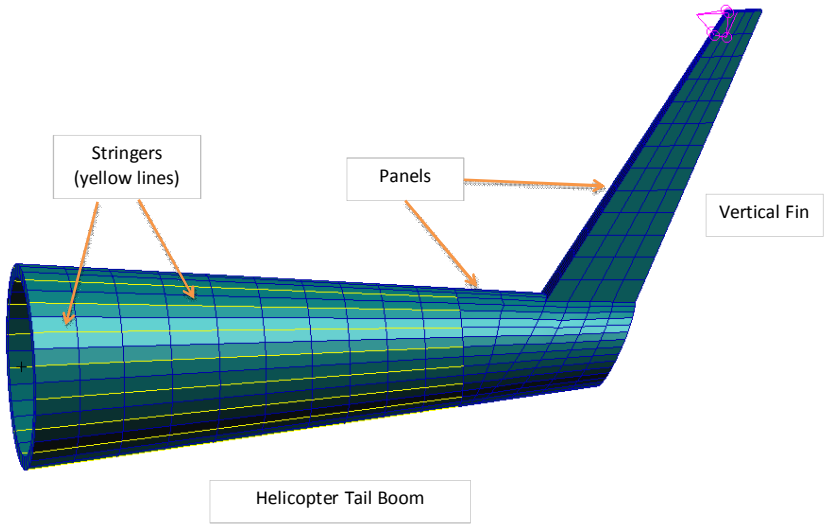

Figure 40 Main elements of the global model

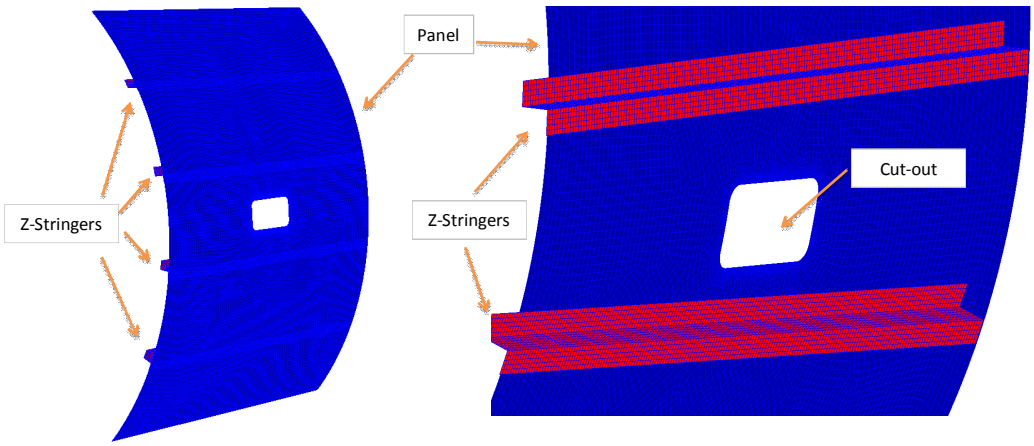

Figure 41 Local FE model

There are several sub-modeling techniques to provide smooth connection between global and local model. In one technique the global model is analyzed with its boundary conditions. Then the boundary conditions of a local model in which the geometric details are modeled in further details are extracted from the results of the global analysis. The boundary conditions (forces, displacements) at the nodes and elements of the local model with finer mesh are interpolated from the internal results at the nodes and elements of the global model. In this method, the global and the local model should be analyzed separately so it requires two steps.

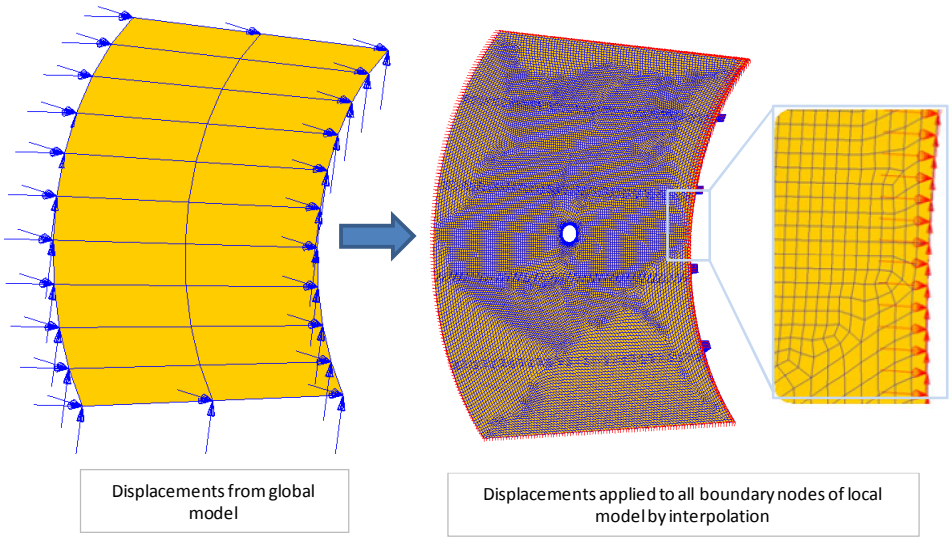

Figure 42 Boundary conditions of local model

Another method is to use multi-point constraint elements to link the nodes of the global model with coarse mesh and the nodes of the local model with fine mesh (see Figure 43). Hence a new model is constructed by attaching the local model to the global model. This new model can be solved by the global boundary conditions. The main advantage of this way is that the solution is obtained at one step. Its drawbacks are that the special link element is necessary to distribute the nodal forces or displacements of the global model to the local model and the analysis will take up more memory and time.

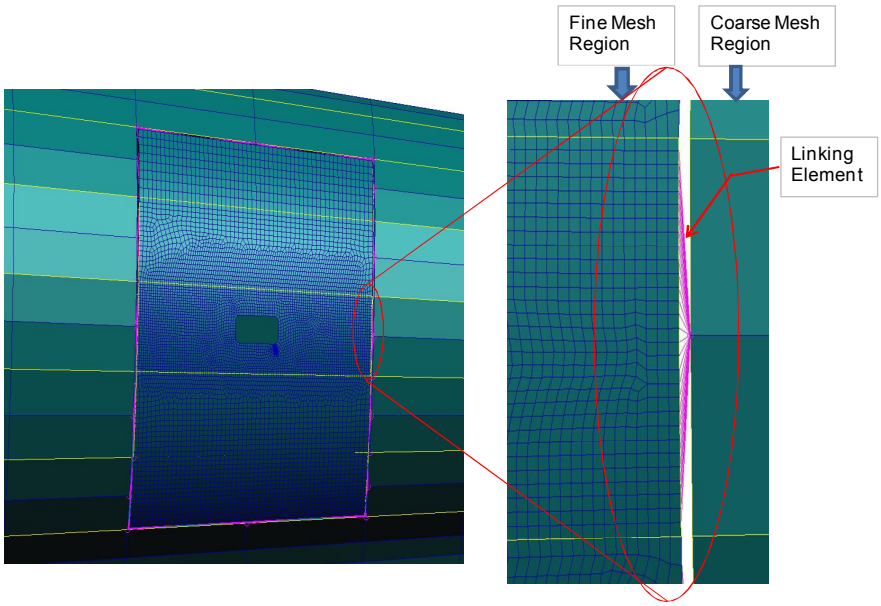

Figure 43 Connection of coarse mesh and fine mesh regions via linking element

RBE3, RBE2 and RSPLINE, multipoint constraint elements provided by MSC.Patran are used as a connection element. RBE3 defines relationship in which the motion at a reference grid point is the least square weighted average of the motions at other grid points (belonging to the sub-model). It is an interpolation element, which does not add extra stiffness to the model. RBE2 provides a convenient tool for rigidly connecting the same components of several grid points together. RSPLINE elements define multipoint constraints for the interpolation of displacements at grid points [48]. This element is useful in changing mesh size in finite element models. RSPLINE is not supported by MARC. Hence it is not examined in this study.

As the method of the connection element RBE3 and RBE2 is applied in the model, the deformation results are given in Figure 44 and Figure 45. The linking global and local model by connection elements can generate excessive displacements and forces at the linked boundary nodes and elements. The application of this method leads to that problem because RBE3 would not add stiffness and the nodes move freely out of plane direction. RBE2 element gives better result than RBE3.

The other method is that the solution of the global model is firstly obtained and then the displacement results of the relevant nodes are spreaded to the nodes of the local model by interpolation method. When the deformation result of the local model is compared with the

analyzed portion that is the counterpart of the local model in the global model, the almost same distribution of the displacement is obtained as seen in Figure 46 and Figure 47.

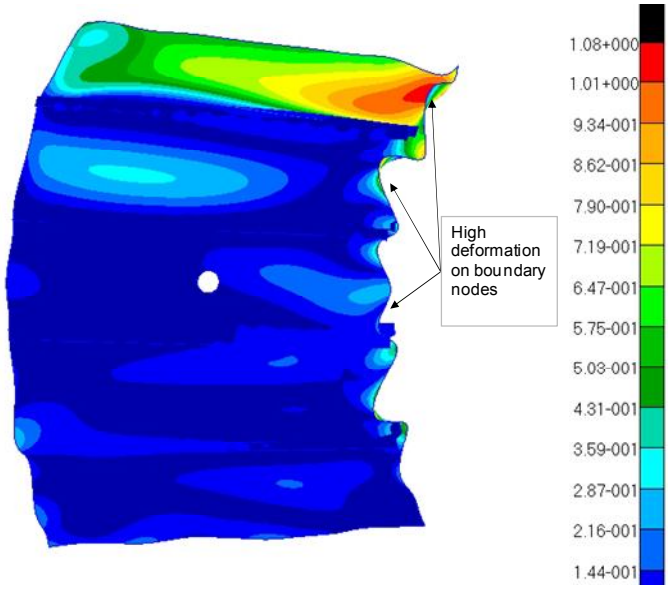

Figure 44 Deformation result of local model connected by RBE3 linking element

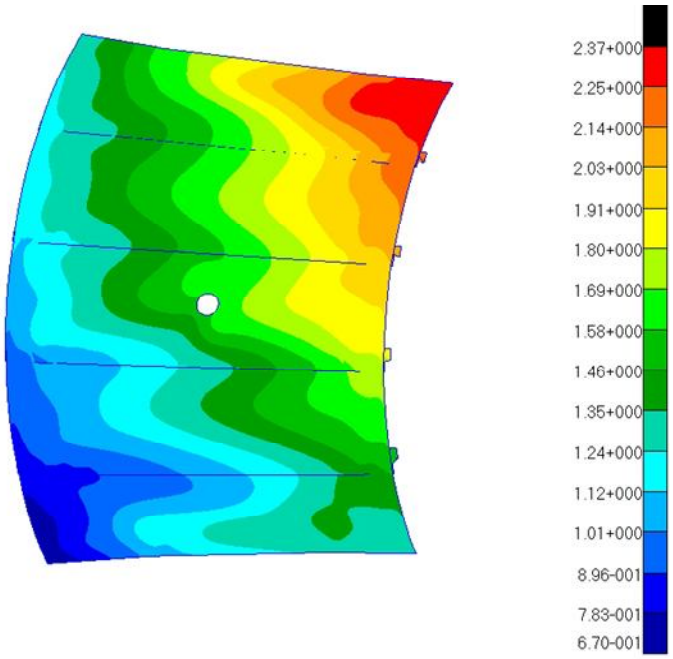

Figure 45 Deformation result of local model connected by RBE2 linking element

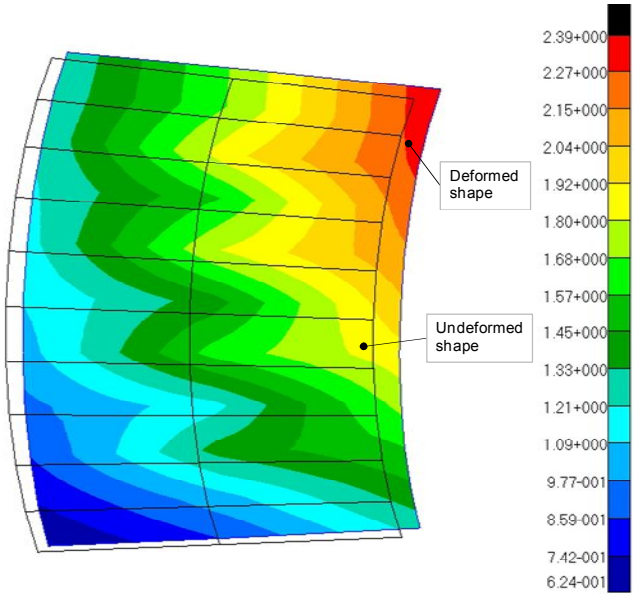

Figure 46 Deformation result of the portion of global model, which is the counterpart of the local model

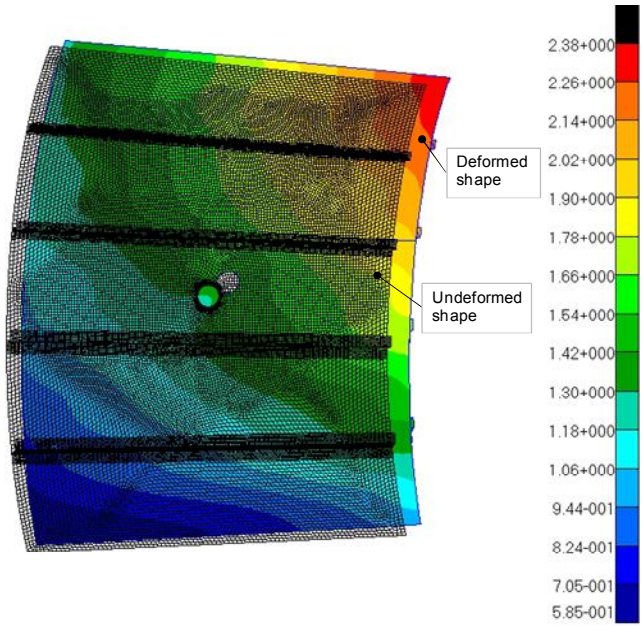

Figure 47 Deformation result of local model whose boundary conditions are displacements from global model

It is concluded that the method where global model is tied to local model by RBE2 element and the other method where the boundary conditions of local model are obtained from the analysis of global model are applicable as a sub-modeling technique in this study. In the latter method once the solution of global model is obtained, it is not necessarily required to run again the analysis with global model. It reduces the computation time fairly. Therefore two-step method is decided for sub-modeling.

4.3.3. Modeling of rivets

It is very common method to model fasteners as 1D bar element. Hence the appropriate cross sectional properties can be defined. Fasteners are occasionally modeled as rigid elements but in that case extra stiffness is introduced to the model. Another issue is the modeling of the holes, where fasteners are passing through and the connection between the holes and the fasteners.

MSC.Patran provides a special element, CFAST, for the fasteners. The remarkable side of this element is not mesh-dependent. Hence it does not require proper mesh on both connected side with grids at the location of the fastener. The properties of the fastener such as stiffness and the diameter are input to the program. Another input is the grids representing the location of the fastener. The program internally generates bushing elements having the stiffness values of the fasteners and create auxiliary grids on the connected parts. RBE3 elements are internally established to connect the grid points. By introducing RBE-3 and a number of grids, localized load transfer is eliminated at the point of connection. The illustration of the modeling for the fasteners is shown in detail in Figure 48. The fastener is linked to the particular nodes of the elements via RBE3.

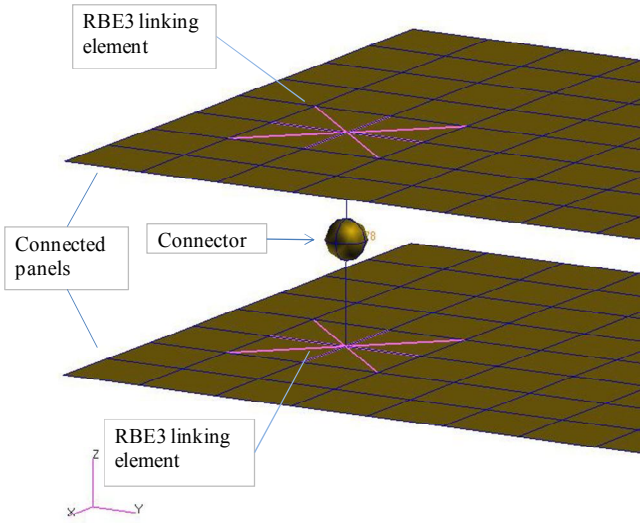

Figure 48 Finite element model of the fasteners

In literature several formulations are available to predict fastener flexibility [49],[50]. Regarding shear stiffness, the formula given by Swift [50] is:

$$K_{y,z} = \frac{5}{dE_3} + 0.8\left(\frac{1}{t_1E_1} + \frac{1}{t_2E_2}\right) \quad (24)$$

In this study Huth method is used, and rivet stiffness's are calculated as follows [49]:

Axial stiffness,

$$K_x = \frac{EA}{L} \tag{25}$$

Shear flexibility,

$$C = \left(\frac{t_1 + t_2}{2d}\right)^a \frac{b}{n}\left(\frac{1}{t_1 E_1} + \frac{1}{nt_2 E_2} + \frac{1}{nt_1 E_3} + \frac{1}{2nt_2 E_3}\right) \tag{26}$$

Shear Stiffness,

$$\mathrm{K_y}, \mathrm{K_z} = 1/\mathrm{C} \tag{27}$$

where E_3: modulus of elasticity of rivet material, E_1 and E_2: modulus of elasticity of the connected plates, d: sectional area of the rivet, t_1 and t_2: thicknesses of the connected plates, a: 2/3 for bolted joints and 2/5 for riveted joints, b: 3 for bolted joints and 2.2 for riveted joints, n=1 for single shear, and n=2 for double shear joints

4.4. Determination of Stress Intensity Factor

4.4.1. Determination of Probable Crack Locations

Indeed it is not possible to know the exact location of the crack initiation as the crack can start to grow due to manufacturing defects or material distortions etc. There is a variety of methods for the determination of probable crack location such as [44]:

- Performing a static analysis to determine the location with highest stress
- Conducting fatigue analysis to determine possible locations where the crack can initiate
- Surveying the results from the static tests to find out the highest deformed locations
- Assessing geometric details such as holes can generate fatigue damage by considering previous test and service experiences for similar components
- Examining the areas in an element, its failure causes the maximum stress in neighboring element
- Examining strains on the structure, which does not have damage, to find out the locations with high stress concentrations

The method judged as conservative and suitable for this study is to initiate the crack from maximum principal stress zone which is prone to fatigue damage. The crack growth rate will even be high due to high loading at that location.

Before starting fracture analysis, a static analysis is executed to extract the maximum principal stresses around the cut-out. The mesh at the edge of the cut-out is refined to find-out the accurate solution. Then the initial crack is placed on the edge where the maximum stress value is obtained. As shown in Figure 49, the critical areas in terms of maximum principal stresses are indicated in red circle A and B.

The crack initiation area is chosen as area-A. Initial crack is assumed to be present from the beginning of the helicopter life.

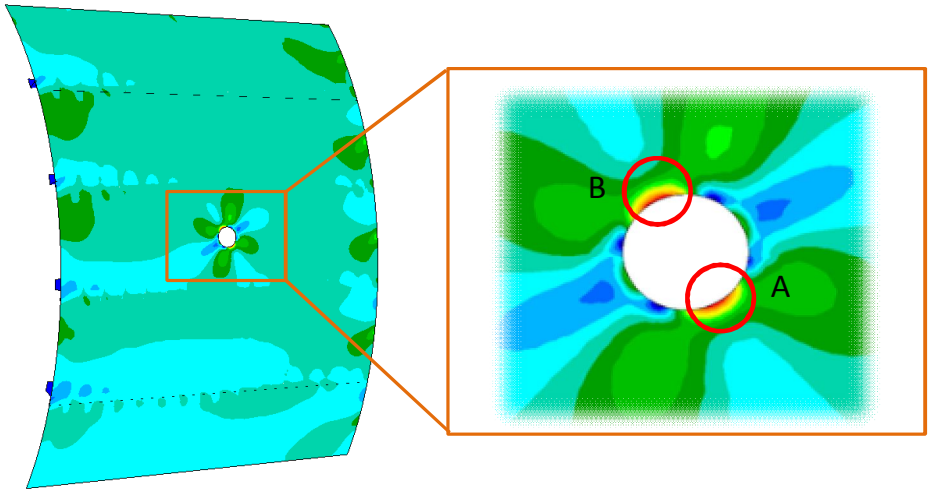

Figure 49 Highly stressed area of local model

The critical elements having higher maximum principal stresses than the others in the critical area are investigated in detail. Then the initial crack growth location is determined as shown in Figure 50.

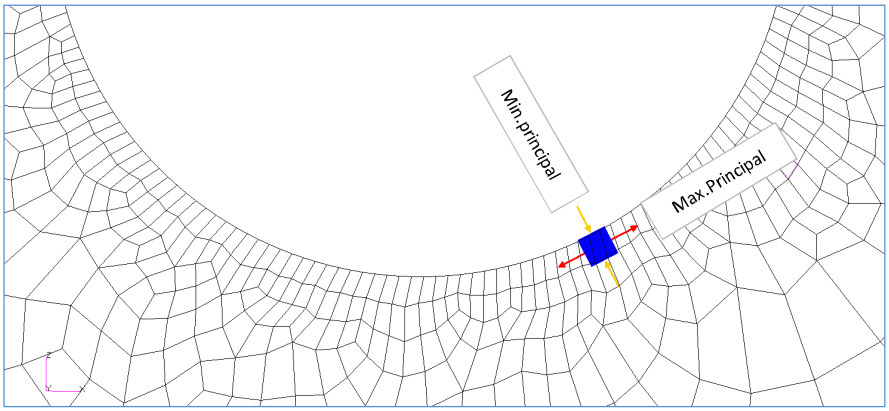

Figure 50 The most critical element in highly stressed region

4.4.2. The effect of structural parameters on stress intensity factor

In this section, the effect of the structural parameters and finite element modeling parameters on the stress intensity factor are investigated for the helicopter fuselage structure regarded as the stiffened panel. After determination of FEM parameters giving sufficiently accurate results, various structural configurations are analyzed. The location of initial crack obtained from the previous analysis is used for all fracture analyses in this section.

Firstly, by modifying FEM parameters as shown in Table 33 (the mesh size at the crack tip and the increment size) the effect of those parameters on the crack trajectory and stress intensity factor values and are investigated. This investigation allows deciding the satisfactory parameters. Different mesh sizes around the crack tip are analyzed while crack increment size is kept unchanged for FEM configuration1, configuration-2 and configuration-3. Crack growth is also simulated with different step sizes of $\triangle$a=15 mm and $\triangle$a=20 mm in configuration-4 and configuration-5 by keeping tip element size as 0.5 mm.

Table 33 FEM parameters to be modified

FEA Parameters	Element Type	Element Size at Crack Tip (mm)	Crack Increment Size (mm)
FEM Configuration-1 (BASE)	Quad4	0,5	10
FEM Configuration-2	Quad4	0,1	10
FEM Configuration-3	Quad4	1	10
FEM Configuration-4	Quad4	0.5	15
FEM Configuration-5	Quad4	0.5	20

The results of FEA for the different FEM parameters are presented in Table 34, Table 36 and Table 37. The crack length, energy release rates, stress intensity factors and crack extension angles are given for each analysis step in the tables. Additionally, deviation of mode-I stress intensity factor values from those of basic configuration (FEM configuration-1) are given in Table 35.

It is obvious from Table 34 that opening fracture mode (Mode-I) is very dominant when compared to sliding mode (mode-II). The largest value of stress intensity factor for mode-II (K_{II}) is obtained at the first step of analyses. As the crack extends, the mode-II values are getting very low according to mode-I values. The crack extension angle is getting diminished in parallel with decrease in mode-II values. The plots of stress intensity factor values for mode-I against crack length are illustrated in Figure 51 and Figure 52 for different tip mesh sizes and crack increment sizes respectively. Note that for different tip meshes the plots of stress intensity factor, K_I against the crack length are very similar to each other. Difference between mode-I values does not exceed %0.75 for tip mesh size 0.1 mm and 0.5 m and is not larger than %2 for tip mesh size 0.1 mm and 1 mm (see Table 35). Consequently tip mesh size of 0.5 mm is acceptable and used for the rest of the analyses.

Table 34 The analysis results for FEM Configuration-1 (Crack Incr.=10 mm, Tip mesh=0.5 mm)

FEM Configuration-1 (BASE)

Step	a (mm)	G_I (N/mm)	K_I (Mpa(m)$^{1/2}$)	G_{II} (N/mm)	K_{II} (Mpa(m)$^{1/2}$)	θ (degree)
1	10	3.2008	15.22	0.1224	2.98	20.7
2	20	4.4927	18.03	0.0001	0.09	0.6
3	30	5.6405	20.21	0.0001	0.09	0.5
4	40	6.6574	21.95	0.0001	0.09	0.5
5	50	7.6460	23.53	0.0019	0.37	1.8
6	60	8.0726	24.17	0.0018	0.36	1.7
7	70	7.2010	22.83	0.0019	0.37	1.9
8	80	6.5908	21.84	0.0326	1.54	8.0
9	90	6.7912	22.17	0.0106	0.87	4.5
10	100	6.8161	22.21	0.1006	2.70	13.5
11	110	7.1880	22.81	0.0120	0.93	4.7
12	120	7.5140	23.32	0.0003	0.15	0.7
13	130	7.6401	23.52	0.0083	0.77	3.8

Table 35 Difference between K_I values for various tip mesh sizes

Step	a (mm)	Config-1 (tip mesh=0.5 mm)	Config-2 (tip mesh=0.1 mm)		Config-3 (tip mesh=1 mm)	
		K_I (Mpa(m)$^{1/2}$)	K_I (Mpa(m)$^{1/2}$)	Diff.	K_I (Mpa(m)$^{1/2}$)	Diff.
1	10	15.22	15.23	-0.02%	14.99	1.51%
2	20	18.03	18.07	-0.19%	17.86	0.95%
3	30	20.21	20.30	-0.44%	19.93	1.39%
4	40	21.95	22.03	-0.36%	21.63	1.49%
5	50	23.53	23.56	-0.16%	23.16	1.55%
6	60	24.17	24.17	0.01%	23.85	1.35%
7	70	22.83	22.71	0.53%	20.67	0.97%
8	80	21.84	21.99	-0.69%	21.92	-0.37%
9	90	22.17	22.01	0.74%	22.04	0.60%
10	100	22.21	22.27	-0.25%	22.32	-0.47%
11	110	22.81	22.86	-0.23%	22.59	0.98%
12	120	23.32	23.16	0.70%	22.86	1.98%
13	130	23.52	23.52	-0.03%	23.22	1.25%

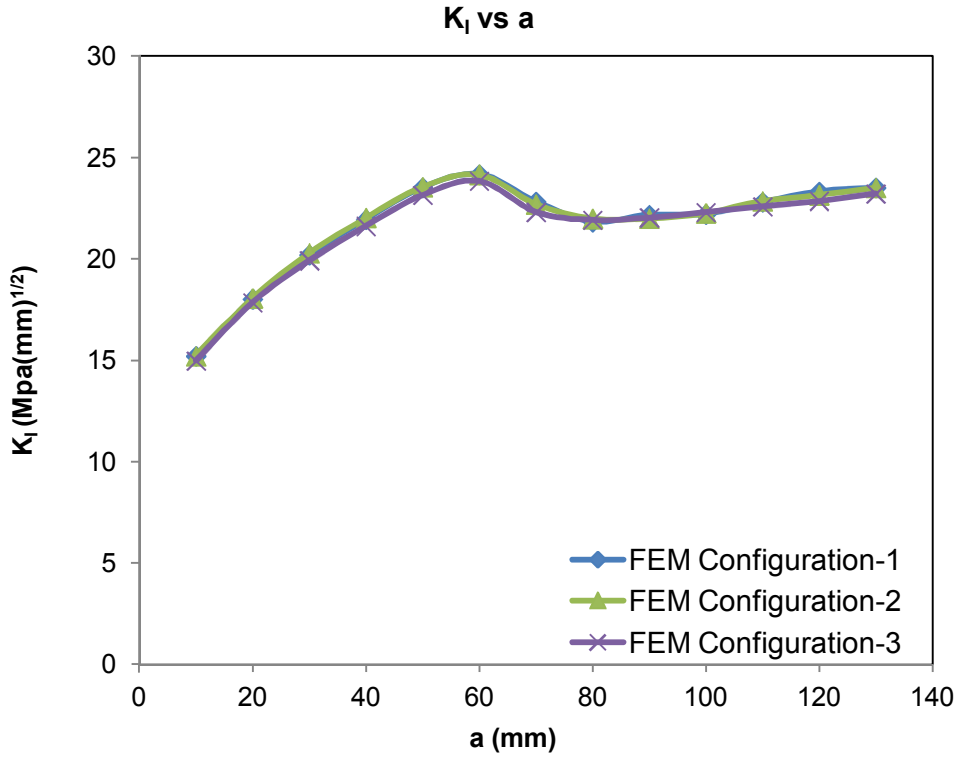

Figure 51 K_I vs crack length plots for different tip mesh sizes

Table 36 Fracture analysis results for FEM Configuration-4 (Crack Incr.=15 mm, Tip mesh=0.5 mm)

FEM Configuration-4

Step	a (mm)	G_I (N/mm)	K_I (Mpa(m)$^{1/2}$)	G_{II} (N/mm)	K_{II} (Mpa(m)$^{1/2}$)	θ (degree)
1	10	3.4448	15.79	0.2074	3.87	24.9
2	25	5.5692	20.08	0.0134	0.98	5.6
3	40	7.0880	22.65	0.0059	0.65	3.3
4	55	8.0980	24.21	0.0299	1.47	6.9
5	60	6.7835	22.16	0.0012	0.30	1.5
6	75	6.7496	22.11	0.0131	0.97	5.0
7	90	6.8090	22.20	0.1419	3.21	15.8
8	105	7.3616	23.09	0.0328	1.54	7.6
9	120	7.8580	23.85	0.0001	0.10	0.5

Table 37 Fracture analysis results for FEM Configuration-5 (Crack Incr.=20 mm, Tip mesh=0.5 mm)

FEM Configuration-5						
Step	**a (mm)**	**G_I (N/mm)**	**K_I (Mpa(m)$^{1/2}$)**	**G_{II} (N/mm)**	**K_{II} (Mpa(m)$^{1/2}$)**	**θ (degree)**
1	10	3.2008	15.22	0.1224	2.98	20.7
2	30	5.5558	20.06	0.0004	0.16	0.9
3	50	7.6081	23.47	0.0040	0.54	2.6
4	70	7.2409	22.90	0.0089	0.80	4.0
5	90	6.6004	21.86	0.0691	2.24	11.5
6	110	7.2366	22.89	0.0001	0.07	0.3
7	130	7.5609	23.40	0.0117	0.92	4.5

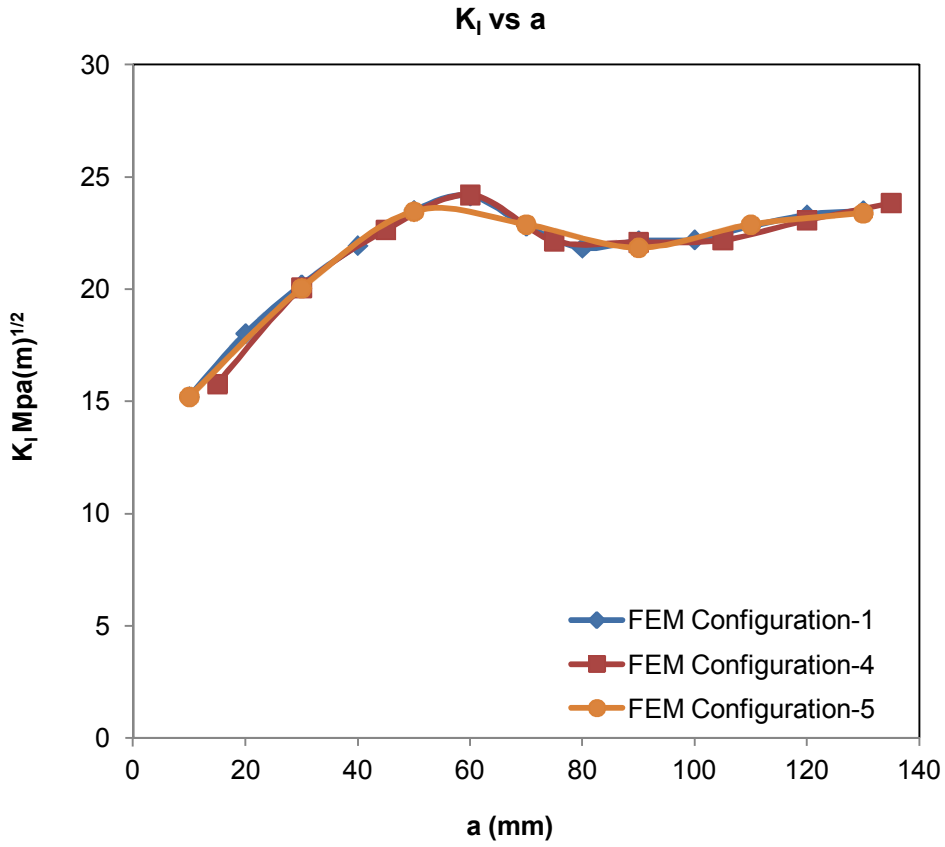

Figure 52 K_I vs crack length plots for different crack increment sizes

With regard to the amount of crack increment, mode-I stress intensity factor values along the crack path follow almost similar trend (see Figure 52). It is observed that the analysis with crack increment size of 20 mm does not exactly catch peak and lowest values when the crack passes through the stiffener. Finite element model with the crack path for crack

increment size of 10 mm (basic configuration) is shown in Figure 53. It is observed that the crack tip tends to grow towards x-direction of the coordinate system, which is shown in Figure 53. From Figure 54, it can be seen that the crack follow very similar paths for the analyses with crack increment sizes of 10 mm, 15 mm and 20 mm. There are some local variations in the crack path but the trend is generally consistent even for high increment sizes.

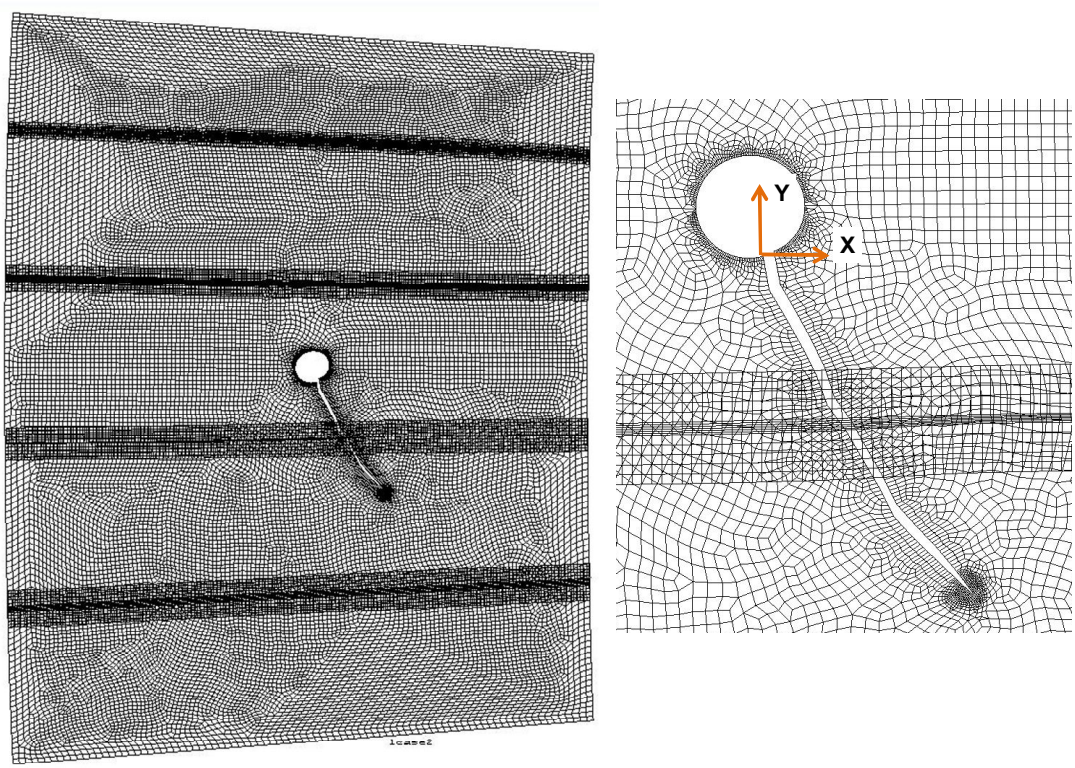

Figure 53 Crack path for basic configuration

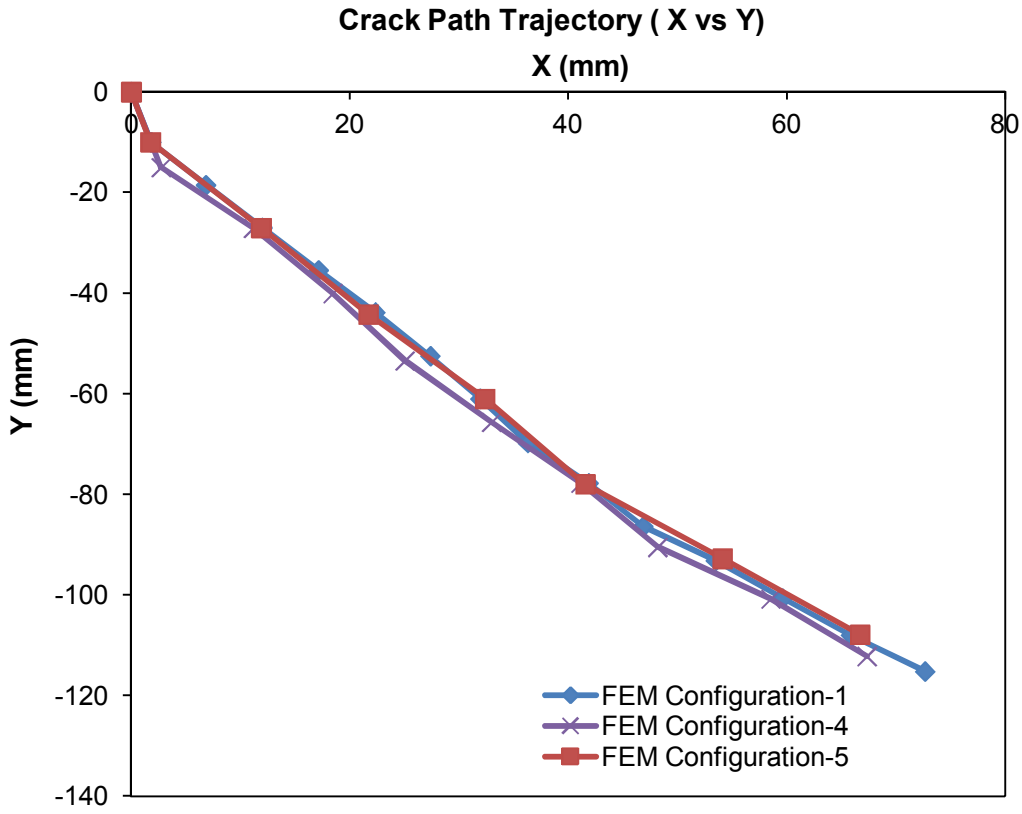

Figure 54 Crack path trajectories for different crack increment sizes

The configurations of geometric features are listed in Table 38. The basic FEM parameters given in the first row of Table 33 is used during the examination of geometric factors. Hence the crack increment length and the mesh size around tip are set as 10 mm and 0.5 mm respectively. The basic configuration of geometric features is determined as given in the first row of Table 38. Then one parameter varied from basic geometric configuration is examined at each time. Global analysis is repeated for some of the configurations, and the local boundary conditions of the basic configuration are not used. The modifications (the panel thickness, the cross section area of the stringer) applied into those configurations changes the global results so the boundary conditions of the local model are also influenced by these modifications.

Table 38 The geometric parameters to be modified

Geometric Parameters	Panel Thickness (mm)	Stiffener C.S. Area (mm^2)	Rivet Spacing (mm)	Rivet Material
Geometric Configuration-1 (BASE)	0,64	48	35	AL7050T3
Geometric Configuration-2 (no direction change)	0,64	48	35	AL7050T3
Geometric Configuration-3 (no stiffener)	0,64	48	35	AL7050T3
Geometric Configuration-4 (Broken Stiffener)	0,64	48	35	AL7050T3
Geometric Configuration-5 (Stiffener C.S Area)	0,64	96	35	AL7050T3
Geometric Configuration-6 (Stiffener C.S Area)	0,64	32	35	AL7050T3
Geometric Configuration-7 (Rivet Material)	0,64	48	35	45-cb (Titanium alloy)
Geometric Configuration-8 (Rivet Material)	0,64	48	35	P15-7 (Corrosive Resistant Steel)
Geometric Configuration-9 (Rivet Spacing)	0,64	48	20	AL7050T3
Geometric Configuration-10 (Rivet Spacing)	0,64	48	54	AL7050T3
Geometric Configuration-11 (Panel Thickness)	0,81	48	35	AL7050T3

Firstly the comparison of the crack propagation analysis (configuration-1) taking into account change in extension angles with the analysis (configuration-2), where the crack grows straight ahead is performed. It provides estimation on the error when the alteration in crack angle is not considered. The crack path simulations for both analyses are given in Figure 55. Table 39 and Table 40 give the simulation results for both conditions. At the beginning of the analyses SIF values are the same for both cases. When the crack grows, increasing in mode-I SIF for configuration-2 is not as much as that for configuration-1.The relative

difference between configuration-1 and configuration-2 reaches up to 20 %. Regarding mode-II SIFs, as crack propagates, K_{II} for configuration-1 decreases, whereas increasing trend is seen for configuration-2. The ratio of mode II stress intensity factor to mode I stress intensity factors (K_{II}/K_I) is always small when the simulation allows change of crack orientation [43].

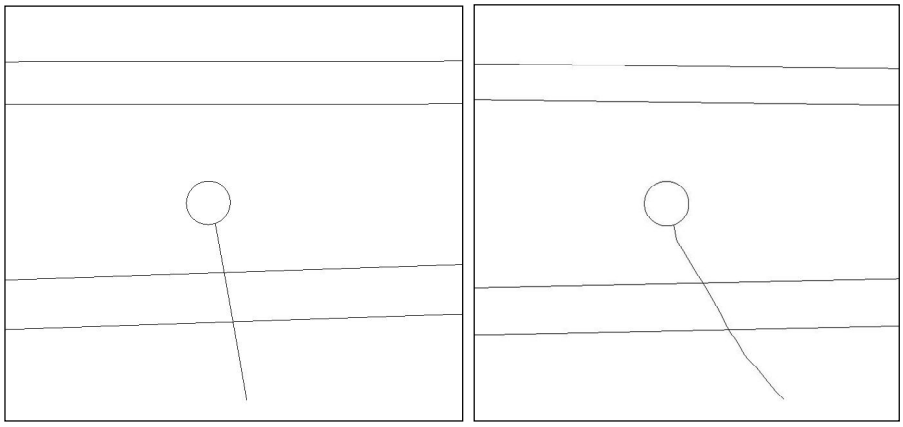

Figure 55 Crack paths for crack direction unchanged and changed

Table 39 Fracture analysis results for geometric congfiguration-1 (basic configuration)

Step	a (mm)	G_I (N/mm)	K_I (Mpa(m)$^{1/2}$)	G_{II} (N/mm)	K_{II} (Mpa(m)$^{1/2}$)	θ (degree)
1	10	3.2008	15.22	0.1224	2.98	20.7
2	20	4.4927	18.03	0.0001	0.09	0.6
3	30	5.6405	20.21	0.0001	0.09	0.5
4	40	6.6574	21.95	0.0001	0.09	0.5
5	50	7.6460	23.53	0.0019	0.37	1.8
6	60	8.0726	24.17	0.0018	0.36	1.7
7	70	7.2010	22.83	0.0019	0.37	1.9
8	80	6.5908	21.84	0.0326	1.54	8.0
9	90	6.7912	22.17	0.0106	0.87	4.5
10	100	6.8161	22.21	0.1006	2.70	13.5
11	110	7.1880	22.81	0.0120	0.93	4.7
12	120	7.5140	23.32	0.0003	0.15	0.7
13	130	7.6401	23.52	0.0083	0.77	3.8

Table 40 Fracture analysis results for geometric congfiguration-2 (crack direction is unchanged)

Geometric Configuration-2

Step	a (mm)	G_I (N/mm)	K_I $(Mpa(m)^{1/2})$	G_{II} (N/mm)	K_{II} $(Mpa(m)^{1/2})$
1	10	3.2008	15.22	0.1224	2.98
2	20	3.8815	16.76	0.2853	4.55
3	30	4.7218	18.49	0.3935	5.34
4	40	5.5348	20.02	0.4551	5.74
5	50	6.1998	21.19	0.3972	5.36
6	60	6.7771	22.15	0.3383	4.95
7	70	6.3446	21.43	0.4674	5.82
8	80	5.8592	20.60	0.6644	6.94
9	90	5.6386	20.20	0.9054	8.10
10	100	5.5479	20.04	1.1536	9.14
11	110	5.6590	20.24	1.2461	9.50
12	120	5.8314	20.55	1.3453	9.87
13	130	6.1909	21.17	1.2308	9.44

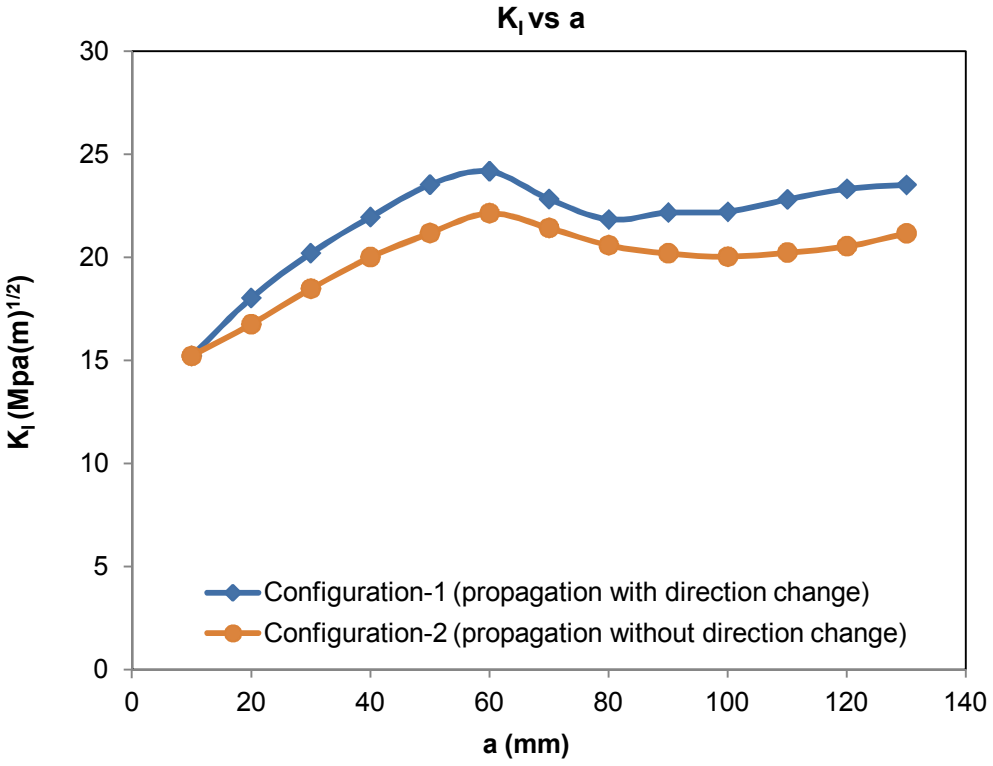

Figure 56 Comparison among mode-I SIF values for configuration-1 and configuration-2

To investigate the possible effects of lack of the stiffener on the stress intensity factor, the simulation is performed for configuration-3 (without stiffener).In configuration-3 the closest stringer to the crack tip is removed from the finite element model (see Figure 57). As for configuraton-4 (broken stiffener), the relevant elements of the stiffener are disconnected from the nodes so that the stiffener is separated into two pieces. The results are given in Table 41 and Table 42. Figure 59 demonstrates the variations of K_I values with the crack length for the configurations. The effect of the existence of the stiffener is clearly observed. The analysis with stiffener shows that when the crack tip passes through the stiffener, Kı values decreases, and then it starts to increase. Without stiffener there is no structure to prevent the opening of the crack, so Kı values increase relatively considerable amount when compared to configuration-1 (with stiffener). The most critical case for the stiffened panels is the tip of the crack under the broken stiffener because the broken stiffener forces the crack to propagate [51]. It considerably reduces the fatigue life. Finite element model including crack trajectory for the broken stiffener case is shown in Figure 58.

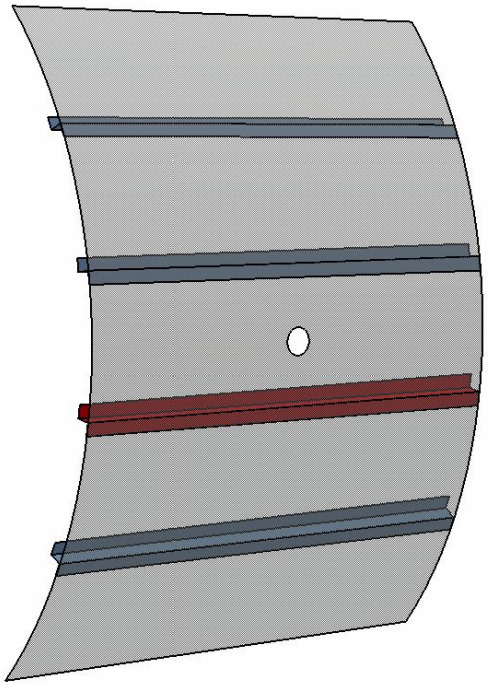

Figure 57 The stiffener with red color removed for configuration 3

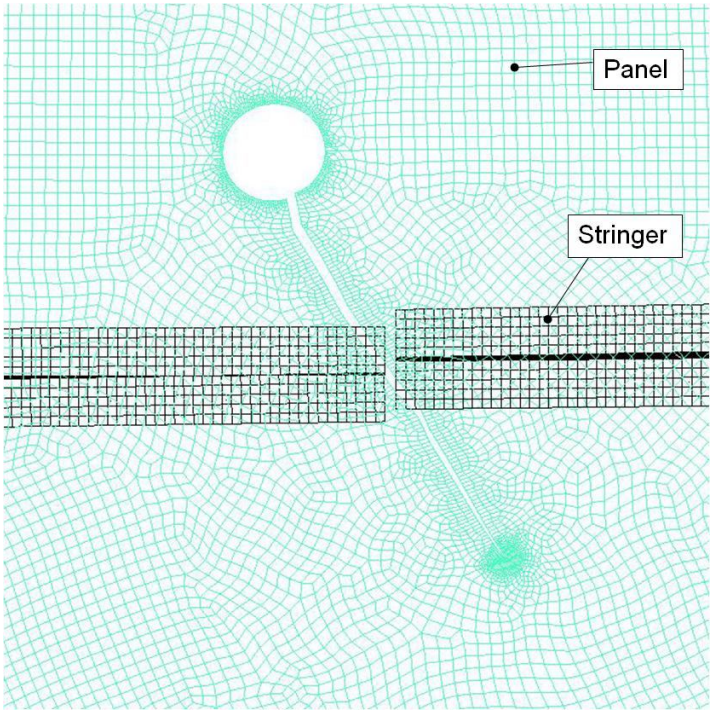

Figure 58 Crack growth trajectory for the broken stiffener case

Table 41 Fracture analysis results for geometric congfiguration-3 (without stiffener)

Geometric Configuration-3

Step	a (mm)	G_I (N/mm)	K_I (Mpa(m)$^{1/2}$)	G_{II} (N/mm)	K_{II} (Mpa(m)$^{1/2}$)	θ (degree)
1	10	3.3836	15.65	0.1381	3.16	21.3
2	20	4.9964	19.02	0.0011	0.28	1.7
3	30	6.4327	21.58	0.0014	0.31	1.7
4	40	7.9892	24.05	0.0012	0.29	1.4
5	50	9.3623	26.03	0.0147	1.03	4.5
6	60	10.5630	27.65	0.0002	0.12	0.5
7	70	11.3930	28.72	0.0021	0.39	1.5
8	80	11.8740	29.32	0.0068	0.70	2.7
9	90	12.0850	29.58	0.0023	0.41	1.6
10	100	11.9850	29.46	0.0099	0.85	3.3
11	110	11.7110	29.12	0.0041	0.54	2.1
12	120	11.2200	28.50	0.0275	1.41	5.6
13	130	10.7910	27.95	0.0006	0.20	0.8

Table 42 Fracture analysis results for geometric congfiguration-4 (broken stiffener)

Geometric Configuration-4

Step	a (mm)	G_I (N/mm)	K_I (Mpa(m)$^{1/2}$)	G_{II} (N/mm)	K_{II} (Mpa(m)$^{1/2}$)	θ (degree)
1	10	3.7848	16.55	0.1636	3.44	21.8
2	20	5.4529	19.87	0.0007	0.22	1.3
3	30	6.8504	22.27	0.0036	0.51	2.6
4	40	8.0748	24.18	0.0334	1.55	7.3
5	50	9.8400	26.69	0.0000	0.03	0.1
6	60	11.9350	29.39	0.0004	0.17	0.6
7	70	13.0810	30.77	0.0500	1.90	7.0
8	80	12.5290	30.12	0.2929	4.60	16.7
9	90	12.1090	29.61	0.0338	1.56	6.0
10	100	11.1980	28.47	0.0015	0.33	1.3
11	110	10.7080	27.84	0.0003	0.16	0.6
12	120	10.5310	27.61	0.0007	0.23	0.9
13	130	10.4440	27.50	0.0101	0.85	3.6

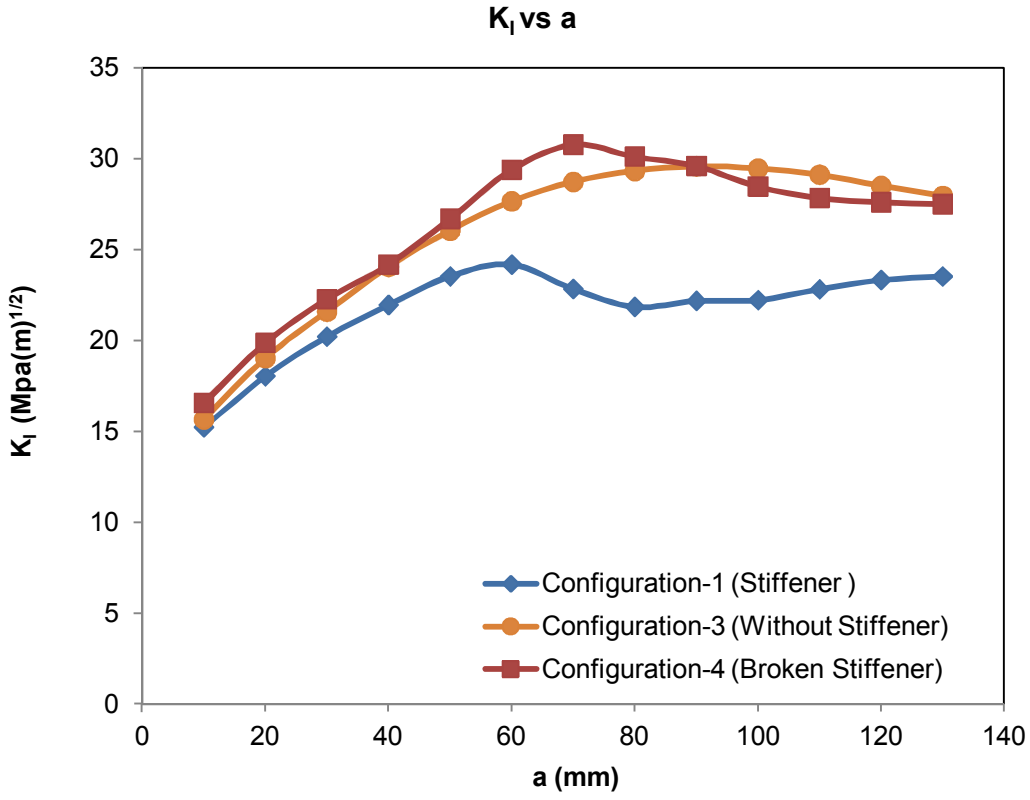

Figure 59 The comparison of K_I values among configuration-1, configuration-3 and configuration-4

Another investigation is performed for the effect of the stiffener size. The stiffener cross section area, which is 48 mm^2 for configuration-1 is modified to 96 mm^2 and 32 mm^2 for configuration-5 and configuration-6 respectively. From Figure 60, it can be deduced that stress intensity factor is considerably affected by the size of the stringer, which is proportional to stiffening effect. With the increase in the size of the stringer, the stress intensity factor tends to decrease and vice versa. From Table 43, it is seen that in case of 50 % increase in cross section area of the stiffener, K_I tends to decrease about 20 % with respect to the basic configuration. On the other hand, by decreasing the size of the stringer about 33 %, stress intensity factor increases about 10 % for the structure investigated here.

Table 43 Fracture analysis results for geometric congfiguration-5 (stiffener cross section area is 96 mm^2)

Geometric Configuration-5

Step	a (mm)	G_I (N/mm)	K_I $(Mpa(m)^{1/2})$	G_{II} (N/mm)	K_{II} $(Mpa(m)^{1/2})$	θ (degree)
1	10	1.8991	11.73	0.1547	3.35	28.0
2	20	2.9738	14.67	0.0001	0.07	0.6
3	30	3.7292	16.43	0.0000	0.01	0.1
4	40	4.3717	17.79	0.0003	0.13	0.9
5	50	4.9069	18.85	0.0002	0.12	0.7
6	60	4.9472	18.92	0.0047	0.58	3.5
7	70	4.8425	18.72	0.0026	0.43	2.7
8	80	4.6966	18.44	0.0003	0.13	0.8
9	90	4.5459	18.14	0.0112	0.90	5.7
10	100	4.5095	18.07	0.0006	0.20	1.3
11	110	4.5919	18.23	0.0037	0.52	3.3
12	120	4.8575	18.75	0.0004	0.16	1.0
13	130	5.1317	19.27	0.0009	0.25	1.5

Table 44 Fracture analysis results for geometric congfiguration-6 (stiffener cross section area is 32 mm^2)

Geometric Configuration-6

Step	a (mm)	G_I (N/mm)	K_I (Mpa(m)$^{1/2}$)	G_{II} (N/mm)	K_{II} (Mpa(m)$^{1/2}$)	θ (degree)
1	10	3.7021	16.37	0.1075	2.79	18.3
2	20	5.1543	19.32	0.0001	0.06	0.4
3	30	6.4621	21.63	0.0007	0.23	1.2
4	40	7.7656	23.71	0.0002	0.12	0.6
5	50	8.9129	25.40	0.0012	0.30	1.3
6	60	9.5465	26.29	0.0004	0.16	0.7
7	70	8.6388	25.01	0.0000	0.04	0.2
8	80	8.1147	24.24	0.0045	0.57	2.7
9	90	8.0741	24.18	0.0199	1.20	5.7
10	100	8.0860	24.19	0.1570	3.37	15.3
11	110	8.7805	25.21	0.0070	0.71	3.2
12	120	8.9238	25.42	0.0004	0.16	0.7
13	130	9.0988	25.67	0.0019	0.37	1.7

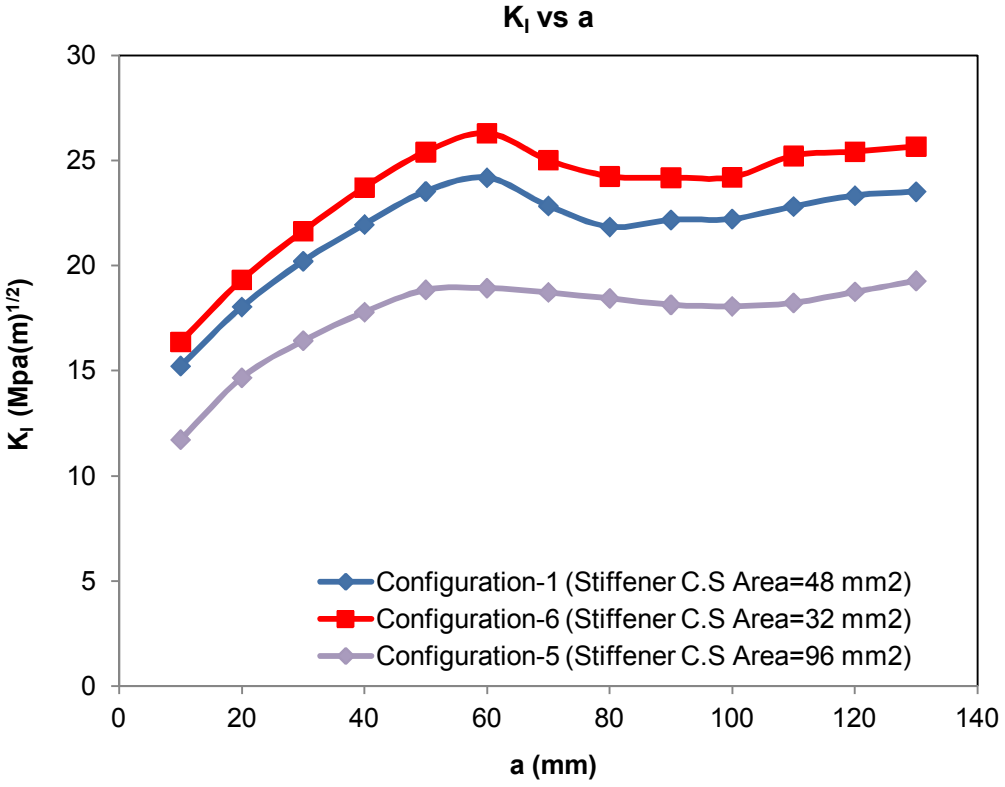

Figure 60 Comparision of different cross section areas of the stiffener

The analysis results for the different rivet pitch cases are presented in Table 45 and Table 46. Altering rivet pitch from 36 mm to 20 mm causes decrease in SIF, which is 9 % lower at most. On the other hand, increasing rivet pitch to 54 mm results in higher SIF values according to the basic configuration. The comparison of the stress intensity factor mode-I versus the crack length plots, which are computed for different rivet spacing cases, is illustrated in Figure 61. The effect of the rivet spacing is seen more effective as the crack passes through the stringer. It is clearly observed that the effect of the stiffener on stress intensity factor diminishes with the increase in rivet spacing.

Table 45 Fracture analysis results for congfiguration-9 (rivet spacing is 20 mm)

Geometric Configuration-9

Step	a (mm)	G_I (N/mm)	K_I (Mpa(m)$^{1/2}$)	G_{II} (N/mm)	K_{II} (Mpa(m)$^{1/2}$)	θ (degree)
1	10	3.1954	15.21	0.1168	2.91	20.3
2	20	4.4900	18.03	0.0001	0.08	0.5
3	30	5.5770	20.09	0.0002	0.11	0.7
4	40	6.5197	21.73	0.0005	0.18	1.0
5	50	7.1679	22.78	0.0020	0.38	1.9
6	60	7.5990	23.45	0.0100	0.85	4.1
7	70	6.5178	21.72	0.0378	1.65	8.6
8	80	5.8885	20.65	0.0147	1.03	5.7
9	90	5.7033	20.32	0.0007	0.23	1.3
10	100	5.6832	20.28	0.0033	0.49	2.7
11	110	5.9646	20.78	0.0097	0.84	4.6
12	120	6.3283	21.40	0.0002	0.13	0.7
13	130	6.8235	22.23	0.0021	0.39	2.0

Table 46 Fracture analysis results for congfiguration-10 (rivet spacing is 54 mm)

Geometric Configuration-10

Step	a (mm)	G_I (N/mm)	K_I (Mpa(m)$^{1/2}$)	G_{II} (N/mm)	K_{II} (Mpa(m)$^{1/2}$)	θ (degree)
1	10	3.2231	15.28	0.1234	2.99	20.7
2	20	4.5859	18.22	0.0000	0.03	0.2
3	30	5.9007	20.67	0.0009	0.26	1.4
4	40	7.0987	22.67	0.0110	0.89	4.5
5	50	7.9117	23.93	0.0383	1.67	7.9
6	60	7.9941	24.06	0.0117	0.92	4.4
7	70	7.7000	23.61	0.0000	0.03	0.1
8	80	7.7397	23.67	0.0056	0.64	3.1
9	90	7.7086	23.62	0.1307	3.08	14.4
10	100	8.4648	24.75	0.0004	0.17	0.8
11	110	8.5319	24.85	0.0001	0.09	0.4
12	120	8.5981	24.95	0.0022	0.40	1.8
13	130	8.5606	24.89	0.0256	1.36	6.2

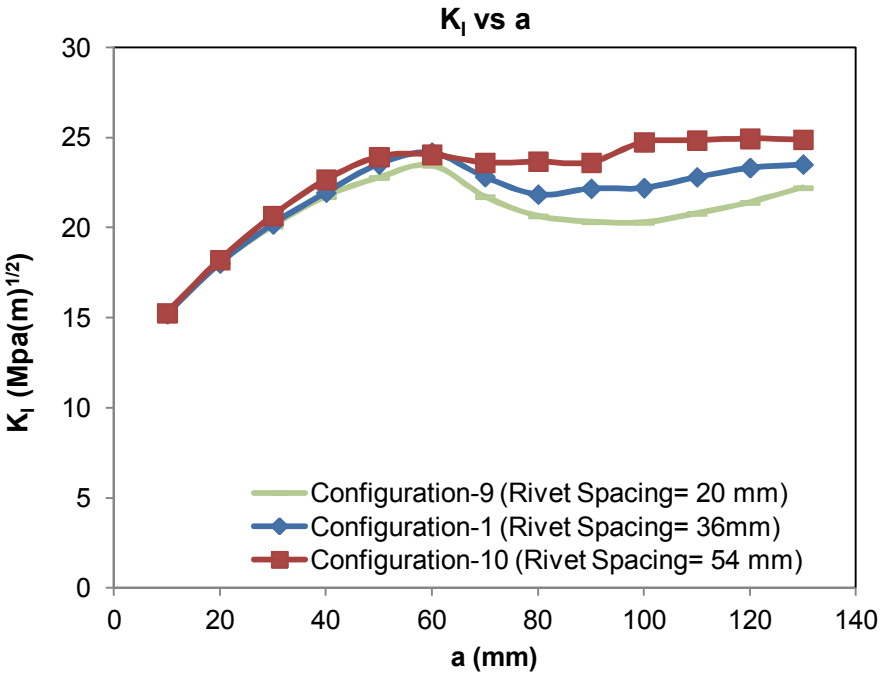

Figure 61 Comparision of different rivet spacing values

Regarding to the effect of rivet material on stress intensity factor, the impact of using more rigid fasteners on SIF is not high. The analysis results are given in Table 47 and Table 48. Figure 62 compares K_I values for the aluminum, titanium and steel rivet cases. The SIFs for titanium and steel rivet cases are slightly lower than the basic configuration, where aluminum rivet is used.

Table 47 The results for geometric congfiguration-7 (titanium 45c-b)

Step	a (mm)	G_I (N/mm)	K_I (Mpa(m)$^{1/2}$)	G_{II} (N/mm)	K_{II} (Mpa(m)$^{1/2}$)	θ (degree)
1	10	3.2113	15.25	0.1223	2.98	20.7
2	20	4.5526	18.15	0.0004	0.16	1.0
3	30	5.6265	20.18	0.0027	0.44	2.5
4	40	6.6512	21.94	0.0234	1.30	6.7
5	50	7.3566	23.08	0.1453	3.24	15.4
6	60	8.1566	24.30	0.0184	1.15	5.4
7	70	7.1565	22.76	0.0001	0.08	0.4
8	80	6.4513	21.61	0.0076	0.74	3.9
9	90	6.5857	21.84	0.1036	2.74	13.9
10	100	7.0125	22.53	0.0005	0.19	1.0
11	110	7.1240	22.71	0.0050	0.60	3.0
12	120	7.3356	23.04	0.0011	0.28	-1.4
13	130	7.6540	23.54	0.0023	0.41	-2.0

Table 48 The results for congfiguration-8 (corrosive resistant steel)

Geometric Configuration-8

Step	a (mm)	G_I (N/mm)	K_I (Mpa(m)$^{1/2}$)	G_{II} (N/mm)	K_{II} (Mpa(m)$^{1/2}$)	θ (degree)
1	10	3.1992	15.22	0.1223	2.98	20.7
2	20	4.4933	18.04	0.0004	0.16	1.0
3	30	5.5769	20.09	0.0027	0.44	2.5
4	40	6.5880	21.84	0.0234	1.30	6.8
5	50	7.2513	22.91	0.1453	3.24	15.5
6	60	8.0698	24.17	0.0184	1.15	5.4
7	70	7.0200	22.54	0.0001	0.08	0.4
8	80	6.3791	21.49	0.0076	0.74	3.9
9	90	6.2168	21.21	0.1036	2.74	14.3
10	100	6.8423	22.26	0.0005	0.19	1.0
11	110	6.9600	22.45	0.0050	0.60	3.1
12	120	7.1957	22.82	0.0011	0.28	1.4
13	130	7.4792	23.27	0.0023	0.41	2.0

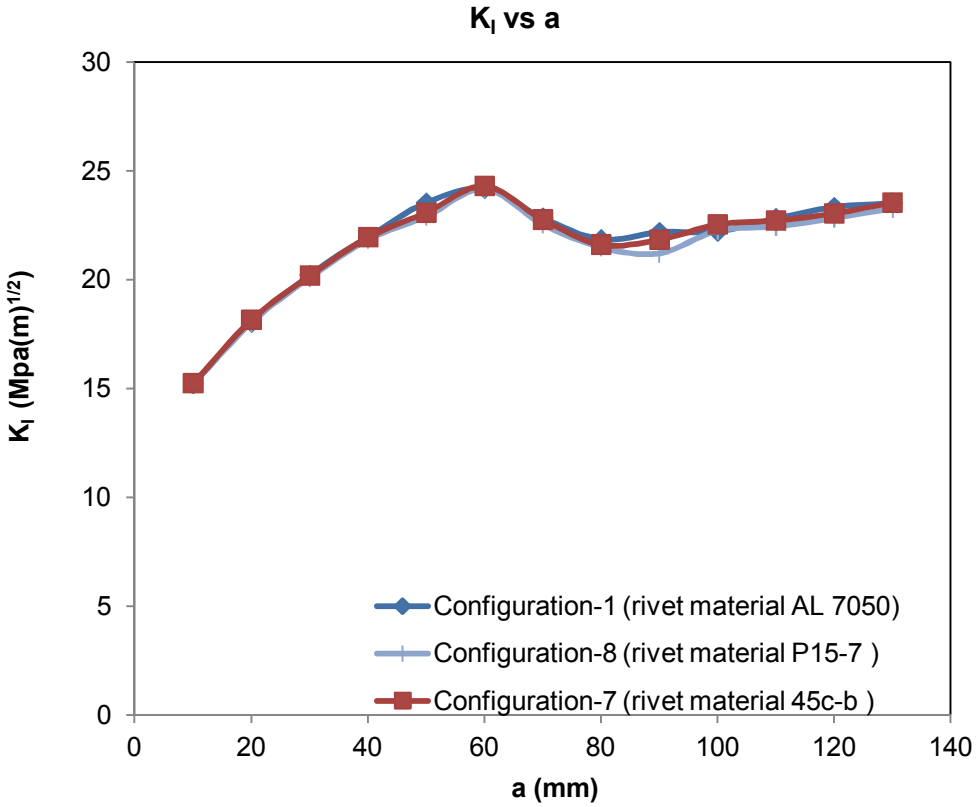

Figure 62 Comparision of different rivet materials

The thickness of the panel is increased from 0.64 mm to nearest upper standard value of 0.81 mm in configuration 11. The analysis result for the thrust load of 11000 N is given Table 49. Figure 63 shows the impact of using thicker panel on SIF. Due to the linear relationship between the thickness and stress values, thicker panel leads to lower stress intensity factor values as expected. With increase in panel thickness, stiffness ratio between the panel and the stringer is getting diminished so that the effect of the stiffener is reduced. The reduction in SIF due to the effect of the stiffener for the thicker plate case is not as much as that for thinner plate.

Table 49 The results for congfiguration-11 (panel thickness is 0.81 mm)

Step	a (mm)	G_I (N/mm)	K_I $(Mpa(m)^{1/2})$	G_{II} (N/mm)	K_{II} $(Mpa(m)^{1/2})$	θ (degree)
1	10	2.2087	12.65	0.0640	2.15	18.3
2	20	2.9653	14.65	0.0000	0.05	0.4
3	30	3.7062	16.38	0.0001	0.07	0.5
4	40	4.4445	17.94	0.0012	0.30	1.9
5	50	5.1559	19.32	0.0001	0.09	0.5
6	60	5.6055	20.14	0.0001	0.07	0.4
7	70	5.1142	19.24	0.0001	0.09	0.5
8	80	4.8977	18.83	0.0037	0.52	3.1
9	90	4.9956	19.02	0.0076	0.74	4.4
10	100	5.1872	19.38	0.0007	0.22	1.3
11	110	5.2433	19.48	0.0001	0.08	0.5
12	120	5.4974	19.95	0.0001	0.10	0.6
13	130	5.6556	20.23	0.0013	0.31	1.7

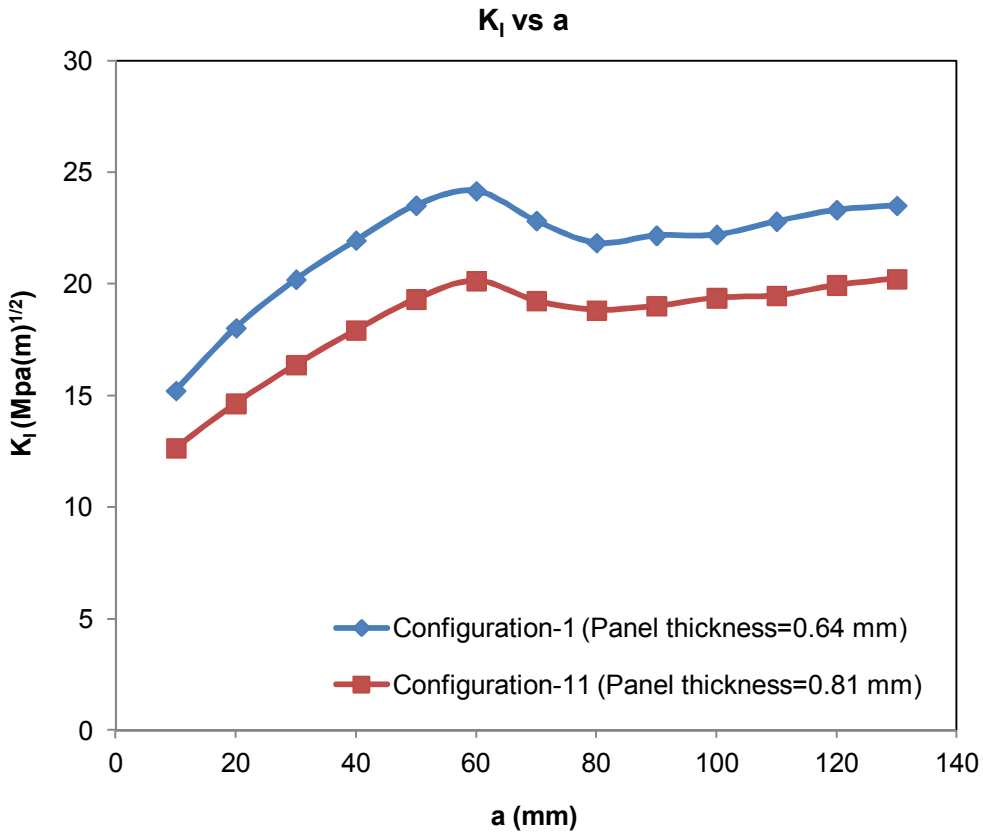

Figure 63 Comparison of different panel thicknesses

4.5. FATIGUE CRACK GROWTH ANALYSIS

In this section life assessment of the stiffened panel is achieved for the several configurations examined in previous section. The analytical solutions of the stress intensity factor for the correct combination of the crack shape, boundary conditions and loading does not exist for every case. Hence the usage of the finite element model is inevitable. Variation of stress intensity factors with the crack length that are obtained under unit loading condition in previous chapter is used for the life calculation.

The stress is proportional to the loading because the linear analysis is performed to compute the stress intensity factor. In order to obtain very accurate solution of the stress intensity factor, after even very little crack growth, the FEM analysis must be repeated for each cycle. Note that it is very inefficient and hard for the spectrum with hundred cycles because the analysis should be performed hundred times. Instead the stress intensity factors are linearly interpolated from those computed at each discrete step by FEM. Hence the stress intensity factors for maximum and minimum loads in spectrum are determined by interpolation from the stress intensity factors at appropriate crack length from the unit loading. The initial crack is assumed as through crack and the propagation will continue as through crack.

The method for the fatigue life estimation is illustrated in Figure 64. The fatigue crack growth life calculation is carried out by a code developed in VB Macro in Excel according to that method. For each load cycle the procedure is repeated. Fracture failure criteria is defined that the crack length has reached sufficient size so that the stress intensity at the crack tip

for maximum load (K_{max}) expected in service has reached plain strain fracture toughness (K_{IC}) or plain stress fracture toughness (K_C). Hence K_{max} values are checked at each cycle. The crack length against number of cycles is obtained at the end of the whole load spectrum.

In addition to stress intensity factor, to complete the life calculation the data of da/dN vs ΔK is necessary. It is obtained from experimental work. The experimental data is modeled by several propagation laws. Crack growth models are used for the assessment of the fatigue life of the structures subjected to cyclic loading. The models are constructed by fitting crack growth data from fatigue experiments. They give the relation describing the crack growth rate da/dN in terms of the stress and the crack length. This relation can be expressed in terms of stress intensity factor, K. Fatigue crack propagation models for mode-I and mixed mode combining mode-I and mode-II are reviewed in the forthcoming sections of the study.

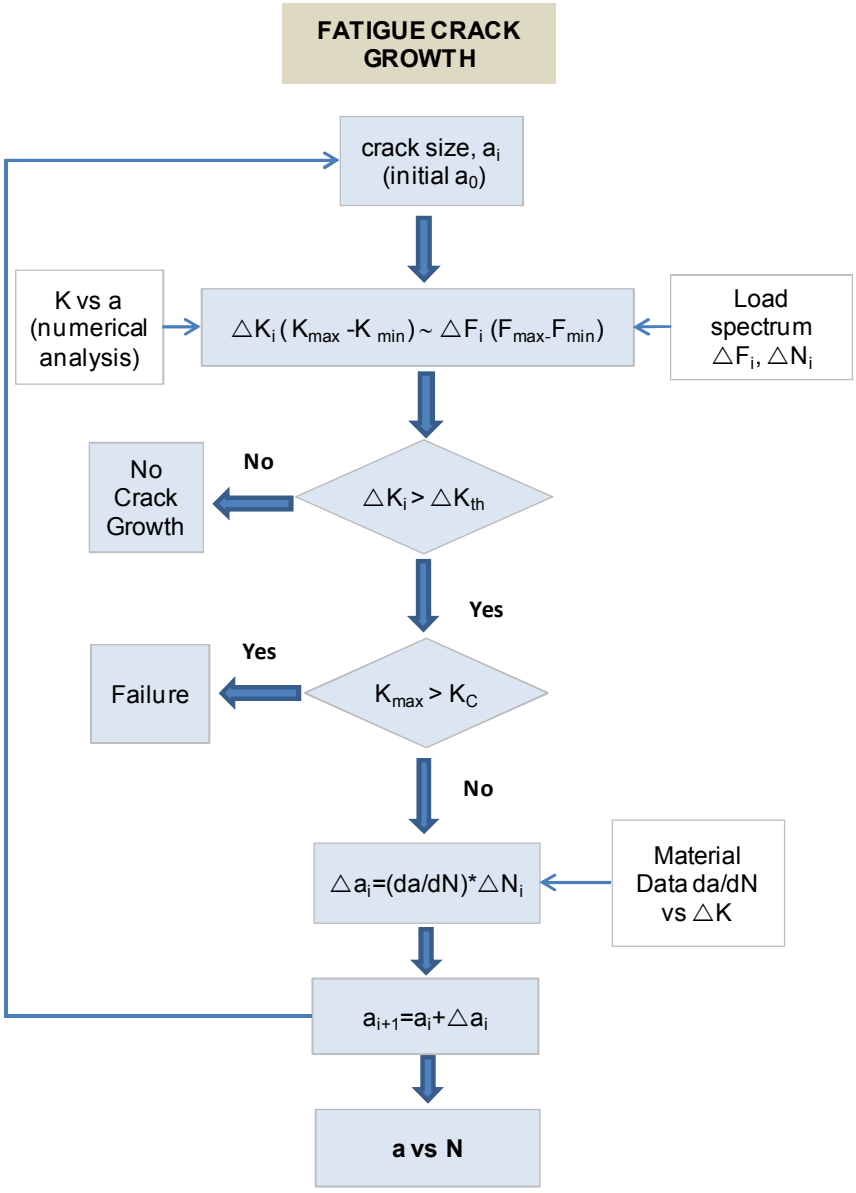

Figure 64 Fatigue Life Estimation Procedure

4.5.1. Fatigue Propagation Laws

Fatigue crack propagation laws such as Paris law, Walker, Foreman and Nasgro are widely used to analyze fatigue crack growth. These models are empirical curve fits used the prediction of the fatigue life.

Paris Law:

Paris and Erdogan presented that the growth of the crack under cyclic loading is governed by the equation representing a straight line on a log-log plot of da/dN vs $\triangle K$:

$$\frac{da}{dN} = C(\Delta K)^n \tag{28}$$

Where N is the number of load cycles, a is the crack length; n and C are the empirical constants depending on the material properties and stress ratio. The definition of stress intensity factor range, $\triangle K$ is expressed as:

$$\Delta K = K_{max} - K_{min} = (\sigma_{max} - \sigma_{min})\beta\sqrt{\pi a} \tag{29}$$

where K_{min} and K_{max} are the minimum and maximum stress intensity factors corresponding to the maximum applied stress, σ_{max} and the minimum applied stress, σ_{min}.

As shown in Figure 65, crack growth rate considerably varies in regime I close to threshold stress intensity factor, K_{th} and in regime III close to the fracture toughness K_{ic}. The Paris law governs only regime II portion of the total crack growth.

The fatigue crack growth is not available under the threshold value, ΔK_{th}. The values of K_{max} approaching the material's fracture toughness, K_{IC} lead to very rapid crack growth rates causing catastrophic failure.

Walker Equation:

The Walker equation includes the influence of the stress ratio ($\sigma_{min}/\sigma_{max}$) on the crack growth rate. However it does not consider the crack growth characteristics near threshold and fast fracture regions. For negative and positive stress ratios the equations are given as:
for $R \geq 0$

$$\frac{da}{dN} = C[\Delta K(1-R)^{(m-1)}]^n \tag{30}$$

for $R<0$

$$\frac{da}{dN} = C[K_{max}(1-R)^{(m-1)}]^n \tag{31}$$

where C is the empirical constant and n is the material constant obtained from data at various stress ratios, R.

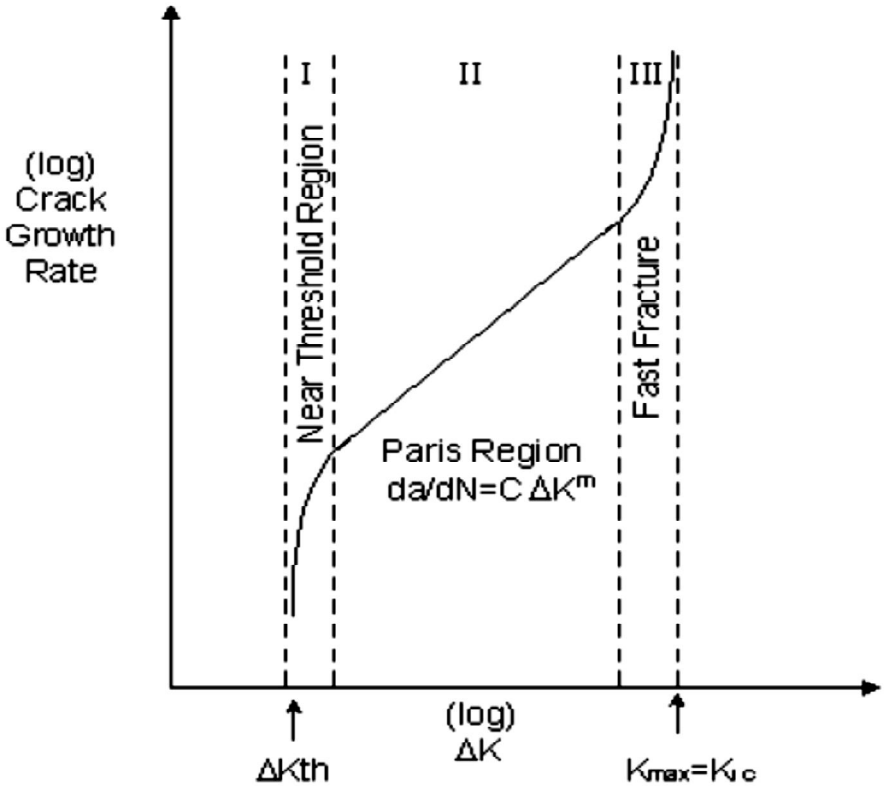

Figure 65 Fatigue crack growth rate vs ΔK

Foreman's Model:

Foreman's model [52] accounts for slow increase in crack growth rate at $K_{min} \approx K_{th}$ and increase in crack growth rate as K_{max} approaches to K_{IC}.

$$\frac{da}{dN} = \frac{C(\Delta K)^n}{(1-R)K_C - \Delta K} \tag{32}$$

where K_c is the critical fracture toughness of the material; C and n are the equation constants; R is the stress ratio ($\sigma_{min}/\sigma_{max}$).

Foreman equation does not take into account shifting the data in terms of stress ratio (R). The data shifting is adjusted by the plane stress fracture toughness (K_C) of the material.

NASGRO equation:

$$\frac{da}{dN} = C\left[\frac{(1-f)}{(1-R)}\Delta K\right]^n \frac{\left(1-\frac{\Delta K_{th}}{\Delta K}\right)^p}{\left(1-\frac{K_{max}}{K_{crit}}\right)^q} \tag{33}$$

where C, q, p and n are empirically derived constants. K_{crit} is the crack resistance against fracture.

f is given as below;

$$f = \frac{K_{op}}{K_{max}} = \begin{cases} max(R, A_0 + A_1R + A_2R^2 + A_3R^3) & R \geq 0 \\ A_0 + A_1R & -2 \leq R < 0 \\ A_0 - 2A_1 & R \leq -2 \end{cases}$$

The coefficients are;

$$A_0 = (0.825 - 0.34\eta + 0.05\eta^2)\left[cos\left(\frac{\pi}{2}S_{max}/\sigma_0\right)\right]^{\frac{1}{\eta}}$$

$$A_1 = (0.415 - 0.071\eta)S_{max}/\sigma_0$$

$$A_2 = 1 - A_0 - A_1 - A_3$$

$$A_3 = 2A_0 + A_1 - 1$$

4.5.2. Mixed Mode Fatigue Crack Growth Rate

Various criteria are proposed for the calculation of effective stress intensity factors used to compute fatigue crack growth rates under mixed-mode state. Some of the models are reviewed in this section.

Tanaka's Model:

The equation proposed by Tanaka [53] is given below:

$$\Delta K_{eff} = (\Delta K_I^4 + 8\Delta K_{II}^4)^{1/4} \tag{34}$$

The fatigue crack growth rate is proposed by using a similar type expression of Paris law:

$$\frac{da}{dN} = C(\Delta K_{eff})^m \tag{35}$$

Tanaka obtained the correlation between the best fit of his test data and the equation (34).

Effective Strain Energy Density Factor Model

It is used by Sih and Barthelemy [54] by implementing strain energy density factor to correlate fatigue crack growth rate:

$$\frac{da}{dN} = B(\Delta S)^m \tag{36}$$

where B and m are empirical constants.
The strain energy density factor range under mixed-mode state is defined as:

$$\Delta S = a_{11}\left(K_{Imax}^2 - K_{Imin}^2\right) + 2a_{12}(K_{Imax}K_{IImax} - K_{Imin}K_{IImin}) + a_{22}(K_{IImax}^2 - K_{IImin}^2) \tag{37}$$

where a_{ij} is the equation depending on the material elastic constants and the crack growth angle.

Tong & Yan' s Model:

This model is obtained from maximum tangential stress criterion.

$$\Delta K_{eff} = \frac{1}{2}cos\frac{\theta}{2}[\Delta K_I(1 + cos\theta) - 3\Delta K_{II}sin\theta] \tag{38}$$

The angle,θ in the equation is the crack propagation direction computed by the maximum tangential stress criterion.

Richard's Model

It is an empirical model as below:

$$\left(\frac{K_I}{K_{IC}}\right) + \left(a\frac{K_{II}}{K_{IC}}\right)^2 = 1 \tag{39}$$

$$K_{eff} = \frac{1}{2}K_I + \frac{1}{2}\sqrt{K_I^2 + 4(aK_{II})^2} \tag{40}$$

where $a = \frac{K_{IC}}{K_{IIC}}$

Energy Release Rate Model

The formulation is given as:

$$\Delta K_{eff} = \left(\Delta K_I^2 + \Delta K_{II}^2 + \frac{1}{1-v} \Delta K_{III}^2 \right)^{1/2} \quad (41)$$

For Mod-I and mod-II effective stress intensity factor is:

$$\Delta K_{eff} = (\Delta K_I^2 + \Delta K_{II}^2)^{1/2} \quad (42)$$

4.5.3. Computation of Fatigue Crack Growth Life

Fatigue crack growth analysis is extensively carried out for Mod-I cases without consideration of the change in propagation angle. However the crack propagation due to fatigue loading will not be in a straight direction in most of the cases because of mixed mode condition emerging from the initial crack angle and the direction of the loading. Even uniaxially loaded structures can contain crack with the orientation not perpendicular to the loading axis, which develops mixed-mode state.

The crack propagation analysis is performed for each load cycle given in Table 31. Mode-I and mode-II stress intensity factors are previously obtained in section 4.4. so it is provided the opportunity to assess the fatigue life for both cases of Mode-I and mixed mode. Eq. (38) is used to compute the effective stress intensity factor for mixed mode case.

Computation of fatigue crack growth is done for the following cases, which are specified in Table 38:

1- Basic configuration (configuration-1)

2- Configuration in which the direction of crack propagation not changing (configuration-2)

3- Configuration with the broken stringer (configuration-4)

Based on the investigation of the influence of the structural parameters on stress intensity factor, it is found that the most conservative case is the broken stiffener state because of high stress intensity factors along the crack path compared to the other cases The comparison of stress intensity factors between mode-I, K_I and mixed mode, K_{eff} is demonstrated in Figure 66. It shows that stress intensity factor values K_I and K_{eff} are almost same. The main difference occurs at few steps after the crack begins to grow. It is due to the fact that opening mode is very dominant so that stress intensity factor values for Mode-II are very small as compared to those for Mode-I, and as the crack propagates by changing its growth direction, mode-II stress intensity factor decreases.

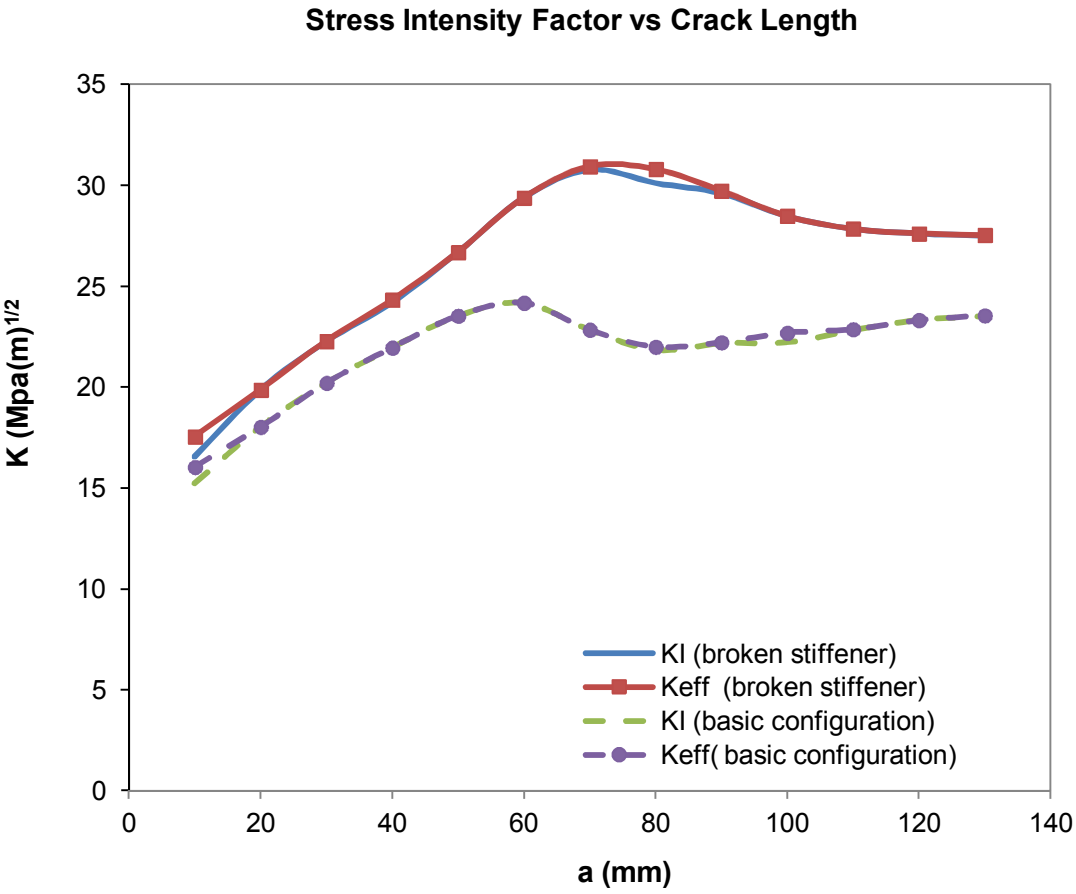

Figure 66 Mode-I and effective stress intensity factor plots

The Walker's equation is applied as a crack growth model. The empirical constants published by NASA are used [55]. The constant values are given in Table 50. The crack growth rate plots (da/dN vs K) are presented in Appendix A.

Table 50 Empirical Constants of 2024 T3 Aluminum (T.L.)

C ($mm(Mpa\sqrt{mm})^{-n}cycle^{-1}$)	n	m
$2.67x10^{-13}$	3.477	0.623

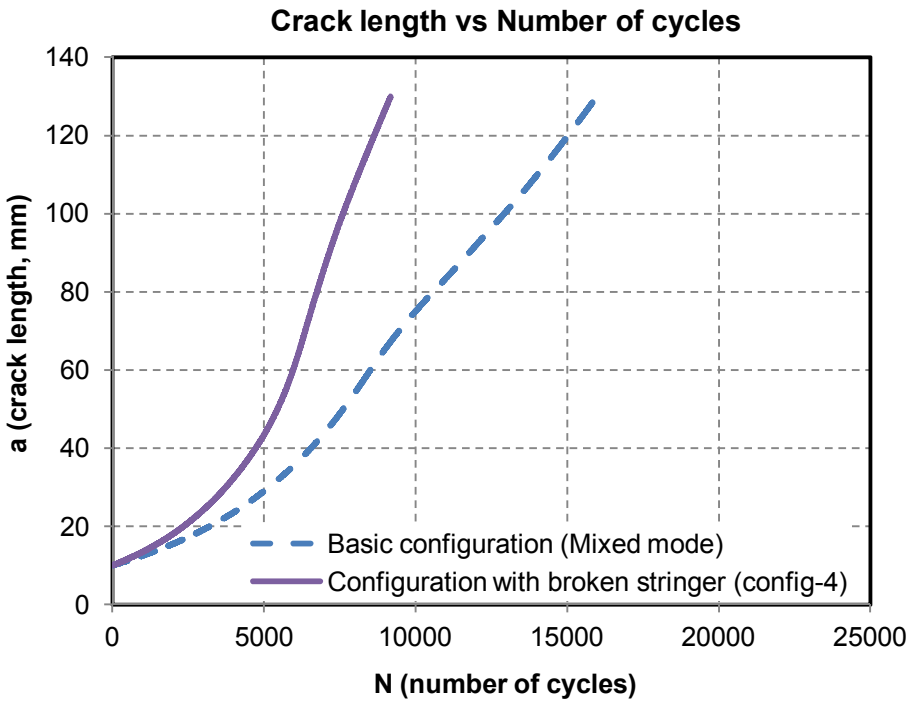

Figure 67 Crack length vs number of cycles for basic configuration and the broken stiffener case

The fatigue analyses are carried out up to the crack length of 130 mm. No fracture failure occurs up to that length of the crack. The effective stress intensity factors for mixed mode are almost same as those for mode-I due to low mode-II stress intensity factors. It is clearly observed from Figure 67 that crack growth rate for the broken stiffener case is much higher than basic configuration with the unbroken stiffener. The effective stress intensity factors are computed by Tong and Yan's method for both cases.

The configuration in which the direction of crack propagation is not changed (configuration-2) gives unconservative results when it is compared to the case in which the direction of the crack propagation is considered (see Figure 68). Mode-I stress intensity factor is used to calculate the crack length corresponding to the number of cycles for the configuration-2. Hence the fatigue crack growth for the structures under mixed mode loading should be analyzed by considering the change in the angle of crack extension.

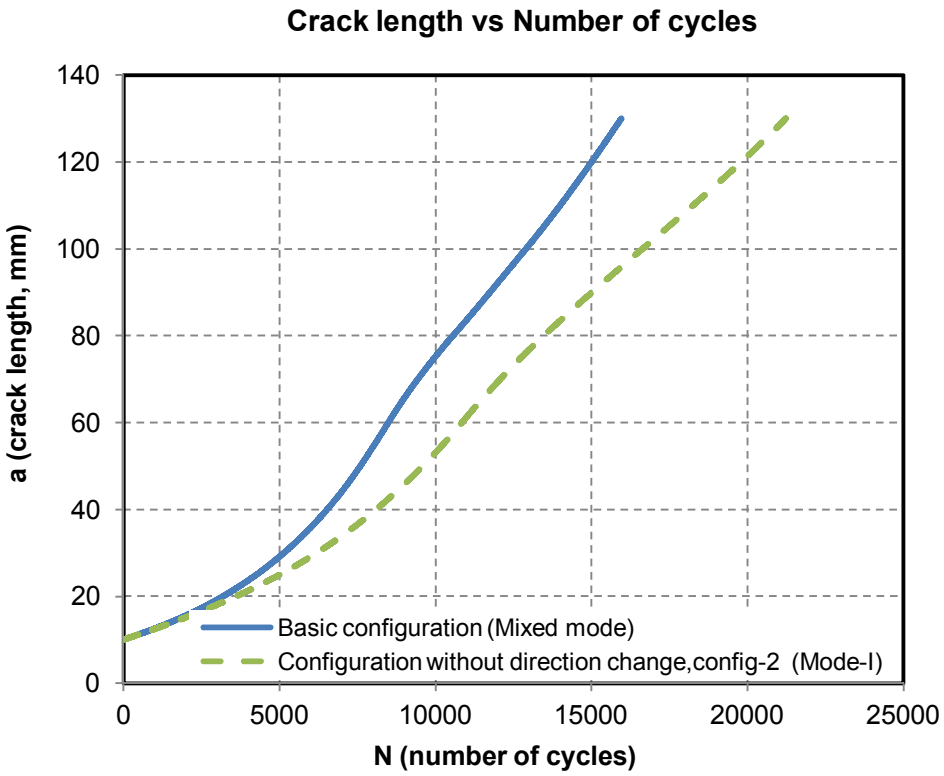

Figure 68 Crack length vs number of cycles for the configuration considering mixed-mode and the configuration with the angle of crack not changing

CHAPTER 5

CONCLUSION

The study is mainly focused on simulating automatic fatigue crack propagation under mixed mode loading with consideration of change in the angle of crack growth. The developed tool is utilized for a stiffened panel structure at helicopter tail boom section. Then the fatigue analysis of the structure is completed by using mode-I and mixed mode propagation laws. Finite element models are prepared by MSC.Patran as pre-processor, and MSC.Marc/Mentat is used as solver throughout the study.

Virtual crack closure technique is utilized to compute energy release rates, and then they are transformed into stress intensity factors. The efficiency of the technique is investigated by a comparative study with the cases from literature. One of the studies is on the stiffened panels with a crack approaching to the stiffener and passing through it. The computation of mode-I SIF is carried out for both the intact and riveted type stiffened panels. The comparison between the numerical and experimental results indicates that VCCT adequately estimates K_I values for the stiffened panels. The difference with the results from literature does not exceed % 3 for the all cases.

The other study includes a plate with an inclined crack subjected to the tensile loading, where a mixed-mode case occurs. The angle of the crack plane with loading direction is altered to generate various mixed mode cases, which causes different values of mode-I and mode-II. The numerical results show that the mesh size at the crack tip affects the accuracy of the computation, and after enough mesh refinement, Quad4 element type can be used in finite element model instead of Quad8. VCCT has also a capability to compute SIFs with a good accuracy under mixed-mode conditions. It is concluded that virtual crack closure technique is a powerful and easily adapted method to compute the stress intensity factor, which gives reliable results.

A tool is developed to simulate automatic crack growth, which consists of two key parts: mesh generation and numerical analysis. Fortran programing language is used to create the tool executing automatically the subsequent steps; mesh generation, numerical analysis and writing the results on the output file. In order to update the finite element model in accordance with new crack condition, the code activates another code created by using PCL (Patran Command Language). Input solver parameters and running the analysis are carried out by means of procedure file of MSC.Marc/Mentat, which is called by the Fortran code. Maximum tangential stress criterion (MTSC) is employed to predict the angle of the crack extension in the study. The output of the tool is variation of stress intensity factors with the crack length, which is used to evaluate damage tolerance behavior of the structure and to estimate the propagation fatigue life. Simulation of the case studies, which are experimentally investigated in the literature is performed by means of the developed code to verify the numerical method, which combines VCCT and MTSC. Case studies focus on several parameters that affect the computational accuracy of SIFs and the prediction of the crack trajectories: the element size in the vicinity of the crack tip and length of the crack extension. As a result of simulations, the predicted crack trajectories agree well with the experimental results, and the computed SIFs exhibit the expected trends. Another observation is that the crack increment size affects the crack path. Increase in extension

length yields more deviation from the crack path obtained in experimental study. As a consequence, the implementation of the tool for mixed mode fracture problems shorten the simulation time and allows more detailed investigation of the design variations affecting the damage tolerance of the structure to be analyzed.

Last part of the study includes the implementation of the developed tool to compute SIFs for fuselage structure of a helicopter tail boom section. A local model, which includes more detailed features of the structure, is used to overcome the difficulties that appear in the process of finite element modeling of large and complex geometries. Different sub-modeling techniques are compared, and the submodeling, which is more efficient in terms of time required for the analysis is decided. Crack growth behavior of complex geometries like stiffened panel is simulated easily by employing the developed tool. With this capability, the effect of various structural parameters; the broken stringer, nonexistence of the stiffener, rivet spacing, rivet material, the stringer size and the panel thickness on SIF is investigated for the stiffened helicopter panel by comparing variations of stress intensity factor values through the crack path. The results show clearly that the stiffeners have good crack-arrest capability, and how much geometrical features can enhance the damage tolerance performance of the stiffened panels for the structure investigated in this thesis. It is seen that the most critical scenario is the case of the skin crack in the presence of the broken stiffener.

The fatigue crack growth analyses are performed for the different configurations of the stiffened helicopter fuselage by using stress intensity factors obtained by numerical analyses. The plots of the crack length vs number of cycles show that consideration of the change in the crack propagation angle under mixed mode is very important to predict accurate fatigue life.

The thesis can be extended by the following subjects;

- The method presented here, which combines VCCT and the maximum hoop stress criterion can be compared with the other methods used for the prediction of the crack extension angle and stress intensity factor. The other techniques to compute SIFs (J-Integral, displacement correlation technique) and to predict crack extension angle (minimum energy density, maximum energy release rate) can be adapted to the program as an option. Hence the comparison with the other techniques can be performed.
- In this study the crack propagating from a cut-out is investigated. The crack initiated from a rivet hole could be included in the further study. The method could be extended for the cracks propagating at both crack tips.
- The simulation of a stiffened helicopter panel could be carried out by the other finite element softwares such as Abaqus and Franc 3D instead of MSC.Marc/Mentat. The crack trajectories and stress intensity factors could be compared.
- The fracture analysis is performed for 2D models in the study. The developed program could be extended for the usage of VCCT in 3D cases. Hence the method presented here could be adopted for 3D models. However it could need much more effort due to complexity of crack propagation in 3D.
- The fracture analysis of the other helicopter structures subjected to multiaxial loading can be analyzed by utilizing the code developed in this thesis.

REFERENCES

[1] Wanhill R.J. Milestone Case Histories in Aircraft StructuralIntegrity. National Aerospace Laboratory NLR-TP-521 2002.

[2] Tavers S.M.O, Moreira P.M.G.P, Pastrama S.D, Castro P.M.S.T. Stress Intensity Factors by Numerical Evaluation in Cracked Structures. 11th Portuguese Conference on Fracture (Lisbon, Caparica) 2008

[3] Bucholz F.G, Chergui A, Richard H.A. Computational Fracture Analysis By Means of Virtual Crack Closure Technique. Argentine Congress of Computational Mechanics 1999;307-325.

[4] Orifici A.C, Krueger R. Assessment of Static Delamination Propagation Capabilities in Commercial Finite Element Codes Using Benchmark Analysis. NASA CR-2010-216709

[5] Poe C.C. Stress-Intensity Factor for a Cracked Sheet With Riveted and Uniformly Spaced Stringers. NASA Technical Report TR R-358 2008

[6] Isida M. Analysis of Stress Intensity Factors for The Tensiion of A Centrally Cracked Strip with Stiffened Edges. Engineering Fracture Mechanics 1973; 5:647-665

[7] Carta F, Pirondi A. Damage Tolerance Analysis of Aircraft Reinforced Panels. Frattura ed Integrita Strutturale 2011;16:34-42.

[8] Adeel M. Study on Damage Tolerance Behavior of Integrally Stiffened Panel and Conventional Stiffened Panel. World Academy of Science, Engineering and Technology 2008;45:315-319.

[9] Tavers S.M.O, Trummer V.R, Moreira P.M.G.P, Castro P.M.S.T. Fatigue Behaviour of Lightweight Integral Panels. 7th Eromech Solid Mechanics Conference, (Lisbon, Portugal) 2009.

[10] Brot A, Wolfin Y.P, Kressel I, Yosef Z. The Damage Tolerance Behavior of Integrally Stiffened Metallic Structures. Israel Annual Conference on Aerospace Sciences 2008.

[11] Arsene S, Van der Veen S, Muzzolini R. A Finite Element Approach to Optimizing Damage Tolerance of Airframe Panels. MSC VPD Conference 2004.

[12] Bouchard P.O, Bay F, Chastel Y. Numerical Modeling of Crack Propagation: Automatic Remeshing and Comparison of Different Criteria. Compuational Methods Applied Mechanical Engineering. 2006;192:3887-3908.

[13] Ayhan A.O. Simulation of Three-Dimensional Fatigue Crack Propagation Using Enriched Finite Elements. Computers and Structures 2011;89:801-812.

[14] Colombo D, Giglio M. A Methodology For Automatic Crack PropagationModeling in Planar And Shell FE Models. Engineering Fracture Mechanics 2006;73:490-504.

[15] Miranda A.C.O, Meggiolaro M.A, Castro J.T.P, Martha L.F, Bittencourt T.N. Fatigue Life and Crack Predictions In Generic 2D Structural Components. Engineering Fracture Mechanics 2003;70:1259-1279

[16] Boljanovic S, Maksimovic S, Analysis of The Crack Propagation Process Under Mixed-mode Loading. Engineering Fracture Mechanics 2011;78:1565-1576

[17] Qian J, Fatemi A. Fatigue Crack Growth Under Mixed-Mode I and II Loading. Fatigue and Fracture of Engineering Materials and Structures 1996;19:1277-1284.

[18] Chen C.S, Wawrzynek P.A, Ingraffea A.R, A Methodology of Fatigue Crack Growth and Residual Strength Prediction with Applications to Aircraft Fuselages. Computational Mechanics1997;19:527-532

[19] Rooke D.P, Cartwright D.J. Compendium of Stress Intensity Factors. The Hillington Press England 1976.

[20] Murakami Y, Stress Intensity Factors Handbook Vol.1 and Vol.2. Pergamon Press England 1987.

[21] Shih C.F, Lorenzi H.G, German M.D, Crack Extension Modeling with Singular Quadratic Isoparametric Elements. International Journal of Fracture 1984;51:69-107.

[22] Theilig H., Bucholz F.G., Crack Path Prediction By The MVCCI-Method and Experimental Verification For Specimens Under proportional Bending And Shear Loading. Argentine Congress of Computational Mechanics 1999;119-130.

[23] Ingraffea A.R, Wawrzynek P.A, Finite Element Methods for Linear Elastic Fracture Mechanics. Comprehensive Structural Integrity Vol3: Numerical and Computational Methods;1-88

[24] Rice J.R. Mathematical Analysis in The Mechanics of Fracture. Fracture: An Advanced Treatise, Academic Press New York 1968

[25] Rybicki EF, Kanninen M.F. A Finite Element Calculation of Stress Intensity Factors by a Modified Cracl Closure Integral. enfgineering Frcture Mechanics 1987;9:931-938

[26] Ramamurthy T.S. Krishnamurthy T, Badarinarayana K, Vijayakumar K, Dattaguru B. Modified Crack Closure Integral Method With Quarter Point Elements. Mechanics Research Communications 1986;13:179-186.

[27] Raju I.S. Calculation of Strain-Energy Release Rates With Higher Order And Singular Finite Elements. Engineering Fracture Mechanics 1987;28:251-274.

[28] Shivakumar K.N, Tan P.W, Newman J.R, A Virtual Crack Closure Technique for Calculating Stress Intensity Factors for Cracked Three Dimensional Bodies. International Journal of Fatigue 1988;36:43-50.

[29] Irwin G.R. Analysis of Stresses and Strains Near The End of A Crack Traversing Plate. Journal Of Applied Mechanics 1957;24:361-364

[30] Bucholz F.G, Chergui A, Richard H.A. Fracture Analysis and Experimental Results of Crack Growth Under Mixed Mode Loading Conditions. Engineering Fracture Mechanics 2004;71:455-468

[31] Erdogan F, Sih G.C. On the Crack Extension in Plane Loading and Transverse Shear. Journal of Basic Engineering 1963;85:519-527.

[32] Hussain M.A, Pu S.U, Underwood J. Strain Energy Release Rate For A Crack Under Combined Mode I and Mode II. ASTM STP 560 1974;2-28

[33] Sih G.C. Strain Energy Density Factor Applied to Mixed-mode Crack Problems. International Journal of Fracture Mechanics 1974;10:305-321.

[34] Wawrzynek P.A, Carter B.J, and Ingraffea A.R. Advances in Simulation of Arbitrary 3D Crack Growth using FRANC3D/NG Proc. 12th International Conference on Fracture (Ottawa, Canada) 2009.

[35] Almroth B, Brogan F, and Stanley G. User's Manual for Stags. NASA CR-165670 1978.

[36] Seshadri B.R, Newman J.C., Dawicke D.S., Young R.D. Fracture Analysis of the FAA/NASA Wide Stiffened Panels. NASA Technical Momerandum 1998-208976. 1998.

[37] MSC.Marc Theoy and User Information, Volume:A, 2010

[38] Abaqus Analysis User's Manual, Providence, RI,USA, 2009.

[39] ANSYS Release Notes, 2010

[40] Leski A. Implementation of Virtual Crack Closure Technique in Engineering FE Calculations. Finite Elements in Analysis and Design 2007;43:261-268

[41] Krueger R, Goetze D. Influence of finite Element Software on Energy Release Rates Computed Using The Virtual Crack Closure Technique. NASA CR-214523 2006.

[42] Alshoaibi A.M, Hadi M.S, Ariffin A.K. Finite Element Simulation of Fatigue Life Estimation and Crack Path Prediction of Two-dimensional Structures Components. The Hong Kong Institution of Engineers Transactions 2008;15:1-6

[43] Carvalho C.V, Araujo T.D.P, Cavalcente J.B, Martha L.F, Bittencourt T.N. Automatic Fatigue Crack Propagation using a Self-adaptive Strategy. Pan-American Congress of Applied Mechanics 1999;6:377-380.

[44] Federal Aviation Regulations, Advisoty Circular: Certification of Normal Category Rotorcraft 27-1B, FAA.

[45] Giglio M, Manes A. Effect of Flight Spectrum Loads On The Damage Tolerance Evaluation of A Helicopter Frame. Materials with Complex Behaviour, Advanced Structured Materials 2010;3:311-329.

[46] Giglio M. FEM Submodeling Fatigue Analysis of A Complex Helicopter Component. International Journal of Fatigue 1999;21:445-455

[47] Potyondy D.O, Wawrzynek P.A, Ingraffea A.R. Discrete Crack Growth Analysis Methodology for Through Cracks in Pressurized Fuselage Structures. International Journal for Numerical Methods in Engineering 1995;38:1611-1633.

[48] MSC.Nastran Quick Reference Guide 2010

[49] Huth H. Influence of Fastener Flexibility On The Prediction Of Load Transfer And Fatigue Life For Multiple-Row Joints. Fatigue In Mechanically Fastened Composite And Metallic Joints ASTM Special Technical Publication 927 1986;221-250.

[50] Swift T. Fracture Analysis of Stiffened Structures. Damage Tolerance of Metallic Structures: Analysis Methods and Applications, ASTM Special Technical Publication 1984;842:69-107.

[51] Bent L.J, Practical Airframe Fatigue and Damage Tolerance. Sigma K. Ltd. 2010

[52] Forman R. G, Kearney V. E, Engle R. Numerical Analysis of Crack Propagation in Cyclic-Loaded Structures.Journal of Basic Engineering 1967;89:459-464

[53] Tanaka K, Fatigue Crack Propagation From a Crack Inclined to The cyclic Tensile Axis. Engineering Fracture Mechanics 1974;6:493-507

[54] Sih G.C, Barthelemy B.M. Mixed Mode Fatigue Crack Growth Predictions. Engineering Fracture Mechanics 1980;13:657-666

[55] Forman R.G, Shivakumar V, Cardinal J.W, Williams L.C, McKeighan P.C. Fatigue Crack Growth Database for Damage Tolerance Analysis. Federal Aviation Administration 2005.

[56] MMPDS-04 (Metallic Materials Properties Development and Standardization. Federal Aviation Administration. 2008

APPENDIX A

MECHANICAL PROPERTIES OF THE MATERIALS USED IN THE THESIS

Table 3.2.4.0(b_1). Design Mechanical and Physical Properties of 2024 Aluminum Alloy Sheet and Plate

Specification	AMS 4037 and AMS-QQ-A-250/4[a]					AMS-QQ-A-250/4[a]		
Form	Sheet					Sheet		Plate
Temper	T3					T361		
Thickness, in.	0.008-0.009	0.010-0.128		0.129 - 0.249		0.020-0.062	0.063-0.249	0.250-0.500
Basis	S	A	B	A	B	S	S	S
Mechanical Properties:								
F_{tu}, ksi:								
L	64	64	65	64	66	68	69	67
LT	63	63	64	63	65	67	68	66
ST	...	...	...	...	...	...	...	...
F_{ty}, ksi:								
L	47	47	48	47	48	56	56	54
LT	42	42	43	42	43	50	51	49
ST	...	...	...	...	...	...	...	...
F_{cy}, ksi:								
L	39	39	40	39	40	47	48	46
LT	45	45	46	45	46	53	54	52
ST	...	...	...	...	...	...	...	...
F_{su}[b], ksi	39	39	40	40	41	42	42	41
F_{bru}[b,c], ksi:								
(e/D = 1.5)	104	104	106	106	107	111	112	109
(e/D = 2.0)	129	129	131	131	133	137	139	135
F_{bry}[b,c], ksi:								
(e/D = 1.5)	73	73	75	73	75	82	84	81
(e/D = 2.0)	88	88	90	88	90	97	99	96
e, percent:								
LT	10	[d]	...	[d]	...	8	9	9[e]
E, 10^3 ksi	10.5							10.7
E_c, 10^3 ksi	10.7							10.9
G, 10^3 ksi	4.0							4.0
μ	0.33							0.33
Physical Properties:								
ω, lb/in.^{3}	0.100							
C, K, and α	See Figure 3.2.4.0							

Figure 69 Mechanical Properties of 2024 Aluminum Alloy [56]

Table 3.7.4.0(b_1). Design Mechanical and Physical Properties of 7050 Aluminum Alloy Plate (Continued)

Specification	AMS 4050															
Form	Plate															
Temper	T7451															
Thickness, in.	0.250-1.500		1.501-2.000		2.001-3.000		3.001-4.000		4.001-5.000		5.001-6.000		6.001 -7.000		7.001 - 8.000	
Basis	A	B	A	B	A	B	A	B	A	B	A	B	A	B	A	B
e, percent (S-Basis):																
L	10	...	10	...	9	...	9	...	9	...	8	...	7	...	6	...
LT	9	...	9	...	8	...	6	...	5	...	4	...	4	...	4	...
ST	...	...	...	...	3	...	3	...	3	...	3	...	3	...	3	...
E, 10^3 ksi	10.3															
E_c, 10^3 ksi	10.6															
G, 10^3 ksi	3.9															
μ	0.33															
Physical Properties:																
ω, lb/in^3	0.102															
C, Btu/(lb)(°F)	0.23 (at 212°F)															
K, Btu/[(hr)(ft^2)(°F)/ft]	91 (at 77°F)															
α, 10^{-6} in./in./°F	12.8 (68° to 212°F)															

Issued: Sep 1976, MIL-HDBK-5C, Item 71-08. Last Revised Jan 2005, MMPDS-02, Item 04-30. Design allowables were reaffirmed in Item 07-32, MMPDS-04.

a A-Basis value is specification minimum. Rounded T_{99} values for F_{tu} are as follows: for 0.250-1.500 (L) = 75 ksi, for 1.502-2.000 (LT) = 75 ksi, for 2.001-3.000 (L) and (LT) = 74 ksi,for 3.001-4.000 (ST) = 69 ksi, for 4.001-5.000 (L) and (LT) = 72 ksi, for 5.001-6.000 (L) = 71ksi.

b A-Basis value is specification minimum. Rounded T_{99} values for F_{ty} are as follows: for 0.250-1.500 (L) = 65 ksi, for 1.502-2.000 (L) = 65 ksi, for 2.001-3.000 (L) = 65 ksi, (LT) = 64 ksi, for 3.001-4.000 (L) = 63 ksi, for 4.001-5.000 (L) = 62 ksi, (ST) = 58 ksi, for 7.001-8.000 (L) = 59 ksi, (ST) = 56 ksi.

c See Table 3.1.2.1.1. Bearing values are "dry pin" values per Section 1.4.7.1.

Figure 70 Mechanical properties of 7050 aluminum alloy [56]

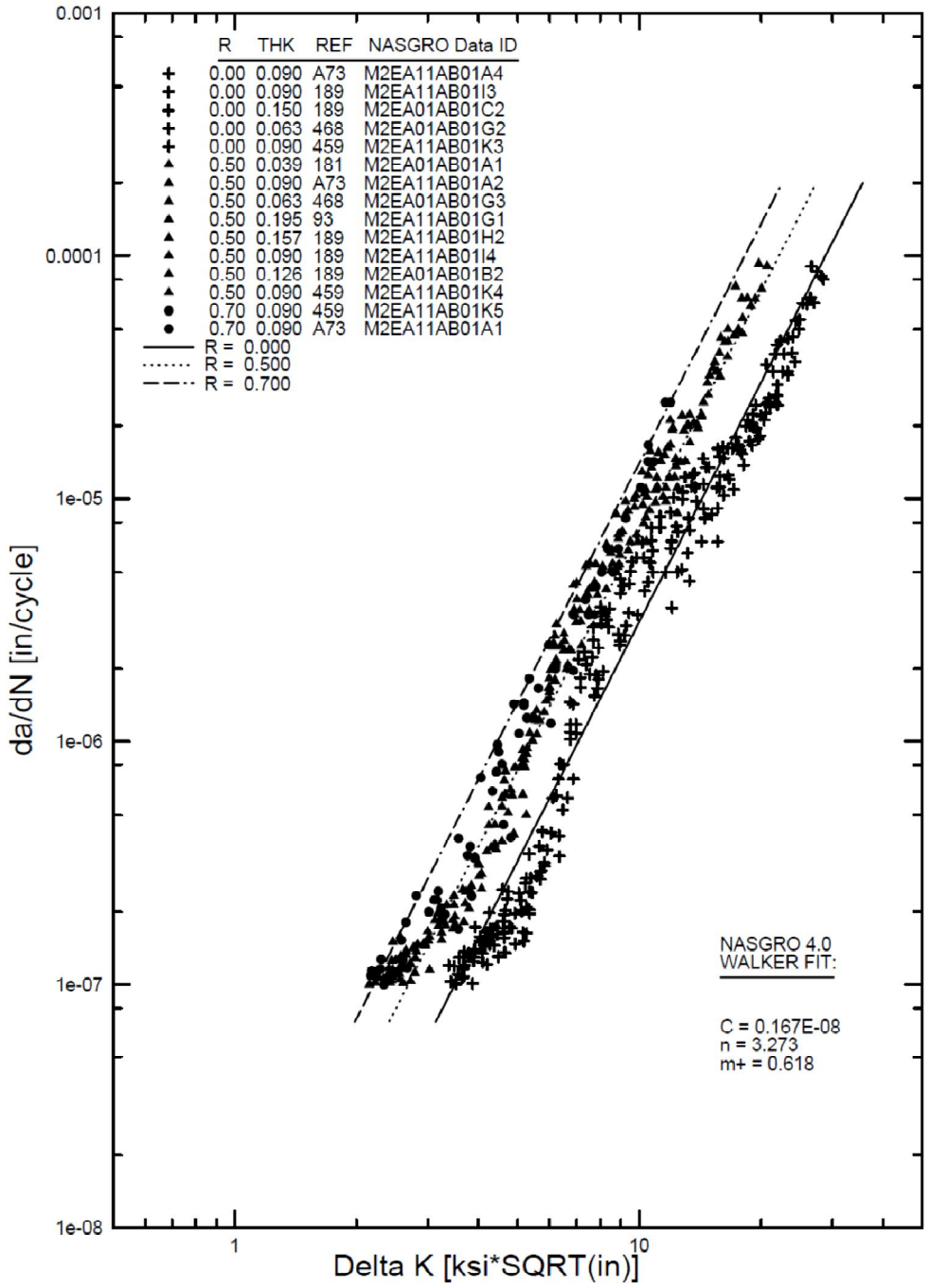

Figure 71 Walker equation fit for 2024-T3 sheet, L-T with positive R values [55]

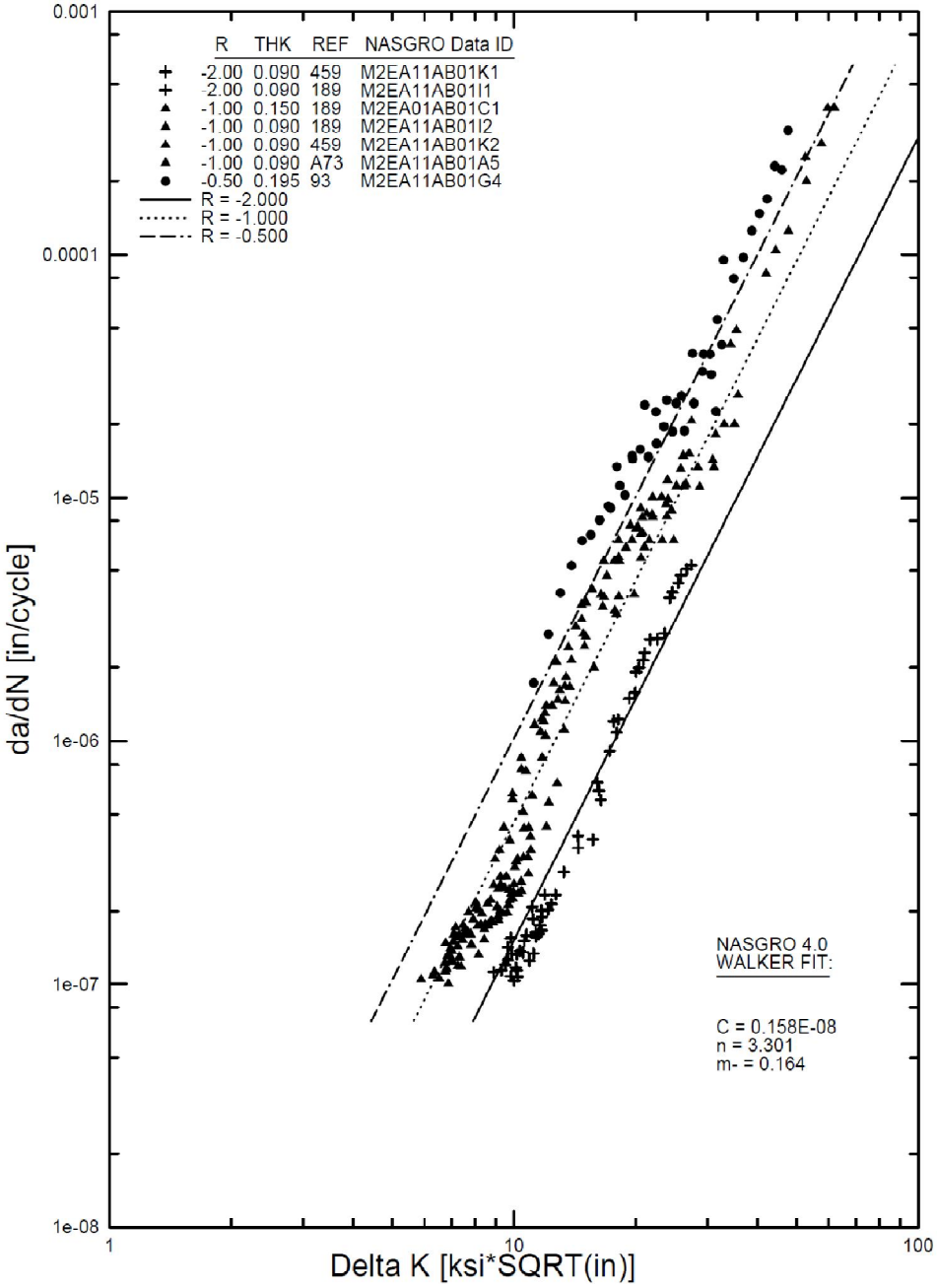

Figure 72 Walker equation fit for 2024-T3 sheet, L-T with negative R values [55]

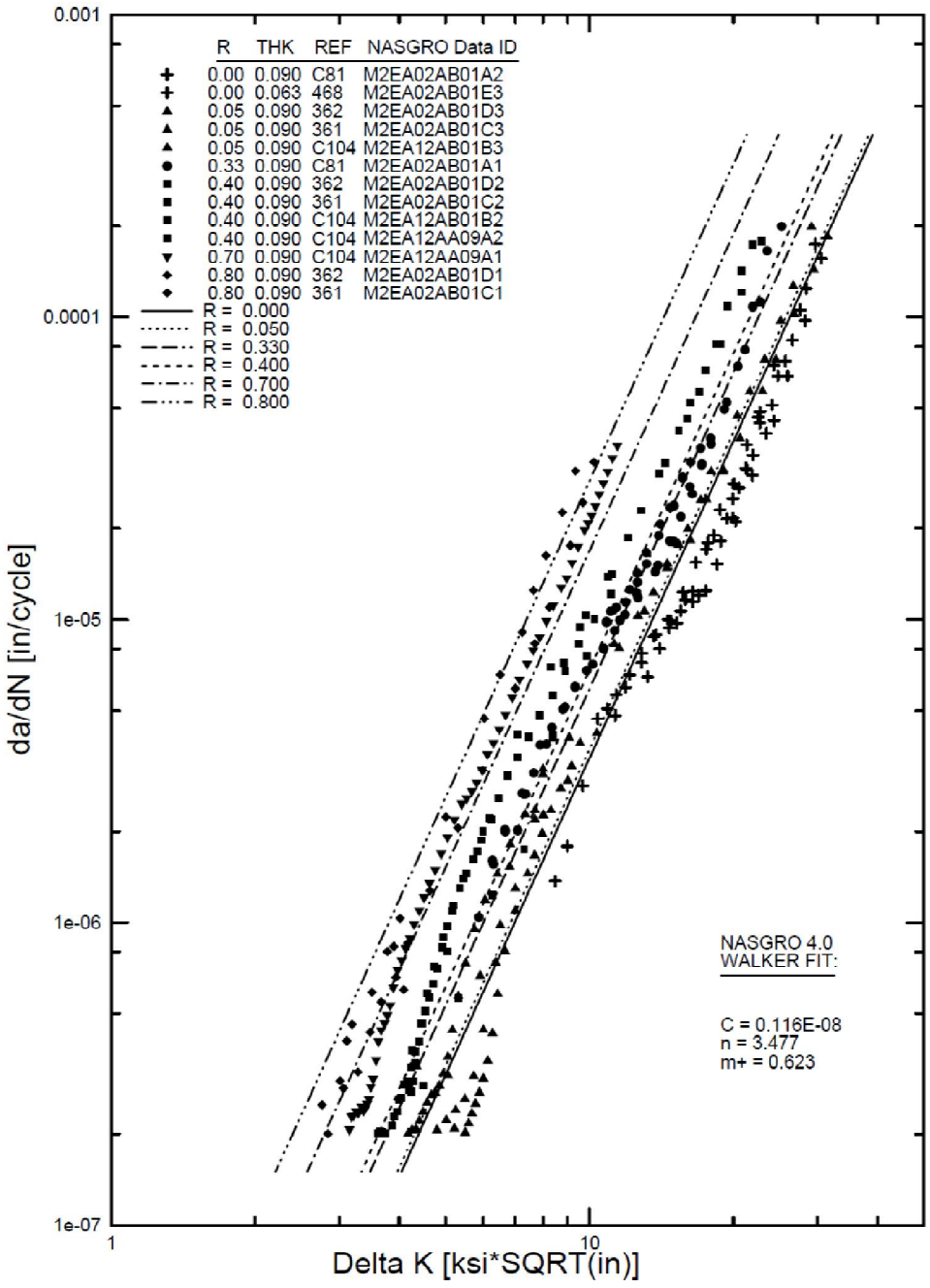

Figure 73 Walker equation fit for 2024-T3 clad and bare sheet T-L [55]